University of Virginia – Chemistry Department

PhD Thesis

Author:
Aspen R. Clements

Kinetic Monte Carlo simulations of ice processing: from the lab to interstellar environments

---

Supervisor:
Prof. Robin T. Garrod

July 13th, 2020

Committee Members:

Chair: Prof. Eric Herbst
Prof. Kateri Dubay, Dr. Anthony Remijan, and Dr. Catherine Dukes

Kinetic Monte Carlo simulations of ice processing: from the lab to interstellar environments

Dissertation

Aspen R. Clements
Kearney, Nebraska, United States

To Laika and all other animals that have furthered science. We shall be forever grateful. We would not be where we are today without your sacrifice...

"I, a universe of atoms, an atom in the universe."

Richard Feynman

Acknowledgements

Foremost, I would like to express my sincere gratitude to my advisor Professor Robin Garrod for his continuous support of my studies and research. I want to thank him for his patience, motivation, enthusiasm, and immense knowledge. His guidance helped me in all things over the last five years.

In conjunction with my advisor, I would like to thank the rest of my committee: Prof. Eric Herbst, Prof. Kateri DuBay, Dr. Anthony Remijan, and Dr. Catherine Dukes, for their encouragement, insightful comments, and compelling questions.

My sincere thanks also goes to Dr. Elisabeth Mills, for offering me a summer internship opportunity under her tutelage and providing a safe environment to discover the grand world of astronomy.

I would like to also thank my fellow labmates past and present in the Garrod Group, for the stimulating discussions and the fun we have had in the last five years. And special thanks to the labmates I have lived with, we always found a way to keep things interesting.

I want to thank all of the women who have inspired me and paved the way. Without your work a difficult task would have seemed insurmountable. You have inspired me, motivated me, and kept me going.

Last but not the least, I would like to thank my family, related and not, for helping me grow and supporting me. In particular, I want to thank my partner, Blake Clements Miller, for their constant encouragement, love, and understanding through this process. I would not be the woman I am today without your patience and kindness.

Abstract

Kinetic Monte Carlo simulations of ice processing: from the lab to interstellar environments

Dust grains in cold, dense interstellar clouds build up ice mantles through the accretion and subsequent surface chemistry of atoms and molecules from the gas. These mantles, of thicknesses on the order of 100 monolayers, are primarily composed of H_2O, CO, and CO_2. The formation of molecules on grain surfaces, and the subsequent production of complex organic molecules, has been demonstrated in laboratory experiments. However, interstellar physical conditions can never be exactly reproduced, and the timescales are vastly different (minutes in the lab versus many thousands of years in the ISM), making the correspondence of the two regimes highly uncertain. Laboratory experiments using interstellar ice analogs have shown that porosity could be present and can facilitate diffusion of molecules along the inner pore surfaces. Yet, there is considerable uncertainty about the structure of interstellar ices, their ability to store volatiles, and under what conditions. Further, the movement of molecules within and upon the ice is poorly described by current chemical kinetics models, making it difficult either to reproduce the formation of experimental porous ice structures or to extrapolate generalized laboratory results to interstellar conditions.

Here we use the off-lattice Monte Carlo kinetics model MIMICK to investigate the effects that various deposition parameters have on laboratory ice structures. We reproduce experimental trends in the density of amorphous solid water (ASW) for varied deposition angle, rate and surface temperature; ice density decreases when the incident angle or deposition rate is increased, while increasing temperature results in a more-compact water ice. The models indicate that the density behavior at higher temperatures ($\sim$80 K) is dependent on molecular rearrangement resulting from thermal diffusion. To reproduce trends at lower temperatures, it is necessary to take account of non-thermal diffusion by newly-adsorbed molecules, which bring kinetic energy both from the gas phase and from their acceleration into a surface binding site. Extrapolation of the model to conditions appropriate to protoplanetary disks, in which direct accretion of water from the gas phase may be the dominant ice formation mechanism, indicate that these ices may be less porous than laboratory ices.

To further elucidate the porosity of ices, we used infrared absorption spectra of CO on the pore surface of porous amorphous solid water (ASW), and quantified the effective pore surface area of ASW. Additionally, we present results obtained from a Monte Carlo model of ASW in which the morphology of the ice is directly visualized and quantified. We found that 200 ML of ASW annealed to 20 K has a total pore surface area that is equivalent to 46 ML. This surface area decreases linearly with increasing temperatures. We also found that dangling OH bonds only exist on the surface of pores; almost all of the pores in the ASW are connected to the vacuum-ice interface, and are accessible for

adsorption of volatiles from the gas phase; there are few closed cavities inside ASW at least up to a thickness of 200 ML; the total pore surface area is proportional to the total three-coordinated water molecules in the ASW.

The presence of such pores could facilitate diffusion of molecules on the inner pore surfaces. However, the movement of molecules within the primary component of ices, H_2O, is not fully understood, making it difficult either to reproduce the formation of experimental porous ice structures or to extrapolate generalized laboratory results to interstellar conditions. Previous work has established kinetic barriers for CO diffusion on and into H_2O ice, but the microscopic details are still unknown, and the mixing barrier is not well determined. Here we provide insight into the diffusion of CO on amorphous water ices with various morphologies. A microscopically-detailed kinetic Monte Carlo model is used to deposit layered H_2O-CO ices utilizing background and uniform-angle deposition, which produces H_2O ices of various densities. A series of isothermal diffusion experiments are run to calculate mixing at each time step and combined to calculate barriers of diffusion. The density and, more importantly, the pore structure play a role in the ability for CO to mix, thus influencing its diffusion barriers. For example, the most porous ice, deposited using background deposition, produces the largest barrier. Utilizing uniform angle deposition, barriers are slightly reduced. Uniform angle deposition produces denser ices with column-like structures. The empty space between the columns appears to be narrower at lower angles of incidence, preventing volatiles from mixing. This result suggests that uniform-angled deposition yields ices that are unreliable as interstellar ice analogs.

We show that using an off-lattice Monte Carlo kinetics model can illustrate how CO first diffuses through and then desorbs from H_2O ices. The strength of this model lies in the ability to monitor molecules desorbing from a surface, which produces spectra consistent with temperature-programmed desorption experiments. From the desorption profile, information about the binding energies and insight into the interacting structures can be extracted, providing direct comparisons to laboratory experiments. With this kinetics model, various stages of an experiment can be visualized, and precise structures can be explored. In addition, the model successfully predicts the characteristics of temperature-dependent structural changes phenomena that are observed experimentally. We find that the composition of the deposited ice is reflected in the desorption temperatures and profiles: layered ices have a two-peak structure at lower temperatures whereas mixed ices have a singular desorption peak. We also find efficient trapping in mixed ices where an ice 50 ML mixed was able to retain 68% of its original CO material. Layered porous ices also demonstrate trapping but with less efficiency. Ice trapping can play a significant role in protoplanetary disks where frozen volatiles provide material for the production of more complex species or be released at later times, changing the gas-phase chemistry.

Contents

List of Figures

List of Tables

Part I:

Overview

1

Introduction

Contents

Despite the fact that humans have been looking at the stars for centuries (e.g. as a means for navigation), it was thought that space was primarily empty. Since the development of radio and infrared astronomy, scientists have shown the interstellar medium (ISM), or the space between stars within a galaxy, is far from empty. On the contrary, the ISM contains a complex chemical array with changing physical properties. What would humans do but to study this complexity? Thus, astrochemistry was born. Astrochemistry is the study of the interplay between astronomy and chemistry and involves the study of the interaction, formation, and destruction of chemical components in the universe. Figure 1.4 represents the three fundamental aspects of astrochemistry: astronomical observations (panel a) where physical features of objects can be directly observed, astrophysical laboratory experiments (panel b) which help us identify new species and understand their response to controlled processing, and the main focus of this work, modeling (panel c). Modeling provides a means to test a series of reactions/processing and can give us microscopic detail that is otherwise unattainable. Further, modeling provides predictions of physical and chemical phenomenon that cannot be measured.

To understand the formation of stars, comets, planets, and even galaxies, scientists have to understand the chemistry that births those objects. Because of the interplay

between the chemistry and physical environments, we can tease out some of the physical processing that occurs in those environments. For example, in high radiation fields one can imagine very little chemical complexity because molecules are destroyed as soon as they are produced. This is one example of how chemical signatures can help identify macroscopic conditions, such as temperature and density. Further, once physical conditions can be understood, different stages of evolution of stars and galaxy can be made clearer. Unfortunately, because of this evolution, the chemistry in our terrestrial environment diverges from some of the most interesting objects in the ISM. For instance, densities can vary from $\sim 10^{-3}$ cm^{-3} in hot, diffuse regions of the ISM to 10^5 cm^{-3} in regions of star formation, whereas densities at sea level on Earth are around 10^{19} cm^{-3}. Unique chemical structures, often unlike those seen on Earth, have been observed because of these divergences. Consequently, our fundamental understanding of chemistry has expanded along with the observations of our universe.

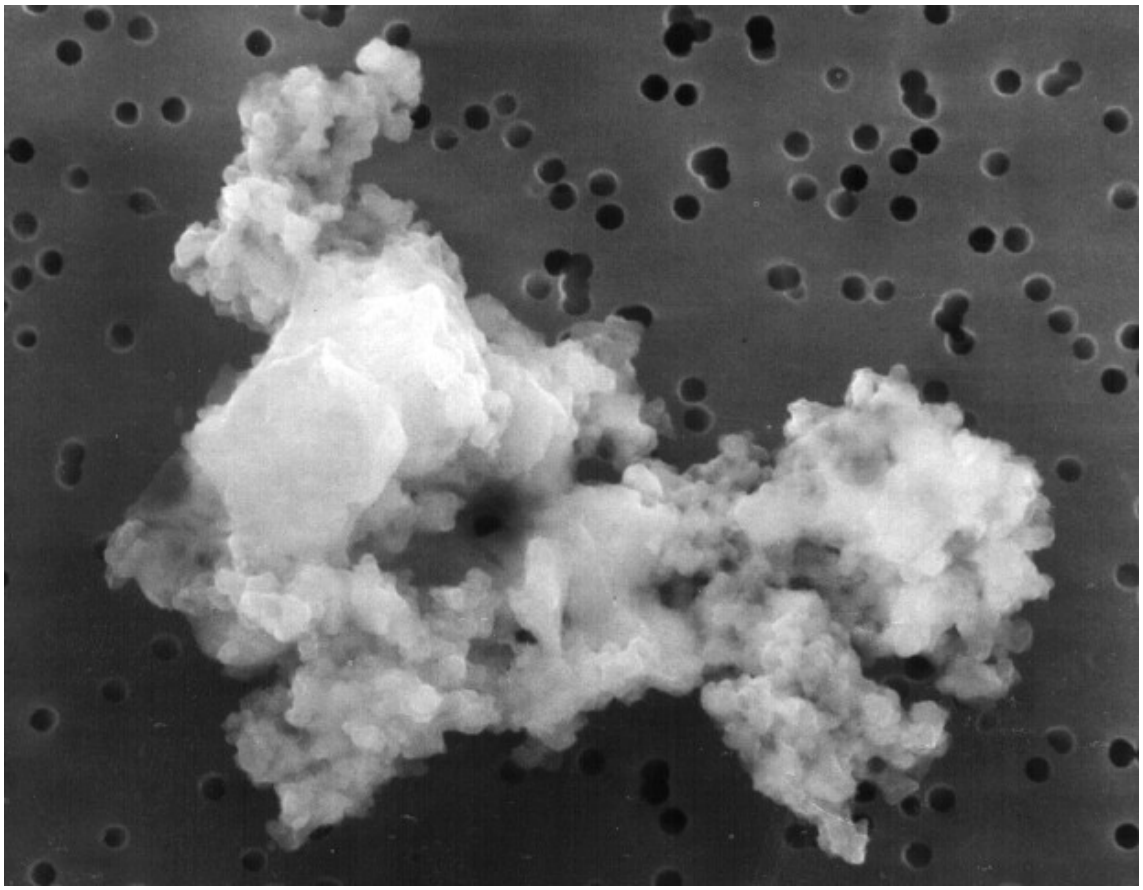

Figure 1.1: A 10-micron interplanetary dust particle collected within the stratosphere. This image was taken from NASA describing the STARDUST mission.[91]

Through the growing field of astrochemistry, we have come to learn there are regions full of gas and dust in our universe. Dust is an irregularly shaped surface composed primarily of carbonaceous and silicaceous compounds. An image of an interplanetary dust grain, which is much larger than their interstellar cousins, is shown in Figure 1.1. While the image demonstrates the irregular structure, grains undergo significant processing for interstellar dust to transform into their solar system counterparts. This includes the aggregation of many interstellar dust particles to form larger grains. In some regions, gas densities are sufficiently high (ranging from 10^2 to 10^5 cm^{-3} for diffuse and dense cold

clouds, respectively) to enable chemical interactions and the formation of multiple-atom species (molecules); more than 200 different molecules have been detected and confirmed in the ISM at this point, and it is an ever growing number. Regions known as molecular clouds (MCs) are prime candidates to study ISM chemistry because of their increased gas densities () and low temperatures (∼10 K). MCs are also called stellar nurseries because the gas is dense and cold enough to lead to a gravitational collapse of the material to a star. Again, the physical parameters dictate the chemistry where MCs are sufficiently cold enough to promote solid-phase chemistry or the sticking of gas-phase species to dust particles to form ice mantles. Atoms (H, N, etc.) and often simple molecules (e.g. CO) are directly deposited onto the grain surface and subsequent diffusion and reactions create more complex species. Complex chemistry may occur in the gas phase, but may become much less efficient because of kinetic and thermodynamic limitations.

Infrared spectroscopy has driven by our understanding of ices in young stellar objects.[92, 41, 66, 8] The grain core as briefly described above is surrounded by an ice mantle components, shown with different colors in Figure 1.2. The most common component of the ice is water, produced through hydrogenation reactions of atomic oxygen. Figure 1.2 shows an example absorbance spectrum taken toward the massive young stellar object (YSO) or the protostar AFGL 7009 S using infrared spectrometers aboard the Infrared Space Observatory (ISO). Ice components are identified using infrared spectroscopy in the laboratory, which is coupled with astronomical observations like those shown. The strong ice and dust absorption features are indicated with the NH_3 hydrate in blue, the CO_2 modes in red, the CO stretching mode in green, the CH_3OH CH_3 bending mode in orange and CH_4 bending mode in yellow. The calculated spectrum for H_2O ice at 10 K is shown in a black dashed line with features that can be identified in the ice absorbance spectrum (Fig 1.2).

1.1 Stellar Evolution

In order to understand thermal processing that occurs that transforms interstellar dust to interplanetary dust, we must discuss heritage and the formation of stars. The Big Bang produced primarily H and He, but as is apparent many other atoms have since been produced. The atoms within us were forged in stars, then released and recycled and used for molecules. As many scientists have coined, "we are star stuff." And our heritage goes as far back as the formation of molecular clouds. A graphic, Figure 1.3, is used to show a simplistic view on the stages of stellar evolution. The first stage is a giant molecular cloud (MC) of gas and dust that will clump together; as the name implies massive, MCs are heavy enough that they undergo clumping eventually leading to gravitation collapse. The result is a rotating protostar surrounded by the outer material of the cloud. The protostar rotation quickens as the collapse continues to maintain angular momentum and a resulting disk is formed. Protostars eject material through bipolar outflows until stable. Accretion of material onto the new-formed star stops once radiative pressure is strong enough to blow away the internal part of the disk reaching a new found stability. The remains are called a proto-planetary disk. Within the disk, ice and dust can aggregate to form planetesimals which then become planets, satellite, and comets. The formation of these objects is not fully understood but likely ices on grains provide adhesive properties

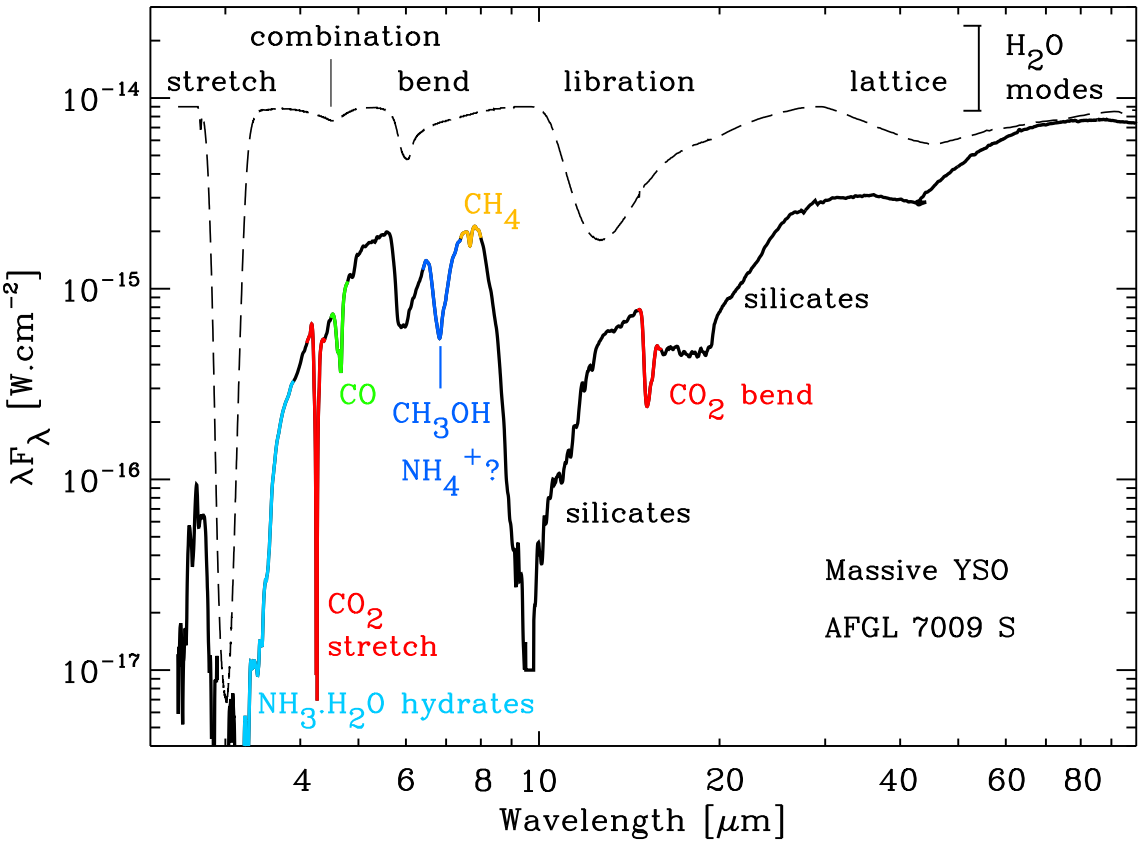

Figure 1.2: Example ice spectrum taken in absorption showing ice and dust features in the massive young stellar object (YSO) AFGL 7009 S. The black dashed line shows the calculated spectrum of IR absorption of H_2O at 10 K. The various modes are shown to show each contribution to the total spectra. This image is modified from Figure 1 of Boogert et al. 2015 and originally reported in d'Hendecourt et al. 2001. [8, 28]

for micron-sized grains to stick together, forming the intermediate stages of comets and planets.[42] The ice-y glue has an unknown origin: is it inherited from the molecular cloud stage or is it altered and processed? Cleeves et al. 2014 investigated the deuterium to hydrogen ratio for water in hopes of answering this question and it was found deuterium fractions of H_2O in our own galaxy are inadequate without inheritance from the MC stage.[19] If our solar system is considered standard then it is anticipated that inherited material should be available to planetary systems. Within the disk, regions closer to the young star will be much hotter and the heat will dissipate further away from the star. The resultant heat gradient will dictate chemistry including snowlines, which dictates the temperature where condensation occurs for each individual species. This explains our own solar system structure where inner planets are made of rocky bodies and outer planets are composed of more volatile gaseous species.

1.2 Chemistry

As discussed above, inheritance is an important aspect that must be considered when discussing the chemistry from one stellar stage to the next. A diagram of protostellar

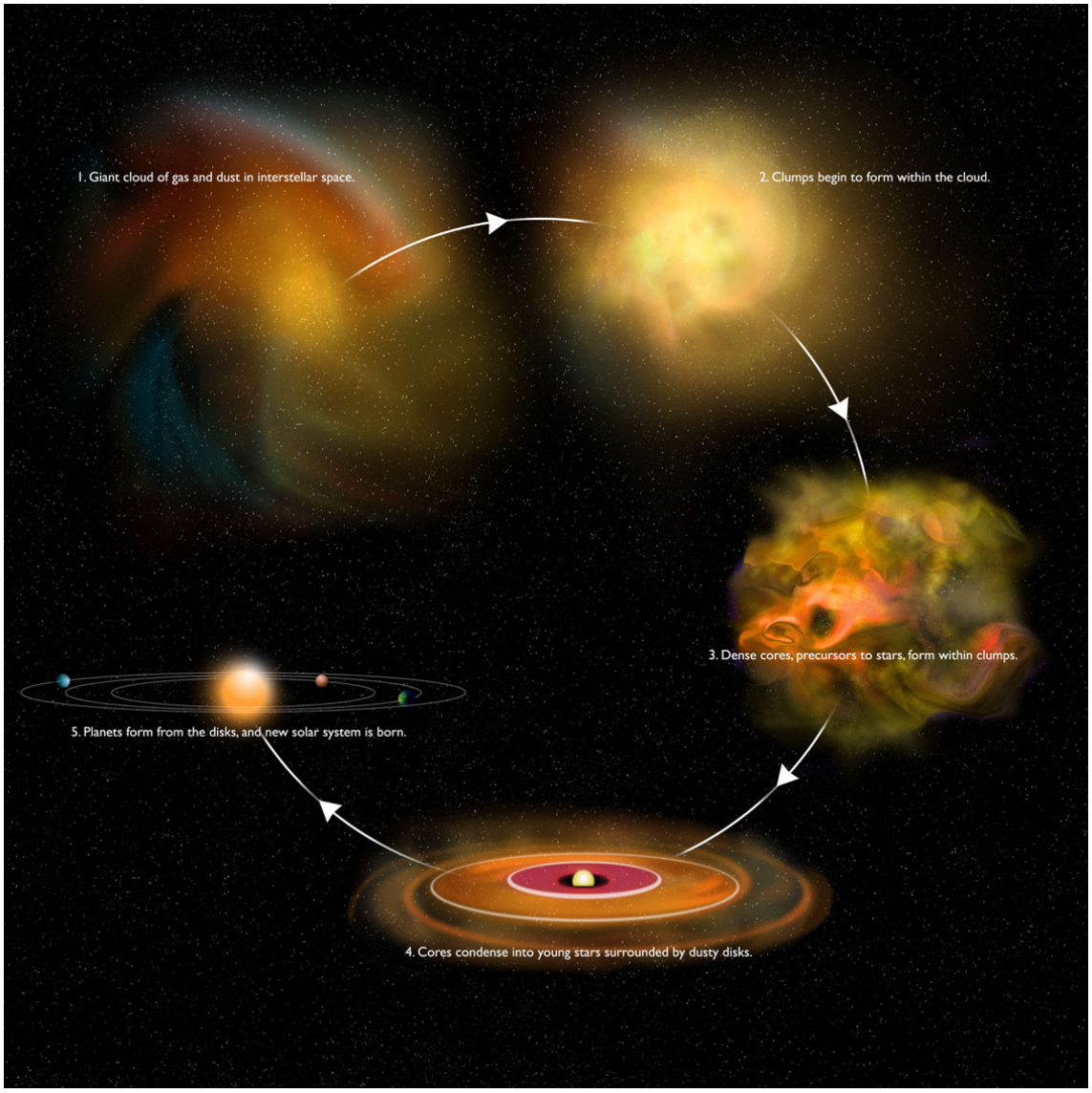

Figure 1.3: Each stage of the astronomical cycle of star formation is numbered in chronological order. The stages are giant cloud i), clumping begins ii), continued collapse until star ignition iii), eventually the rotation of the collapse leads to a disk iv). v)The disk then evolves planets, satellites, and other bodies which resemble our own solar system. [78]

physical and chemical evolution is shown in Figure 1.4a.[51] At temperatures relevant to molecular clouds, atoms and molecules such as H, C, N, and CO can stick to grain surfaces. H only sticks temporarily and will diffuse on the grain before desorbing if reaction or trapping has not occurred. CO, the second most abundant molecule in ices led by H_2O,[66] can react with atoms such as hydrogen and form methanol(CH_3OH)[88, 17] and a side product of glycolaldehyde[34], a precursor to ribose.[73] If the cloud undergoes collapse into a protostar the temperature will increase and this will heat local ices increasing the rate of diffusion and or reaction and potentially causing sublimation into the gas phase. The release of each individual molecule is dependent on the chemical composition and structure of the surrounding ice.[22, 21, 38, 32] Figure 1.4 panel a indicates the approximate temperatures at which CO will desorb from ices (CO evaporation) and stick (CO freezeout). The temperatures indicated were determined using experiments like those in panel b taken from Fayolle *et al.* 2016. [32] The experiment involves the heating

of an ice and the observation of desorption through mass spectroscopy. Experiments such as these are discussed in more depth in Section 1.4 of the introduction.

As the star condenses and heats up, the surrounding gas and dust will heat up and release ice components depending on their interactions with the surrounding material. **To understand properly how interstellar ices sublimate and re-condense, we must understand the physical surfaces they form on and how the local conditions control these structures. These effects will be crucial to determine ice behavior in protoplanetary disks, and the gas-phase chemistry that results from ice sublimation in various star-formation environments.**

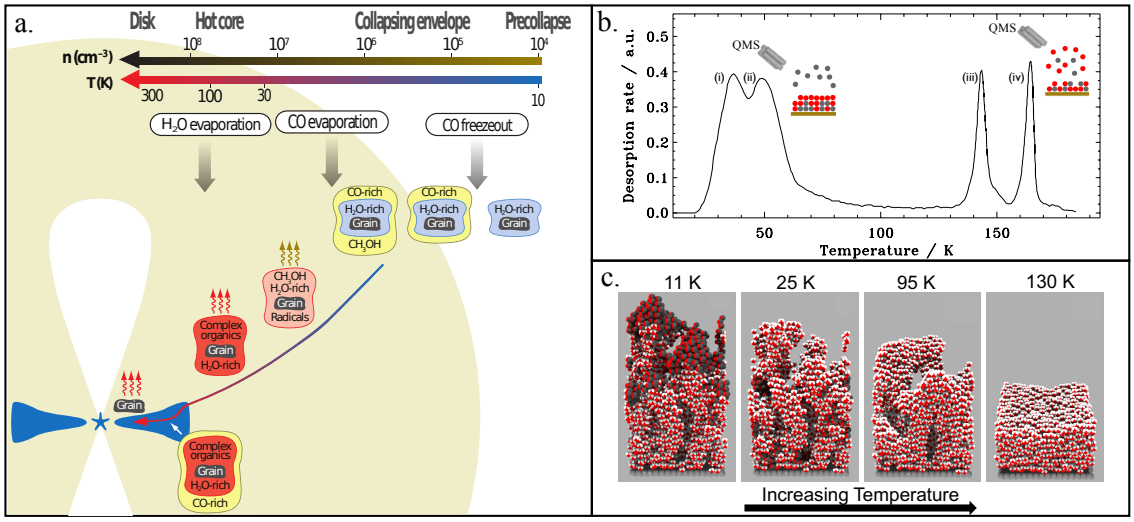

Figure 1.4: Depiction of the star formation process where the arrows indicate the physical evolution during the stellar evolution from prestellar stage and the final stage, the disk. **Panel a** is an adaptation from Herbst & VanDishoeck (2009) describing protostar evolution and its corresponding chemistry.[51] The temperature increases from right to left along with the density. The response of CO to the changing physical parameters is shown in tandem. In **panel b** there is a temperature programmed desorption profile from laboratory experiments.[32] The temperature is shown on the x-axis and CO desorption rate on the y-axis. At regions i and ii, CO is leaving the surface either from a CO-rich environment (i) or a water-rich environment (ii). Stages iii and iv correspond to CO leaving during the rearrangement of water (iii) and sublimates from the surface (iv). **Panel c** shows a model of a layered CO and H_2O ice and how the structure changes with temperature. At 11 K the original layered ice is shown. The next temperature, 25 K, shows CO has diffused into the pores of the H_2O ice where some CO may become trapped until the rearrangement and desorption of H_2O. At 95 K the H_2O has begun collapsing and the last temperature shows the water ice before desorption.

1.3 Dust and Ice

1.3.1 Dust Grains

Interstellar dust or grains (typically 1% of mass in clouds) are particles around 0.1 μm in diameter, composed primarily of carbonaceous and silicaceous compounds. Atoms and molecules can accrete or deposit onto the grain surface at low temperatures or high pressures, thereby building up a surrounding ice layer. On the grain surface, atoms

and molecules can diffuse, react, or desorb, which is influenced by its own molecular properties, the surrounding components, the physical structure of the ice (i.e. pores), and the temperature of the grain. Dust acts as a catalyst in low density environments, providing a place for multiple atoms to meet and react. For instance, H_2, the most abundant molecule in the ISM, is primarily formed on grains because the grain provides a sink for the extra energy released when 2 or more H atoms combine, which would otherwise break apart the bond in the gas phase.[85] The largest components of ice mantles, in order of most- to least-prevalent, are H_2O, CO, and CO_2. [41, 67]

In addition, grain surfaces are important for their shielding properties.[5] Stars, being excellent radiators of ultraviolet light, will destroy molecules into simpler components, but grains in the outer shell of a cloud can absorb or scatter radiation and protect newly-formed molecules within the cloud. This provides an environment for further complex chemistry to occur, possibly building up to biologically-important molecules, often described as complex organic molecules (COMs), on ices. The chemistry, of both the grains and COMs, is important for star-forming regions, because it is theorized life on planets like our own was either seeded with biologically-important molecules initially on early Earth or comets delivered them upon impact.

1.3.2 Amorphous Solid Water

When temperatures are cold enough, atoms and molecules will physisorb or deposit onto grains (E$\sim$10-400 meV) or grain analogs, which will be discussed further in the laboratory setting. Chemisorption (E$\sim$1-10 eV) can also occur, in which bonds form between the impinging particle and the grain, but this is beyond the scope of this work. Water ices physisorbed to grains in the ISM are found to be primarily amorphous, or in a disordered state, and can contain large, empty pockets called pores. Amorphous solid water (ASW) is a major component of astronomically-important structures, including comets, planetary rings, satellites, and mantles on interstellar grains. [44, 72, 58, 41, 67]

The formation of such an ice structure is dependent on many parameters, including the formation timescale, temperature, pressure deposition angle, and deposition rate. Astrochemists use laboratory studies to understand ices in the ISM, but the parameters used can, often, be different, thus, the ice structure made may not truly represent an ISM ice structure. One difference between lab and interstellar ices is how H_2O is delivered to the grain. In the ISM, it is thought that H_2O is formed through reactions of hydrogen and oxygen atoms on grains, but, in most laboratory experiments, H_2O is directly deposited on the surface. This is not a fault of experimentalists as directly depositing water simplifies the chemistry and prevents chemical reactions that are unwanted. The different formation mechanisms likely mean that lab ices are more porous than interstellar ices. [55, 40] Further, the ices may undergo radiation and thermal processing reducing the porosity.

1.4 Laboratory Experiments

Astrochemical experiments can be used to study the structure of water ice, and further they are an essential component to understanding the chemistry and processes that occur

in the ISM because they can help identify species in the gas- and solid-phase, confirm the viability of proposed reactions, and find reaction rates reaction barriers. To ensure laboratory-made ices are as similar as possible to interstellar ices, experimentalists have studied ices created under similar conditions to dark clouds or MCs (low pressure and temperature). To maintain low pressures, vacuum chambers are utilized and maintained with pressures of 10^{-10} Torr. Cryogenic targets within the ultra-high vacuum chambers can be cooled to temperatures as low as 8 K, temperatures similar to MCs. While these values are typical, each experimental setup varies and may produce slightly different results from one another. Spectroscopic methods such as infrared spectroscopy, mass spectroscopy, and many more tools are used to discern chemical and physical properties of ice.[7, 12, 57] In laboratory experiments, two forms of ASW can be formed during deposition—porous and compact—depending on temperature and pressure. The structure of ASW depends on the deposition methods. [83, 57, 29, 75] Generally, lower deposition temperatures and higher deposition angles (where 0° is normal to the surface) favors a higher porosity. Important studies, performed by Kimmel *et al.* 2001 and Berland et al 1995, investigated the effects of deposition angle and deposition temperature and rates, respectively, on ice compactness. Kimmel *et al.* [2001] studied the adsorption of N_2 into ASW as a means to track porosity. They found that increasing the angle of the doser, source of the incoming gas, creates a greater glancing angle, yielding a more-porous ice; deposition at a normal angle produces ices with little to no porosity. Berland et al. [1995] found background deposited ices at increasing temperature increases the density, while decreasing accretion rate increases the density.

Berland used background water in the vacuum chamber for deposition as opposed to a doser next to the surface, meaning the ice was deposited where each molecule will come in at seemingly random angles known as “background" dosing. Background deposition will produce the most porous ices at low temperatures.[57, 20] Studies have shown that both increasing the deposition temperature [16] and decreasing the deposition rate increase the density. [7, 12] Some studies have shown no temperature dependence when depositing ices using the uniform angle method but with various angles.[90, 57]; this may be accounted for by the various deposition parameters like the kinetic energy each incoming particle may have.

The pore structure of ASW is important because it allows trapping of other chemical components, such as CO, CO_2, NH_3, CH_3OH, and, potentially, more chemically complex species. This feature will dictate when desorption of gases trapped in pores into the gas phase occurs altogether changing both the surface- and gas-phase chemistry. As one would imagine, the ability for molecules to incorporate into the ice is highly dependent on the water structure. For instance, porous ASW (densities as low as 0.6 g/cm^3) can absorb 20 to 50 times more gas than a compact, non-porous ASW.[4] The efficiencies of complex reactions, within the ASW, between incorporated molecules are highly dependent on the structure and porosity. For example, the hydrogenation of CO into e.g. formaldehyde and methanol is more efficient in ASW ices over crystalline ices due to the trapping of incorporated CO within the pores. The effect of ASW structure on the occurring chemistry is an active area of research. [52, 89]

Finding desorption temperatures or energies is vital in this mission to understand inheritance from one stage of stellar evolution to the next. One method used in finding the desorption temperature or the binding energy is temperature-programmed desorption (TPD). In this technique, a molecule of interest is typically vapor deposited individually or with other gases on the desired surface and heated at a linear rate until all molecules

have desorbed. A desorption-rate profile is generated by measuring molecule desorption by a mass spectrometer as a function of temperature. In Figure 1.4b, CO desorption features are indicated with numbers i - iv and each desorption peak corresponds to CO leaving from a different environment (i.e. different ice composition or morphology).[32] At regions i and ii, CO is leaving the surface either from a CO-rich environment (i) or a water-rich environment (ii). Stages iii and iv correspond to CO leaving during the rearrangement of water (iii) and sublimates with water from the surface (iv). The presence of two initial peaks indicates a difference in the interaction between CO with itself and H_2O. CO interacts more strongly with H_2O indicated by the higher desorption temperature.

The rearrangement and resulting compaction of water ices has been demonstrated.[9] The pores within the ice structure undergo a collapse until the ice has reached its maximum density around 0.9 g/cm^3 in accordance with the density observations from Brown et al. [1996]. Around 140 K the ice will also undergo a phase change from amorphous to crystallin ice. By 160 K all water will have desorbed from the surface along with all trapped volatile species. As discussed briefly with H_2O and CO as an example, TPD profiles will have unique profiles depending on the ice composition and structure, aiding in the identification of ice components. [21] The resulting spectrum can be fit using analytical methods, and binding energies can be calculated. TPD curves are typically fit using the Polanyi-Wigner equation:

$$\frac{-d\theta}{dT} = \frac{\nu}{\beta}\,\theta^n\, e^{\frac{-E_{des}}{T}} \tag{1.1}$$

where θ is the ice coverage, T (K), ν is a pre-exponential factor (s^{-1}), β the linear heating rate (K s^{-1}), n the kinetic order of the desorption process, and the desorption energy is E_{des} (K). Boltzmann's constant is not used here as the temperature and desorption energy are in the same units (K). These fits do not take into account the porosity of ices, which may change the surface area and hence the coverages. For example, a porous water ice has significantly more surface area than a compact ice, increasing the coverage needed to saturate the surface. While the results from experiments are valuable, modeling is an essential part to fully understand ice chemistry. Further, the discrepancies in conditions and the ice structures from the laboratory to interstellar conditions raise the question whether the ice analogs used are a sufficient substitute.[40, 20].

Given the importance of the ice morphology to interstellar and protoplantary chemistry, models are required that can simulate structure in both laboratory and interstellar conditions, extrapolating lab results reliably to interstellar conditions and timescales.

1.5 Purpose of Work

The formation of molecules on grain surfaces, and the subsequent production of COMs, has been demonstrated in laboratory experiments. However, interstellar physical conditions can never be exactly reproduced, and the timescales are vastly different (hours in the lab versus many thousands of years in the ISM), making the correspondence of the two regimes highly uncertain. To address this divide, we will model the fundamental micro-

scopic processes that govern the formation of molecules and the structure of ices. Using an off-lattice kinetic Monte Carlo model, we will investigate the processes, timescales, and chemistry that govern laboratory ice formation and structure with a focus on two of the most abundant molecules within ice mantles: H_2O and CO. We will apply the model to astronomical conditions to explore interstellar ice formation and structure. This will allow more extreme conditions of the interstellar medium – currently inaccessible in the laboratory – to be explored, and the fidelity of interstellar ice analogs to be assessed.

Scientific Objectives

1. **Investigate how ice composition and structure relate to desorption temperatures in protostellar sources.**
2. **Investigate the main influences on ice structure, trapping and diffusion.**
3. **Resolve the relative timescale dichotomy between the laboratory and interstellar medium and the resulting effects on chemistry.**

Technical Objectives

1. **Reproduce and quantify characteristics for the main components of interstellar ices (H_2O and CO) based on existing laboratory data.**
2. **Measure and fit diffusion, trapping, and desorption of the ice components.**
3. **Measure structure of ices formed from the hydrogenation and other subsequent reactions and compare to ices produced using direct deposition.**

1.5.1 Organization of the thesis

The topics discussed in each chapter will touch on the aforementioned objectives. First, the original model will be briefly introduced. Then the improvements that have been implemented will be explained. Chapter 3 onward will include the application of the model. The first topic includes the structure of pure water ices using various deposition parameters. The next application was a natural extension of chapter 3 where the surface area of water ices is discussed alongside laboratory experiments that measure the infrared absorption spectra of CO on porous amorphous solid water (Chapter 4). After establishing the reliability of the model in producing water ices, we provide insight into the diffusion of CO on amorphous water ices with various morphologies (Chapter 5). The diffusion was first established followed by desorption, as we will show diffusion dictates the amount of CO that can be trapped during the desorption process (Chapter 6).

List of publications:

1. Jiao He, Aspen R. Clements, SM Emtiaz, Francis Toriello, Robin T. Garrod and Gianfranco Vidali, *The Effective Surface Area of Amorphous Solid Water Measured by the Infrared Absorption of Carbon Monoxide*, 2019, ApJ

2. Aspen R. Clements and Robin T. Garrod, *Microscopic simulations of laboratory and interstellar ice structure and chemistry*, 2019, IAU Proceeding

3. Aspen R. Clements, Brandon Berk, Ilsa R. Cooke and Robin T. Garrod, *Kinetic Monte Carlo simulations of water ice porosity: extrapolations of deposition parameters from the laboratory to interstellar space*, 2018, PCCP

4. Aspen R. Clements, Isla R. Cooke, Robin, T. Garrod *Monte Carlo Modeling of Astrophysically-Relevant Temperature-Programmed Desorption Experiments*, 2017, IAU Proceeding

   In preparation:

5. Aspen R. Clements, Ilsa R. Cooke, Jake A. Butler, Edith C. Fayolle, and Robin T. Garrod *Characterization of Diffusion of Carbon Monoxide in Amorphous Solid Water Utilizing an Off-Lattice Monte Carlo Model*

6. Aspen R. Clements, Ilsa R. Cooke, Edith C. Fayolle, and Robin T. Garrod *Kinetic Monte Carlo modeling of Temperature Programmed desorption experiments: H2O and CO ices*

2

Off-Lattice Kinetic Monte Carlo Model

Contents

Astrochemical models have primarily consisted of rate equation methods, as they are fairly straight-forward and computationally inexpensive. In the rate equation models, each species has a differential equation associated with its formation and destruction, and its abundance can be monitored through time. A series of nonlinear differential equations are solved at each time step to calculate these abundances. While the method is invaluable for gas-phase chemistry, the solid phase requires a more-thorough treatment [82, 26] because rate equation methods cannot account for the structural components like ice porosity. The most relevant example for this work is the simplification of barriers for diffusion and desorption. For instance, the diffusion barrier is typically assumed to be 0.3 to 0.5 times that of the desorption barrier, while a spectrum of values would be more physically realistic.

One resulting problem from the simplifications is the over- or under-production of some species in regimes where the competition between diffusion and desorption controls production. A method used to further understand solid-phase astrochemistry is Monte Carlo modeling, first used in the field by Tielens & Hagan. [84] In particular, microscopic Monte Carlo codes can be useful in understanding grain ice mantle structures because particle locations can be directly monitored. Initial models were used to understand the macroscopic properties, like abundances on the grains, but did not follow the molecule movement within the ice mantle and the corresponding structural and chemical changes.

Without knowledge of the location of each species, the structure of the ice is unknown and how barriers are affected remains unclear. Using conditions ranging from the laboratory to the ISM, ices can be simulated, and the effects of deposition angle, temperature, and density can be quantified.

Monte Carlo models utilize randomly-generated numbers to determine which process will occur in a given time interval. The Markov chain Monte Carlo method is utilized where the ice and all of its components are explicitly placed. A Markov chain by definition provides a model that describes a sequence of possible events and the probability for each event which depends on the previously achieved state. For example, an empty surface may accrete a particle. The next set of events that could occur would be accretion of another particle, diffusion or desorption of the original particle on the surface and their rates would depend on details of the current state.

2.1 MIMICK

We use an off-lattice microscopic kinetic Monte Carlo model called *MIMICK* (Model for Interstellar Monte Carlo Ice Chemical Kinetics) to simulate laboratory ices and when applicable interstellar and protoplanetary conditions. By using a microscopically-detailed model we can apply the methods fairly easily to all regimes, and laboratory results may be extrapolated directly to interstellar conditions; this allows us to test how closely laboratory ices represent interstellar ices. An off-lattice model was developed to better replicate the intrinsic disorder of amorphous ices. On lattice models calculate rates beforehand, limiting moves to discrete positions potentially preventing surface species from finding local minimum. Further, an on-lattice approach cannot account for individual species sizes.

The predecessor of this model is discussed in detail by Garrod (2013). A representative model for the predecessor model is shown in Figure 2.1. The code has been adjusted to use a surface with periodic boundary conditions and will be more like the flat square surfaces used in laboratory experiments. The *MIMICK* model is based around the need to simulate surface diffusion kinetics, which is governed by kinetic rates. The model therefore traces the positions of entities that could plausibly engage in surface diffusion – either atoms or molecules (including radicals). Thus, where a molecule exists, it is treated as a self-contained entity, rather than as separate atoms. All binding between entities on the surface is of a van der Waals-type nature; no chemical bonds are considered (except implicitly, within molecules). Furthermore, all physical interactions between surface entities are described by isotropic pairwise potentials, making all surface species effectively spherical. We therefore refer to all independent entities as "particles", whether atom or molecule.

We use the same treatment of time evolution and process selection as Gillespie (1976). The time progresses by first selecting the process that will occur next and then how much time elapses after the process occurs. Each chemical process (deposition, diffusion, desorption, or reaction) is assigned a rate. Reaction, desorption, and diffusion require

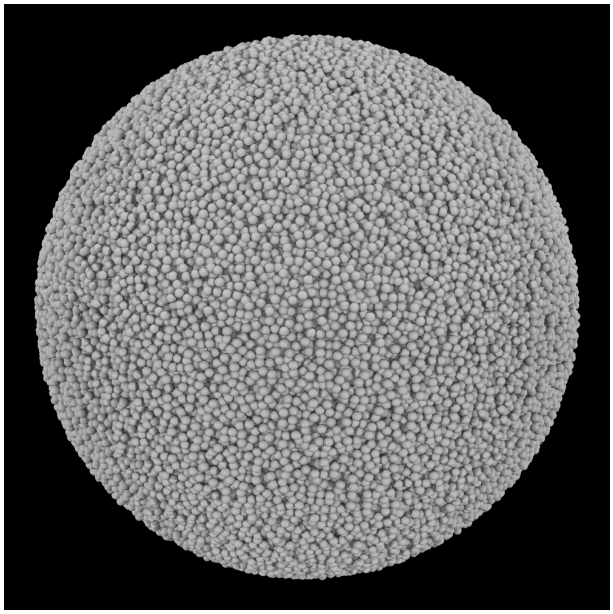

Figure 2.1: POV-Ray image of grain with individual atom in grey. This particular grain was used in Garrod et al. 2013 as an analog to interstellar grains.[40]

a rate for each individual particle as this will vary depending on local conditions. Each process is assigned a probability by taking a ratio of the process rate and the sum of all rates and a random number is used to select the process. Then, another random number determines the time elapsed by

$$\Delta t = -\ln(N_{ran})/R_{tot} \tag{2.1}$$

where the random number generated, N_{ran}, is different for the process selection and the time elapsed and R_{tot} is the sum of all of the rates. The code has been adjusted to use a surface with periodic boundary conditions, and now includes a relaxation process discussed later in this section 2.2.1. Important features of the code used here are described below.

Figure 2.2 shows a simple representation of the flow of computational processes used in *MIMICK*. The main loop of the model involves: the evaluation of rates for every possible physical/chemical process that could happen; the random choice of a single process to occur as the next event (with probabilities weighted according to the magnitudes of each rate); the carrying out of the chosen process; and the advance of the time parameter. All physical/chemical events occur sequentially, with rates dependent on the outcomes of previous events. The model ends once the final time or the desired coverage has been reached; the desired coverage is achieved when the number of molecules/surface area is equivalent to the number of layers desired. The number of layered is defined by the number of deposited particles divided by the surface sites on the bare substrate or in other words the ratio between the number of molecules and the surface size. This is a simplistic measure of thickness as the deposited species likely will have some irregular structure or gaps in each layer. The model traces the positions of all particles on the surface at all times, as various deposition, diffusion and desorption processes occur.

Because *MIMICK* is an off-lattice model, there is no pre-determined grid of allowed positions for particles; all particle positions are determined through the minimization of the sum of pairwise potentials that they experience due to interactions with other surface

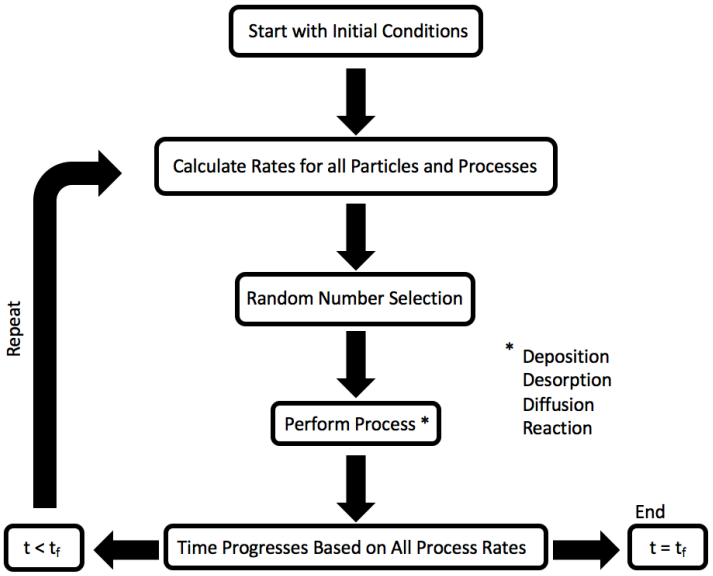

Figure 2.2: Basic flow chart of the operations carried out within the kinetic Monte Carlo code *MIMICK*.

particles. Since the constant global minimization of potentials would be prohibitively expensive in computational time, only the position of a particle that has just accreted or diffused is optimized. Low temperature ices with amorphous structures are best treated using an off-lattice model, where disorder is inherent. The off-lattice treatment allows amorphous surface structures to form containing pores.

The model starts with certain pre-defined initial conditions, which consist of a bare substrate surface at some temperature. This surface is constructed of two layers of atoms fixed in a body-centered cubic arrangement; the substrate surface atoms are not allowed to move during the simulation (although water and carbon monoxide molecules are), but each one produces an isotropic pairwise potential with any deposited particle that comes close enough to interact. The highly-ordered substrate surface employed here is not very representative of interstellar grain surfaces, which are expected to have irregular or fractal geometries, but it is a good basis to compare to laboratory experiments, which often use regular surfaces such as well-defined metal or ionic crystalline surfaces. Periodic boundary conditions in the lateral directions are utilized, to allow a small section of surface to represent a large experimental surface. A series of surface sizes ranging from 46×46 to 160×160 atoms is used to ensure that structural features remain smaller than the scale size of the ice.

The only process which may occur at the very beginning of the simulation, where the surface is clear, is the deposition of a particles from the gas phase. All deposition events consist of the placement of a new particle at a starting position at a fixed height far above the surface, whose lateral position is randomized in the x and y directions. If so-called background deposition is assumed, then the velocity vector of the incoming particle is randomized over the solid angle of a hemisphere centered on the starting position. In the case of fixed-angle deposition, the velocity vector is pre-determined and uniform for all deposition events (for chapter 3 and have updates described in section 2.2, which are the used model for chapters 4, 5, and 6). The trajectory is then gradually advanced until a surface particle (either a water molecule or a substrate atom) is encountered. The

progression of the trajectory is then halted, and the position of the incoming particle is optimized according to local pairwise interactions with surface particles.

The positions of surface particles, following deposition or diffusion, are determined by calculating local minima via a Lennard-Jones potential. A Lennard-Jones (LJ) potential is an accumulation of repulsive and attractive forces, where the repulsion term, accounted for by the power of 12, is due to Pauli exclusion or repulsion, and the attractive force term, the term to the 6th power, is due to van der Waal forces.

$$V = \epsilon\left[\left(\frac{\sigma}{r}\right)^{12} - 2\left(\frac{\sigma}{r}\right)^{6}\right] \tag{2.2}$$

Where r is the distance between the selected particle and neighboring particles, ϵ is the depth of the potential well, and σ is the distance at which the intermolecular potential goes to zero. The model parameters (σ and ϵ) are tuned for each molecule in question, H_2O and CO. The determination of mean molecular desorption energies from the model provides another measure of the fidelity of the model to macroscopic properties.

In practice, the above expression is adjusted, such that the potential gives a zero-value at a distance of 2.5σ or beyond. This is achieved by adding a small modifier to the expression in square brackets, then applying a small scaling factor to ensure that the potential minimum is fixed at ϵ. The standard expression would return a value around 0.8% ϵ at the truncation distance. The truncation of the potential simplifies the calculations and is acceptable given that long-range interactions are of limited interest for the amorphous ices that are simulated here.

The kinetic rates, such as diffusion and desorption, and how they are determined are briefly described in here, but a full description is provided by Garrod (2013)[40] and Garrod (*in prep.*). The accretion/deposition rate is treated as a free parameter and is changed based on the desired conditions (10^1 to10^6 molecules cm^{-2} s^{-1} for the ISM and protoplanetary disks, respectively and 10^{13} to 10^{16} molecules cm^{-2} s^{-1} for laboratory conditions).

The general temperature-dependent rate for thermal desorption or diffusion of a surface particle i is shown in equation 2.3, where ν_i is the characteristic vibrational frequency of the molecule, $E_{i,n}$ is the energy or barrier for process n, and T is the surface temperature.

$$R_{i,n} = \nu_i \exp(-E_{i,n}/T) \tag{2.3}$$

The characteristic frequency for each individual molecule is determined using a one-dimensional harmonic oscillator relation[45] based on the desorption energy of the molecule. The desorption energy (K) is simply the sum of all pairwise interactions with nearby particles ($r \leq 2.5\sigma$). This is a departure from the method used by Garrod (2013), in which only contributions from contiguous particles were considered, which resulted in binding energies that were exactly proportional to the number of nearest neighbors. Here, weaker, somewhat longer ranged interactions are also considered, which produces a less discrete distribution of binding energies across all particles on the surface. The pairwise interactions for each combination of particles is shown in Table 2.1.

In the past version of the model[40], a successful desorption event led to the immediate removal of the desorbing particle from the surface. Here, a desorbing particle is assigned an outward trajectory vector, which is calculated simply as the vector sum of pairwise bond directions (unit vectors) for all immediately contiguous binding partners. pairwise

Table 2.1: The pair-wise interactions in Kelvin for the species of importance to the models presented here. The interactions to the grain are adequately high to ensure sticking at reasonable temperatures.

	Grain	H_2O	CO
H_2O	550	850	210
CO	120	210	120

binding strengths are not considered in the calculation of this direction vector. This vector sum therefore represents the mean geometric normal to the local surface. The particle trajectory is then traced outward until it exits the upper boundary of the simulation, or it collides with another surface particle, at which point it is re-adsorbed onto the surface, following the same procedure as regular deposition. This "re-accretion" process is important in cases where a particle desorbs from inside a pore.

Diffusion barrier calculations are more complicated than the determination of the desorption energy, as these barriers are dependent on the spatial arrangement of the surrounding particles. Due to the amorphous nature of the ice that is produced in these simulations, not all diffusion pathways have the same barrier. To determine the number and directions of diffusion pathways, it is assumed that diffusion always occurs through local saddle points, which may be found by allowing the diffusing particle to rotate around an axis that joins a pair of surface particles that are contiguous with the diffuser (although not necessarily with each other). Simple geometric checks are also carried out to ensure that such pathways are physically allowed, and not immediately blocked by another particle. As explained by Garrod (2013), a plane may be defined that intersects with the initial position of the diffusing particle and the positions of the pair of particles that define the saddle-point. The positions of all other particles immediately contiguous with the diffuser are then assessed in relation to this plane; if all these surrounding particles fall on only one side of the plane or the other, then diffusion around the specific "saddle-point pair" is allowed. If one or more contiguous particles is on the other side of the plane from the others, then diffusion around the pair in question is deemed to be obstructed, and is not allowed. Importantly, no calculation of a post-diffusion position is carried out, until after such a diffusion event has been selected as the next process to occur in the simulation, which saves significant calculation time. For each diffusion pathway available, the energy barrier is determined by summing the energies that would be required either to break or stretch each pairwise surface bond to the furthest distance it could reach as a result of rotation around the axis, ignoring those bonds that would be made stronger by diffusion in the given direction. This method diverges from that described by Garrod (2013), which required the outright breaking of all bonds except those of the saddle-point pair. As a result, the surface diffusion barriers take on a smoother range of values, as well as generally being lower.

With the diffusion barriers for each direction determined, if diffusion by some particle or other is chosen as the next event in the sequence, the diffusing particle is rotated around the relevant saddle-point pair until it collides with one or more particles on the other side. Its position is then optimized according to its new location, in the same way as with deposition.

2.2 Changes to model

2.2.1 Relaxation Process

The relaxation process was implemented for the means for ensuring water ices produced reasonable densities in Clements et. al [2018]. [20] The description of the relaxation process was first described there and now is repeated here.

The basic *MIMICK* treatment considers only thermal diffusion. Results presented later, however, indicate that a non-thermal mechanism is also necessary. The relaxation process we introduce here accounts for the energy of an incoming particle, which can potentially allow it to hop (or indeed react, if reactive species are present) on the surface. The energy gained is a combination of the thermal kinetic energy that the particle brings from the gas-phase, and the energy gained when the incoming particle accelerates into a surface potential well at short range; the maximum energy available from this latter process is the total interaction energy of the particle with the surface, although at least some of this will be lost the inelastic collision of the particle with the surface.

In typical experiments, the gas from which the deposited particles derive is held at room temperature; we assume that it will maintain the same energy distribution when it is introduced to the vacuum chamber. In that case, the average kinetic energy is $\frac{3}{2}kT$. Expressing this energy in units of Kelvin, as is typical for astrochemical models, gives an average energy of 450 K, for a gas temperature of 300 K. It is noteworthy that such an energy is likely on the order of just 10% of the binding energy of a typical water molecule, or likely no more than one third the energy required to overcome a surface diffusion barrier for water. The kinetic energy gained due to acceleration into the surface potential well should therefore dominate the non-thermal energy available for immediate diffusion on the surface.

While detailed calculations for the efficiency of diffusion of a newly-adsorbed molecule could be obtained through a molecular dynamics treatment, this would be a major endeavour, and such calculations could not be directly incorporated into a kinetics model, due to the much greater timescales over which the kinetics models operate. The average efficiencies derived from separate MD calculations could potentially be incorporated into the present models, but even the most up-to-date MD treatments of excited molecules on water surfaces deal only with crystalline water ice[37], rather than the amorphous structure of interest here. We instead seek to implement a more empirical treatment to gauge the effects of such a process, and therefore to determine the efficiency required to reproduce experimental results using our kinetics model.

We use a Maxwellian distribution to randomly select the kinetic energy of each incoming gas-phase water molecule, $\mathrm{KE_{init}}$. Upon adsorption to the surface (into a potential well whose strength is determined according to local conditions), a kinetic energy equal to the surface potential is added to this value. An efficiency factor (between 0 and 1), α, which is a free parameter, is then applied to this total energy, which sets the initial energy available to the molecule that can be applied to hopping over a surface diffusion barrier, i.e.

$$E_{\mathrm{init}} = \alpha \left(KE_{\mathrm{init}} + PE_{\mathrm{init}} \right) \tag{2.4}$$

If the newly-adsorbed particle has a diffusion pathway accessible that has an energy

barrier, E_{dif}, less than or equal to the available energy, E_{init}, a diffusive hop spontaneously occurs. If more than one diffusion pathway is accessible, each is assigned an equal probability of occurring. Whichever hop is chosen, an energy equal to the operative diffusion barrier (corresponding to the energy cost in broken/stretched bonds) is subtracted from the available energy when the hop occurs. However, more energy is then added to the total, corresponding to the energy gained as a result of settling into the new binding site, ΔE, so that the available energy after one non-thermal hop is given by:

$$E_1 = (E_{init} - E_{dif} + \Delta E)\beta \tag{2.5}$$

where E_1 is the energy available for further hopping after 1 non-thermal hop; β is a second efficiency factor (also between 0 and 1) that accounts for inelastic losses associated with the particle's motion into the new binding site. The energy gained by moving into the new binding site, after factoring in the loss associated with leaving the old one, is defined by:

$$\Delta E = PE_1 - (PE_{init} - E_{dif}) \tag{2.6}$$

where is the total binding energy associated with the new potential well, PE_{init} is the binding energy of the first binding site, and E_{dif} is the diffusion barrier. If enough energy is available after the first non-thermal hop, another may occur, assuming one or more of the new diffusion barriers are low enough to be overcome with this energy. In such cases, the same value of β is assumed. If, at any stage, the available non-thermal energy is insufficient to overcome any diffusion barrier currently open to the particle, the period of non-thermal diffusion is over. The particle can then take part in thermal diffusion normally.

By defining global values for α and β, we allow *average* efficiencies to be assumed for the retention of kinetic energy following collisions relating to the initial impact of adsorption and subsequent diffusive hops to new binding sites. This avoids making detailed calculations of the energy losses and gains associated with each separate process, while retaining non-uniform behavior for each event that is dependent on local binding and diffusion conditions.

2.2.2 Non-linear accretion trajectory

A small change is made to the adsorption treatment in the present model. Whereas in previous versions of *MIMICK*, an incoming molecule would follow a straight-line trajectory toward the surface (whose starting point and/or direction would be randomized, depending on the deposition method), the new method attributes a velocity to the molecule (taken randomly from a Maxwellian distribution) and allows the velocity vector to adjust to the potentials that it experiences as it approaches the surface. (Again, a cutoff of 2.5σ is used). Timesteps of 0.1 m/$|v|$ are used in this calculation (with velocity units of m s^{-1}), to ensure appropriate time resolution is obtained for any incoming velocity. As in the previous treatment, when the molecule reaches the surface, the trajectory is stopped, and the position of the molecule is optimized. From there, following Clements et al. 2018, the incoming molecule may undergo non-thermal diffusion between binding sites according to its incoming energy, which is the sum of its original kinetic energy and the energy gained upon settling into its initial binding site.

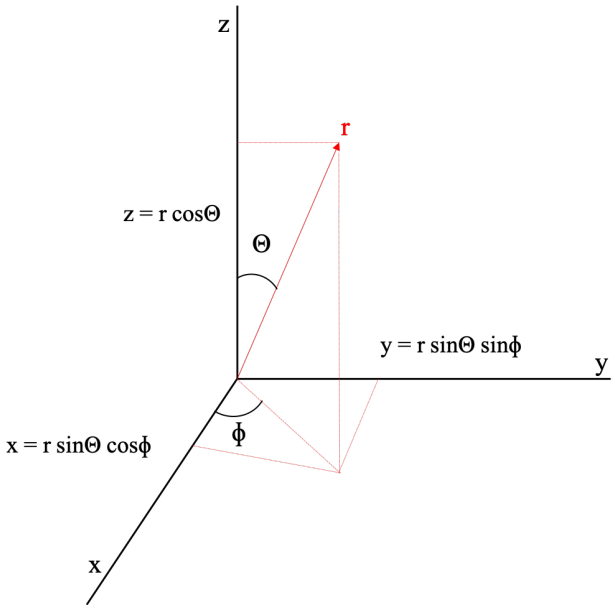

Figure 2.3

This change to the adsorption treatment ensures, for example, that an incoming molecule at an oblique angle of entry cannot skirt along the surface without interacting with it. The method may therefore be considered a crude form of molecular dynamics, and thus a step forward from the simple hit-and-stick method used in Chapter 3.

The model has a number of parameters that are changed for the purposes of changing the angle of deposition, or the angle at which particles approach the surface. Three parameters are given for the incoming particle, x, y, and z coordinates. For example, if the ice is deposited at a normal angle to the surface the coordinates for x, y, and z would be 0, 0, and 1, respectively. When utilizing random angles for each incoming particle two random numbers are used to generate random angles for θ and ϕ using:

$$\Theta = 2\pi N_{ran\,1} \tag{2.7}$$

$$\Phi = cos^{-1}(2\pi N_{ran\,2} - 1) \tag{2.8}$$

where each random number is generated separately from 0 to 1. If an outward trajectory is generated, it will be reversed to ensure inward trajectory. This ensure cases are counted once. A simple schematic is shown how spherical coordinates relate to cartesian coordinates, a calculation within the model. The random θ and ϕ are then used to calculate the vector components, x, y, and z. The conversion is shown in Figure 2.3.

The incoming particle will then approach the surface with the direction described above. The position is incremented until a bond can be found. The original version of the model did not account for interaction of the trajectory with the potentials of the surface and ice. Likely the particles on the surface, because of the nature of the potential of water, will provide additional acceleration towards the ice. Indeed, we found pure water ices produced densities lower than those described in chapter 3 (Clements et al. 2018 does not include the changing trajectory). The densities are lower because of the combined potential was high enough to pull each trajectory in sooner than the original model. The relaxation parameters needed to be raised slightly to reproduce the results

in Chapter 3, but we believe this change will become more important when considering a heterogenous ice mixture.

2.2.3 Species with different sizes

Previously, all species were treated with a uniform size, radius of 1.6 Å. As these projects progressed it became apparent that volatile species should be treated with their own sizes especially when considering physical properties such as trapping. One can imagine an instance of a pore width being able to exclude large species. The size of each species is a parameter defined within the model. For the work presented the most pressing molecules are H_2O and CO. The Van Der Waal radii are 1.75 and 1.859 Å, respectively. Further, the surface needed to be updated to reflect these changes. The surface is constructed of two layers of atoms fixed in a body-centered cubic arrangement, which do not move during the simulation. The atoms have a size approximately that of a carbon atom at 1.6 Å. The size and potential for the surface may be tuned to accommodate other surface types but for our purposes the identity is not of great significance as long as sticking occurs at the desired temperatures.

Table 2.2: Van der Waal radii used for each species in the presented models. The grain radius is nominally based on the size of a carbon atom.

Grain	H_2O	CO
1.6	1.75	1.859

2.2.4 Extended Reaction Network

The initial goal to extend the reaction network was to accommodate the formation of glycine. A collaboration for a paper in prep. led to the need for such an extended network. This work will not be presented in this body of work as it beyond the scope of the subject at hand. The network was applied to formation of ices with interstellar conditions with the select goal of finding the compactness in this regime. Before the initial changes MIMICK consisted of a simplified network with 73 reaction consisting of 39 different species. The reaction network has been upgraded to contain 330 reactions and 130 species. The purpose of this update was to include all important reactions that might occur with atomic abundances similar to those of a dark cloud. The primary formation route expected from laboratory experiments is through the reaction between CH2NH2 and COOH. All reactions leading to the formation and destruction of these products was added. Alternative routes to glycine were included as was reactions that destroy the precursors.

Part II:

Body of Work

3

Amorphous Water Structure

Contents

3.1 Water Structure: Density Study

Laboratory ice experiments are one means to gain an understanding of the physical structure and chemistry that can occur in astronomically-relevant ices (for further discussion on ASW formation, characteristics, and processes, see Hama and Watanabe 2008. [43]) However, it is yet unclear whether the ices that are grown under laboratory conditions are closely representative of interstellar ices. Various conditions must be considered when

forming an interstellar ice analog in the laboratory, such as the deposition rate, vacuum pressure, temperature, deposition angle, and thickness of the deposited ice. All of these parameters can alter the ice morphology, and may play a significant role in interstellar ice structure. Typical laboratory experiments involve a high- or ultra-high vacuum system (UHV), i.e. 10^{-7} to 10^{-11} torr, with temperatures usually ranging from $\sim$10 to 300 K. The typical gas density corresponding to a UHV system is $\sim 10^7$ molecules cm^{-3} – higher than the values that obtain in dense interstellar clouds, which range from around 10^6 down to 10^4 molecules cm^{-3}. Furthermore, the production of water ice under interstellar conditions typically occurs through the deposition of atomic precursors, which then form water through chemical reactions (although in certain types of interstellar object, such as protoplanetary disks, direct water deposition may indeed dominate). Due to the different gas densities and formation mechanisms operating in typical laboratory and interstellar regimes, to reach equivalent coverages or thicknesses in either case requires vastly different timescales (minutes versus many thousands of years).

The formation of laboratory water ices has been treated computationally using a number of simulation methods, such as ballistic, molecular dynamics, and kinetic Monte Carlo models.[62, 61, 56, 30, 16] Kimmel *et al.* (2001a) utilized a simple ballistic model where deposition angle was considered. Temperature was not explicitly treated, but the incoming particle was allowed to hop a fixed number of times before the next particle was deposited. [57] Treating the temperature and diffusion appears to be important for correctly characterizing structure. Another condition that should be considered is the kinetic energy of each incoming particle, because it may be converted to translation energy. This relaxation process has been modeled extensively by Yang *et al.* (2001) and Zhou *et al.* (1997) for high-energy collisions (1 to 20 eV) for thin nickel films deposited from ionized vapor. [93, 95] In the case of laboratory ice experiments, as well as under interstellar conditions of interest, typical energies will be much lower (well under 1 eV). However, the adsorption of a water molecule into a local surface potential minimum will imbue that particle with some further kinetic energy as it is accelerated toward the surface at short range. This combined kinetic energy may allow the newly-adsorbed particle to undergo one or more surface diffusion events before thermalizing with the surface. Such occurrences have not yet been considered in kinetic simulations of water-ice production. Some recent work has investigated non-thermal hopping, but the source of energy was the exothermicity of reactions.[62, 61] The work described here investigates non-thermal hopping activated by the energy gained from deposition.

Here we investigate the formation of porous structures within ices formed in a laboratory setting and seek to reproduce the trends in porosity associated with the main experimental parameters during the ice-formation process. We modify the interstellar off-lattice kinetic Monte Carlo model *MIMICK*[40], a version of which was first presented by Garrod (2013), to allow application to laboratory conditions; here, periodic boundary conditions are applied, allow a small section of laboratory ice to be modeled self-consistently. The use of this off-lattice model allows a fully three-dimensional picture of amorphous ice structure to be traced, as it is formed kinetically through deposition and diffusion, and allows the conditions used in published experimental studies to be replicated. The tuning of model parameters, achieved through the successful reproduction of experimental results, allows ice production under the more extreme conditions of the interstellar medium – currently inaccessible in the laboratory – to be explored through simulations, and the fidelity of interstellar ice analogs to real interstellar ices to be assessed. The full exploitation of experimental ice data to improve our understanding

of interstellar ice formation makes kinetics models like the one presented here essential.

Monte Carlo chemical kinetics models by Garrod (2013)[40] and a laboratory study by Oba *et al.* (2009) [65] found direct deposition should produce much greater porosity than the chemical formation of water ice. In the models, diffusion of oxygen atoms at 10 K, prior to their hydrogenation to water by atomic H, allowed microporous structures to be filled in more effectively over long interstellar timescales, whereas the water molecules directly accreted from the gas phase were essentially immobile, and therefore formed highly-porous structures. A prevalence of porous structures within interstellar ices will also significantly increase the time required for any arbitrary diffusing particle to visit all surface binding sites, increasing the meeting and reaction timescales in cases where only a few reactants are present on the surface at any moment.

We first discuss the computing requirements of the model. We then present results from preliminary models that allow the tuning of the model parameters, using experimental data in the regime where there is little/no temperature dependence for measured ice densities. We then present the results of this model as applied to fixed-angle deposition, and then to background-deposited ices at various temperatures.

With this model, we examine how amorphous H_2O ice structure is affected by various deposition parameters, including the ice temperature, the rate of deposition, and the angle at which the incoming gas molecules approach the surface. Past computational studies have varied the deposition rate, matching the rates used in laboratory experiments, with the sole intention of replicating laboratory results and have not been extended to replicate the ISM. The presented work is the first application of a model to the direct comparison of laboratory and interstellar ices, using respective deposition parameters.

The main feature of the experimental ices that we aim to reproduce is the porosity. The advantage of using *MIMICK* is that the positions of all particles are known at all times, so that porosity may be explicitly traced, and can be directly observed using three-dimensional representations of the simulated ice. The degree of porosity produced in the models can be quantified in various ways, but only methods that can be compared directly with laboratory values are useful in constraining the model parameters. We therefore use the ice density as a proxy for porosity and the structure, as is done by various experimental groups. The densities of simulated ices are relatively simple to calculate (see Section 2.2).

We use an off-lattice microscopic kinetic Monte Carlo model called *MIMICK* to simulate laboratory deposition of amorphous water ice. With this model, we examine how amorphous H_2O ice structure is affected by various deposition parameters, including the ice temperature, the rate of deposition, and the angle at which the incoming gas molecules approach the surface. Past computational studies have varied the deposition rate, matching the rates used in laboratory experiments, with the sole intention of replicating laboratory results and have not been extended to replicate the ISM. The presented work is the first application of a model to the direct comparison of laboratory and interstellar ices, using respective deposition parameters.

The main feature of the experimental ices that we aim to reproduce is the porosity. The advantage of using *MIMICK* is that the positions of all particles are known at all times, so that porosity may be explicitly traced, and can be directly observed using three-dimensional representations of the simulated ice. The degree of porosity produced in the models can be quantified in various ways, but only methods that can be compared directly with laboratory values are useful in constraining the model parameters. We therefore use the ice density as a proxy for porosity and the structure, as is done by

various experimental groups. The densities of simulated ices are relatively simple to calculate (see Section 3.1.2).

3.1.1 Deposition Parameters

Experimental ice thicknesses are typically defined by the number of monolayers (ML). In these models, we define a monolayer as a single sheet of molecules (without pores), that will fit precisely on top of the bare substrate. Hence, simulations with substrate surface sizes of 80×80 and 160×160 have 160,000 and 640,000 molecules, respectively, for a 25 ML thick water ice. Typical dense cloud ices are ∼100 ML in thickness, on the order of tens of nanometers. Experimentally, ices have been studied in the range from tens of nm to μm thick. However, ices of thicknesses around 1–5 μm can be prone to spontaneous cracking, accompanied by the production of very large pockets that are phenomenologically different from the porosity that we aim to model here. Furthermore, *MIMICK* accepts only a uniform temperature value throughout the ice, and therefore does not take into account any variation in temperature associated with distance from the cooled surface, which may be important for thicker ices. [12, 90, 7, 57, 29] Since results for thinner ices are also available in the literature, experiments closest to astronomical thicknesses will be used for comparison with the simulations.

Preliminary models indicate that surface sizes significantly lower than our smallest surface size of 80×80 substrate atoms (e.g. 10×10), produce surface and bulk-ice structures that are comparable in scale to the size of the periodically-repeated cell in which they form, raising the possibility that, in such a regime, the cell size itself may control the size of the simulated structures. Similar effects can also become apparent where ices are allowed to form that are significant thicker (taller) than the substrate is wide. To avoid such effects, we use at least an 80×80 ice, using the 160×160 ice where model run-times allow. The choice of using 25 ML as our standard thickness avoids this problem in the vertical direction. Surface effects and computational time are discussed further in section 3.1.3.

It should be noted that the experimental data sets that we compare our results with most frequently in this work, which come from Brown *et al.* (1996)[12] and Berland (1995)[7], were obtained for ices ranging from ∼700 ML to 5 ML, respectively, with densities measured in each dataset that are reasonably consistent with each other, showing no significant divergence. However, the Berland *et al.* data, while closer in ice thickness to the 25 ML ices that we simulate, cover only a few temperature values, while the Brown data are well-sampled from 15–125 K. The Berland *et al.* ices may also be thin enough that the ice structures formed local to the substrate surface could influence the density values, possibly diverging from the values obtained in the bulk water ice. For these reasons, we mostly constrain our comparisons to the Brown *et al.* (1996) data. [12]

In the models presented here, ices are deposited onto the surface at temperatures ranging from 10 to 130 K. Deposition rates are varied from 10^1 to 10^{16} molecules cm^{-2} s^{-1} (equivalent to the number of molecules delivered to the surface at 10^{-20} to 10^{-5} Torr). Additionally, a deposition rate of 10^6 molecules cm^{-2} s^{-1} was used to replicate conditions pertaining to protoplanetary disks.

Two different deposition methods are used to reproduce experimental treatments: 1) deposition angles are randomly generated individually for all molecules, to replicate ex-

perimental background deposition, and 2) incoming particles are all deposited at the same angle with respect to the surface (ranging from 0° to 75°). A number of ice thicknesses were investigated (10 ML to 100 ML).

3.1.2 Calculating density

The method used to calculate the density of the ices produced by the models must take into account the effect of porosity; it must therefore be an average over the entire bulk ice, rather than be based on small sections, whose densities may vary widely at a local level. Since the number of water molecules is known, the calculation of density reduces to a calculation of the volume of the ice produced. To calculate this volume, we divide the ice into vertical columns, each of base size $\sigma \times \sigma$, and measure the height of the highest water molecule within it, to determine a volume. We then sum these volumes, and divide the total mass of water molecules by this value. Densities are reported in g cm^{-3}.

3.1.3 Computational Considerations

The *MIMICK* model runs in a single thread for each model setup; the advantages of parallelization were thought to be limited at the time of publishing for this type of model, due to the sequential nature of the calculations. The code was, however, optimized by storing previously-calculated particle positions, in the case where uninterrupted chains of surface hops occur for individual molecules; diffusing particles often return to the same sites multiple times. This chain information is saved even if the chain is broken by multiple particles taking turns to move on the surface, so long as they do not physically interact. This approach is essential to allow the code to be run on manageable timescales, but necessarily demands significant RAM allocation (averaging around 1–2 kB per particle in the model). However, in all the models presented here, the required RAM allocation is easily handled, and the main limitation on the size of model parameters is the run-time.

The bulk of the calculations carried out in the code relate to thermal hopping between binding sites. Therefore, the main factors that influence the CPU time of the model are the number of molecules being deposited (dependent on surface size and coverage), the rate at which the ice is deposited, the surface temperature, and whether the relaxation treatment is implemented. Higher dust temperatures and lower deposition rates will raise the time required for each run, due to the larger number of hops occurring prior to model completion. The relaxation process adds extra hops for each deposition event. The time required to run a model ranges from as little as 10 minutes (for a model at 10 K with a deposition rate of 10^{13}, an 80×80 surface with maximum ice coverage of 25 ML, and no relaxation calculations) to around a week for high surface temperatures combined with the largest surface or low deposition rates. Given the dependence of the computational time on the number of molecules, we use the smallest surface size possible (for a given target ice thickness), while maintaining a large enough surface to prevent surface inhomogeneities from dominating the density value, and to avoid pore-scale issues.

3.1.4 Tuning of Pairwise Interactions

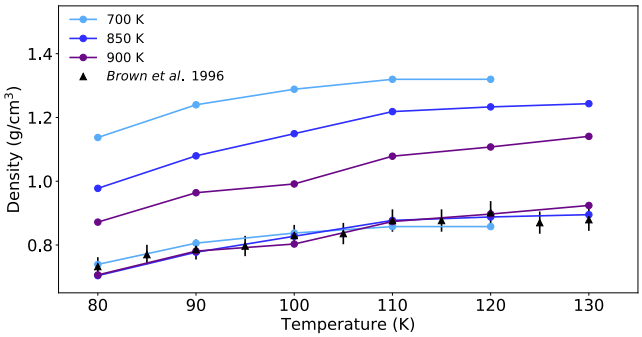

Figure 3.1: Densities of ices produced using pairwise interactions of 700, 850, and 900K. Re-scaled densities are also shown, using scaling factors for each model determined by best-fit calculations to the experimental data of Brown *et. al* (1996). [12]

A major influence on the simulated ice density is the strength of binding (ϵ) between each water molecule and its neighbors, which controls both the total binding energy of each molecule and its diffusion barriers. The general approach in the *MIMICK* model is to use non-directional potentials for all atoms and molecules, which in interstellar applications could include on the order of 100 species. In the models presented here, we require only two pairwise potentials: the surface–H_2O interaction and the H_2O–H_2O interaction. The stronger the interaction, the higher the temperature must be to overcome the resultant diffusion barriers. When the value is low, the molecules have weaker local diffusion barriers, allowing them to diffuse more easily to find a deeper potential well, which produces a generally smoother ice. Conversely, with high values (assuming the same ice temperature), the strength of the H_2O–H_2O interaction can significantly slow – or even prohibit – diffusion, resulting in more irregular structures on large and small scales.

In order to achieve the appropriate water density for comparison with experimental values over a broad range of temperatures, we first tune the model to reproduce certain key values. The experimentally-determined densities of Brown *et. al* (1996)[12] are plotted (along with test-model data) in Figure 3.1, over the 80–130 K range; the full dataset extends down to 20 K. It may be seen that at temperatures around 110 K and higher, the experimental density values reach a plateau at around 0.87–0.90 g cm^{-3}. We therefore assume, for the purposes of our parameter fitting, that thermal diffusion is efficient enough in this range of temperatures to produce the maximum surface rearrangement possible, thus achieving the densest structure available for low-density amorphous water. At lower temperatures, the thermal diffusion of water molecules is less able to rearrange the surface to reach this maximum density.

To find the best set of ϵ and σ parameters for our models, we therefore seek firstly a water-water pairwise potential that produces ice densities that achieve plateau behavior beginning at around 110 K (regardless of the absolute value of the density achieved in the model). Figure 3.1 shows the results from several models in the ϵ=700–900 K range that achieve similar plateau behavior in the correct temperature range. A range of models was in fact run between 700–1200 K, for temperatures ranging from 80–130 K, in 10 K increments, with water deposited at random angles at a rate of 10^{13} molecules cm^{-2}

s^{-1}. High pairwise potential models tend to produce plateau behavior only at very high temperatures; lower potentials reach a plateau at lower temperatures.

We take the density results from these models and scale them with a uniform scaling factor, determined uniquely for each model (and representing divergence from the initial σ value of 3.2 Å). This factor is in each case calculated by minimizing the chi-squared function shown below to achieve the best match with the experimental data for each model.

$$\chi^2 = \sum_{i=1}^{n} \frac{(O_i - E_i)^2}{E_i} \tag{3.1}$$

We use the formulation in Eq. (3.1) (typically used in Pearson's Chi-squared test) as a means to measure the goodness of fit. Index i indicates the temperature of interest, O_i is the observed density at a particular temperature and E_i is the corresponding density measured from Brown *et al.* 1996.[12] The fitting uses the data in the 80–130 K range, corresponding not only to the plateau region, but also to somewhat lower temperatures, at which it is assumed that the density is still determined by purely thermal diffusion of water molecules (as is borne out by later models). The final best-fit values of chi-squared (per Eq. 6) determine not only the best-fit scaling factor for each model, but also the best-fit model out of all of those tested, across all values of ϵ. The best-fit values are listed in Table 3.1, while the unscaled and scaled density values are plotted over the experimental values in Figure 3.1. Although the ϵ=1200 K model shows moderately good agreement, with no scaling factor required, no plateau-like behavior is in fact observed in those models; densities continue to grow for increasing temperatures. The model with $\epsilon(H_2O–H_2O)$=900 K did not achieve the plateau at the highest temperature desired. The overall best match to the experimental data was initially found to correspond to a value $\epsilon(H_2O–H_2O)$=800 K. An additional model was run using ϵ=850 K, using a scaling factor of 0.735, which provided an even better match. We adopt the ϵ=850 K value for all other models presented here. Based on the required density-scaling factor for this model to match observations, we tune the value of the (one-dimensional) σ parameter from the initial value of 3.2 Å, to a value σ=3.546 Å., so that the model results match the experimental values without a density-scaling factor.

Table 3.1: Best-fit density-scaling factors and associated values of the goodness-of-fit parameter (chi-squared) for models using various values of the pairwise interaction for H_2O-H_2O. The asterisk denotes the overall best-fitting pairwise potential, which was chosen for use in all subsequent models

H_2O-H_2O (K)	Scaling Factor	χ^2
700	0.65	0.0034
800	0.71	0.0023
850*	0.73	0.0016
900	0.80	0.0041
1000	0.79	0.016
1100	0.97	0.0068
1200	1.00	0.0033

The adopted pairwise potential of 850 K results in an average total binding energy for surface molecules of ∼6,700 K, based on the calculated averages at the end of the model runs at low temperatures. The values increase up to ∼7,300 K for surface temperatures of 130 K. These values fall toward the upper end of typical ranges of binding

energies for water in astrochemical models. However, binding energies for *individual* water molecules in the present *MIMICK* models can range to as low as ∼3,000 K, making such molecules more likely to desorb. Since desorption of an individual molecule is likely to be preceded by multiple diffusion processes, the *effective* desorption energy may be lower than the average values quoted above, due to molecules finding and then preferentially desorbing from weak binding sites. To determine this *effective* binding energy, a full TPD model would need to be run. The value of 4,800 K determined by Penteado et al. (2017)[70] indeed falls between our lower value of 3000 K and the mean value of 6,700 K for low-temperature deposition. A full analysis of TPD desorption characteristics will be discussed in chapter 6 of this work.

3.1.5 Uniform Incident Angle

In order to test the effects of ice deposition at fixed incident angles, a number of ice simulations were run, using various angles of deposition, over a range of temperatures and deposition rates. Figure 3.2 shows a side view of each of the resultant ices produced for deposition rates 10^1 and 10^{13} molecules cm^{-2} s^{-1}, at temperatures of 10 and 30 K, with angles varied from 0 to 75°. The images are produced using the freeware ray-tracing software, *POV-ray*. While water is treated in *MIMICK* as a sphere, using non-directional potentials, it is nevertheless depicted in these images as a molecule, following the treatment by Garrod (2013)[40], who chose this representation to aid identification of different species. The porous structure of the ices is clearly visible, demonstrating the effect of shadowing; voids are present between the column-like structures of H_2O, especially for large angles of incidence. Ices deposited normal to the surface show gaps still present, but they appear smaller and less tubular than for high angles. Similar structures can be seen in Kimmel *et al.* (2001)[57] and Dohnalek *et al.* (2003)[30] where a ballistic model was used. Their model, while demonstrating angular dependence, did not investigate the effect of deposition temperature. An arbitrary number of hops or diffusion events were allowed to occur for each molecule, but the structure does not reflect the surface temperature. This is a critical component when considering an ice that may warm up and experience structural changes.

These general trends in structure that are visible in Figure 3.2 are also reflected in the density behavior. Figure 3.3 plots the simulated ice density against temperature for several incident angles (shown in blue), for temperatures ranging from 10 to 115 K; only the high deposition rate results are shown. Background deposition (i.e. random angle deposition), discussed in more detail later, is shown in green, and exhibits behavior comparable to that of ices grown at a 60° angle. Higher temperatures during deposition produce higher densities, although at high deposition rates, little variation is observed below temperatures of 35 K. Each of the deposition angles shown produce density variations of a factor of ∼2, over the 10–115 K temperature range.

Increased temperatures allow more loosely-bound water molecules to diffuse into nearby potential minima that provide stronger binding. The stronger sites will tend to be those with pronounced inward surface curvature at a microscopic level, as these will allow a water molecule to interact with more H_2O neighbors. This effect may be seen visually in Figure 3.2, for the low deposition-rate ices; higher temperatures produce smoother ices, indicating that microscopic-scale roughness is being smoothed away, while

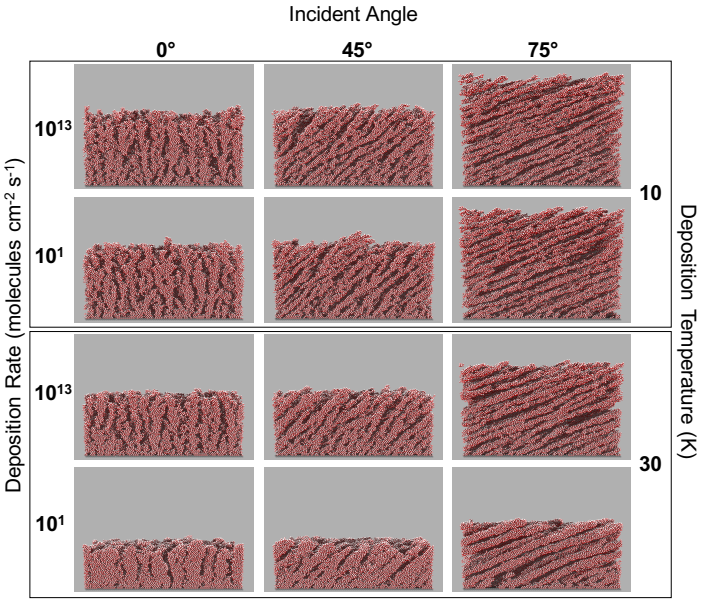

Figure 3.2: Simulated ices, shown in side-view, produced for deposition angles ranging from 0° to 75°. Results for two temperatures are shown (10 K and 30 K), divided into high and low deposition rates (10^1 and 10^{13} molecules cm^{-2} s^{-1}). Columns of ice with interstitial voids are formed, whose angle traces the deposition angle. Greater porosity is produced for ices formed at lower temperature, higher deposition rate, and greater angle. Images were generated using the ray-tracing software, *POV-Ray*.

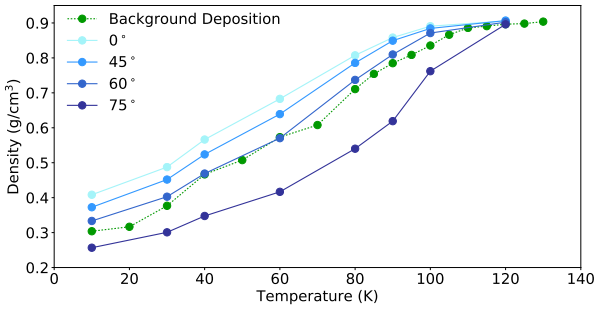

Figure 3.3: Simulated ice densities as a function of temperature for ices deposited at a rate of 10^{13} molecules cm^{-2} s^{-1}. Ices grown at incident angles ranging from 0° to 75° are marked in blue; the results for background deposition are also plotted. The ice densities for background deposition are comparable to those deposited at a fixed angle of ∼60°.

some larger-scale structures still remain.

The same structural trend seen in Figure 3.3 was found by Stevenson *et al.* (1999) who measure porosity by N_2 adsorption to water ices formed with various deposition angles. They found that N_2 adsorption was greatest at low temperatures and angles, with the exception of a normal incident angle, for which a consistently low degree of porosity, with no temperature dependence, was observed.[83] This particular result therefore disagrees with our simulation results, which show a clear temperature–density dependence for all angles. Unfortunately, it is difficult to compare directly the experimental N_2 adsorption results with the simulated densities, as there is no means of direct conversion immediately apparent. It is possible that the degree of adsorption may also incorporate some measure

of the connectivity of pores within the ices. The more irregular shapes of the pores produced by the simulations at normal angles are arguably consistent with a picture in which the efficient uptake of gas-phase N_2 would be limited only to those pores closest to the outer surface. In this scenario, the pores throughout the ice would become isolated from each other, either during their formation, or as a result of blockage of any narrow connective passages by the adsorption of the N_2 itself. It is unclear without more detailed modeling whether the latter effect might be possible for the ices shown in Figure 3.2. The direct simulation of experimental adsorption of N_2 on porous ices is a topic for future study.

3.1.6 Background Deposition

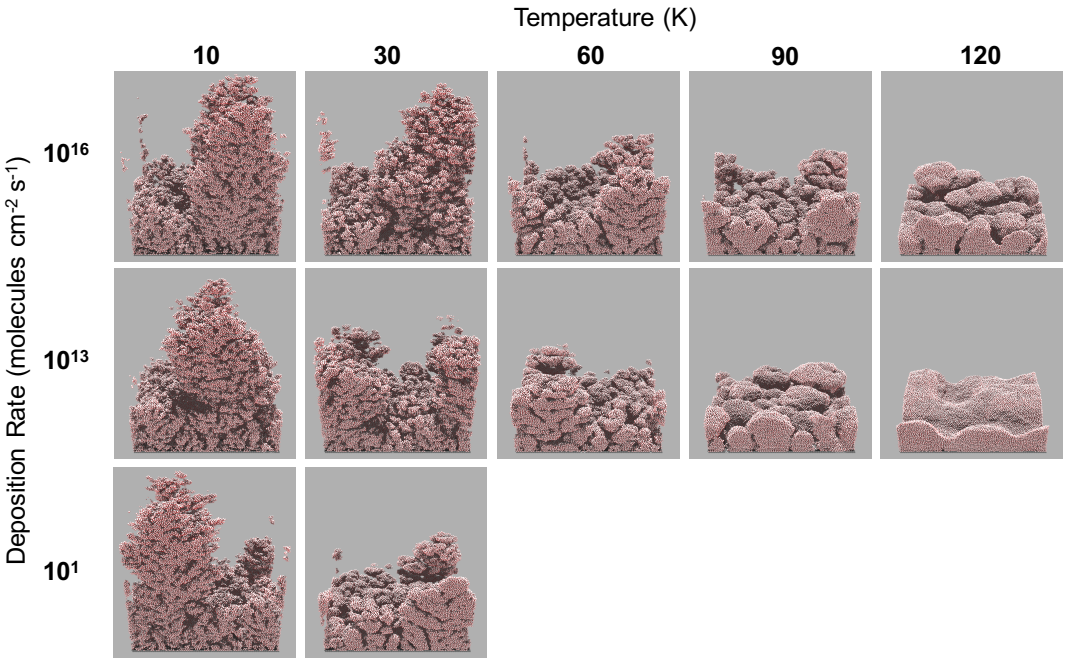

Figure 3.4: Simulated ices formed through background deposition at various rates, for a range of surface temperatures with immediate relaxation. Molecules deposited at the lowest rate are unable to form an ice at high temperature. Additional images are shown for temperatures 15 and 25 K for this deposition rate. The ice grown at 35 K at this rate has a density of 0.786 g cm^{-3}, similar to the ice grown under laboratory conditions at 85 K. Ice densities are greatest for higher temperatures and lower deposition rates.

Direct determinations of the densities of amorphous ices produced through background deposition are available in the literature. It is therefore valuable to attempt to reproduce these experiments using *MIMICK*, as we may compare both the density trends and the absolute values, in order to constrain the models and to shed light on the processes occurring as the ices are formed.

Background deposition was simulated for a range of deposition rates (10^1, 10^6, 10^{13}, and 10^{16} molecules cm^{-2} s^{-1}) and temperatures (10–120 K). The images and results are shown for ices with a thickness of 25 ML. Figure 3.4 shows side-views of a selection of the resulting simulated ices. Sticking was not achieved for models with a deposition rate of 10^1

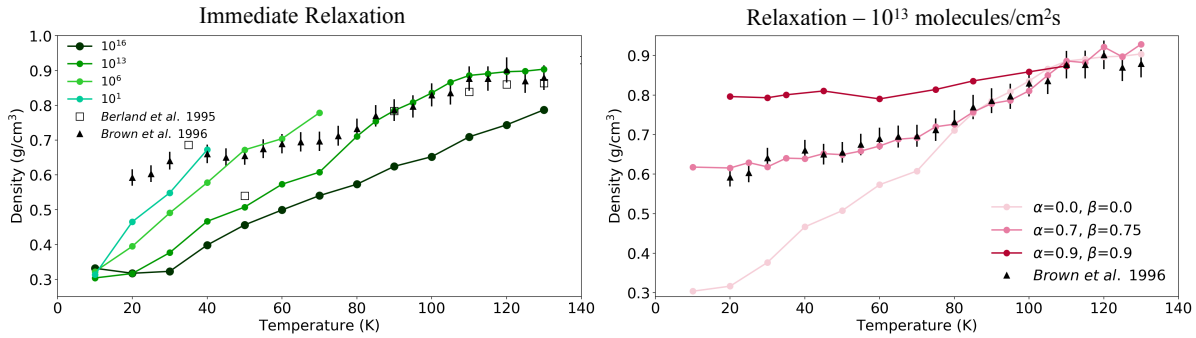

Figure 3.5: Densities of amorphous water ices grown at various temperatures and deposition rates using randomly-generated angles for each molecule. The gradient shows an increasing α and β for a deposition rate of 10^{13} molecules cm^{-2} s^{-1} comparable to the laboratory data of Brown *et al.* (1996), shown in black.[12]

molecules cm^{-2} s^{-1} at temperatures above 40 K. The angle of incidence for each incoming particle is randomly generated, mimicking the likely behavior of both experimental and interstellar ice deposition.

The total fluence of deposited water molecules is held constant between simulations, so the number of molecules is approximately the same for each case and for each image shown in the figure. The ices may be seen to become significantly more compact as temperatures increase from 10–120 K. Large-scale irregular structures or protrusions are less frequent at higher temperatures, and less small-scale porosity is apparent; the porous structures are also more regular and somewhat wider, consistent with more effective thermal diffusion. Decreasing the deposition rate for simulations at sufficiently high temperature also produces more compact ices; however, at lower temperatures, diffusion is slow, and there is little difference in the compactness produced for the different deposition rates.

The densities calculated for all the simulated ices are plotted in the left panel of Figure 3.5, shown as colored lines. Experimental data from Brown *et al.* (black triangles) [12] and Berland *et al.* (black squares) [7] are also shown. Dohnalek et al. (2003) shows the same trend from the Brown data but is not shown here for clarity. [29] A rate of 10^{13} molecules cm^{-2} s^{-1} in the model is the most comparable to the laboratory experiments of Brown *et al.* (1996) with estimated rates between 10^{13}-10^{14} molecules cm^{-2} s^{-1}.

The figure demonstrates more clearly the increase in density with surface temperature. The ices become smoother and thinner at higher temperatures, while increasing the deposition rate has the opposite effect. This effect has been reported by Berland *et al.* (1995), who showed using refractive index measurements that increasing the deposition rate causes the density of ASW ices to decrease. If the deposition rate is much faster than the rate of diffusion, the molecules do not have time to rearrange into lower energy sites before another molecule is deposited nearby, locking the structure more firmly in place. At higher temperatures, the model results are in good agreement with the experimental data, at the appropriate deposition rate of 10^{13} molecules cm^{-2} s^{-1}; both the general trend and the absolute density values are well reproduced.

In the low-temperature models, diffusion essentially does not occur rapidly enough to compete with deposition, and all deposition rates of a magnitude achievable in the laboratory (i.e. the two higher values) produce ices with the same low density. This marks a clear divergence from the experimental results. In the lowest deposition-rate

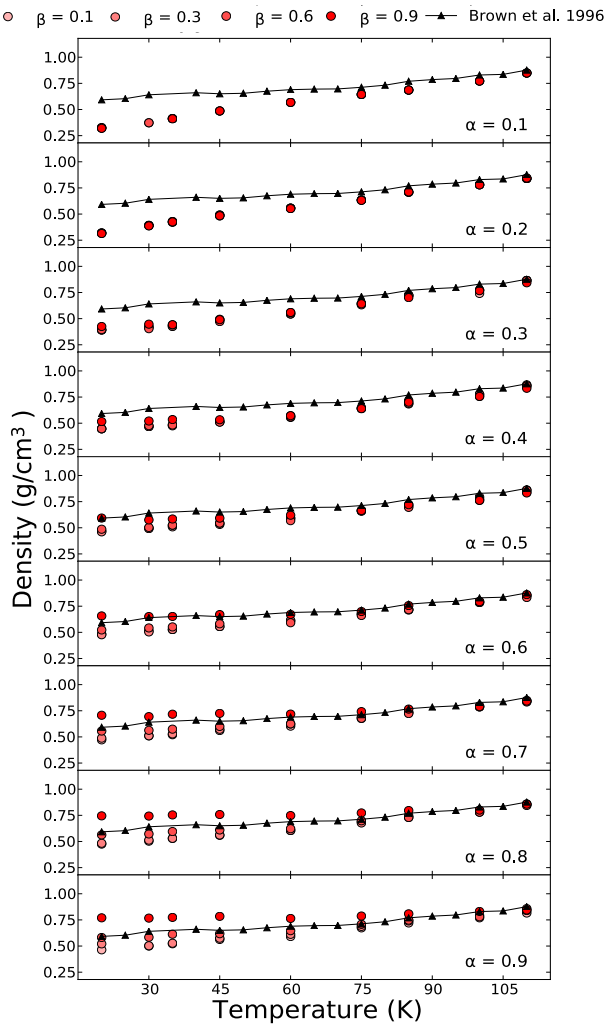

Figure 3.6: Modeled ice densities as a function of temperature, for various values of the α and β parameters. Each box is a different α value from 0.1 to 0.9. The colors are β values from 0.1 to 0.9. The Brown *et al.* (1996) data is shown in black for comparison.[12]

case, appropriate to interstellar conditions, densities more comparable with the high deposition-rate experimental values can be obtained, indicating that thermal diffusion has time to re-arrange the surface structure before it becomes locked in.

These simulations therefore suggest that where thermal diffusion is sufficiently active, the modeled ices are a good representation of experimental densities and/or structures, over a range of temperatures. The break-down in fidelity suggests that at low temperatures, a non-thermal process may take over that was not included in the basic version of *MIMICK* that has been employed up to this point.

3.1.7 Relaxation Process

Here we include the relaxation process described in Section 2.2.1, whereby the sum of (i) the residual gas-phase kinetic energy of the incoming water molecule, and (ii) the energy it gains as it is accelerated into a surface potential well, is made accessible to the adsorbed

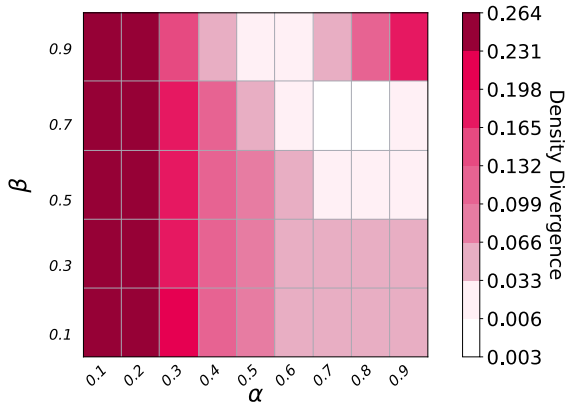

Figure 3.7: Divergence of the simulation results from the experimental densities of Brown *et al.* (1996)[12], as a function of the relaxation parameters α and β. The divergence from experimental results is quantified as a chi-squared value.
Smaller divergence is indicated by lighter colors.

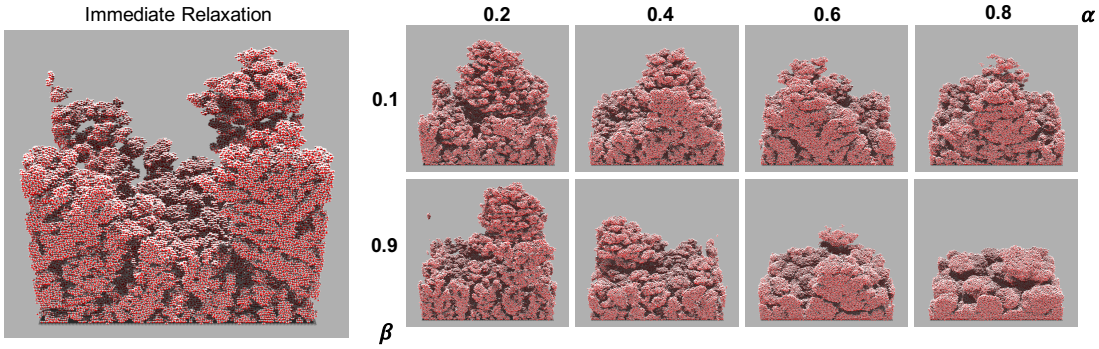

Figure 3.8: Images of ices deposited using various α and β values at 30 K. The deposition rate was maintained at 10^{13} molecules cm^{-2} s^{-1}. The density increases as both α and β are increased.

molecule to overcome diffusion barriers. It may continue to hop over barriers to diffusion until insufficient excess energy remains, by which point it has relaxed, becoming fully thermalized with the surface. The models presented in section 3.1.6 may be considered to assume an immediate thermalization of all deposited molecules.

The relaxation process has two parameters associated with it that can be thought of as efficiencies, α and β, corresponding respectively to the fraction of energy retained upon the initial deposition, and the fraction retained after settling into a new potential well as a result of diffusion. While all of the energies considered in these calculations are determined locally, according to the nature of the molecular constituents of the surface and their relative positions, the efficiencies α and β are held constant for all molecules, throughout each ice deposition simulation.

Values for both α and β ranging from 0.1 to 0.9 were tested in the models; the smaller 80×80 surface was used for consistency throughout the model grid, due to the longer run-times required for the most extreme α, β values, which scale roughly with surface size. The resulting densities for some of the simulations are compared with the laboratory data of Brown *et al.* (1996)[12] in the right panel of Figure 3.5. It may be seen from the figure that higher-end α-values ($\sim$0.7–0.8) produce a very good match to the experimental results. Variations in α have a strong effect on the overall agreement;

the most extreme model we tested ($\alpha = 0.9$, $\beta = 0.9$) is dominated by the non-thermal diffusion produced by the gradual relaxation of the molecule on the surface, showing no significant temperature dependence at all. The corresponding results from Section 3.1.5 ($\alpha = 0$, $\beta = 0$) are also shown on this plot.

Figure 3.6 shows the temperature dependence for each model in the grid, with each panel corresponding to a different α-value. Datasets for the various β-values employed are indicated by the color of the dots. Data from Brown *et al.* (1996) are marked in black as before.[12] It is again apparent that the α=0.7, 0.8, 0.9 values provide the closest match to the experimental data, although the α=0.8 dataset shows the best match over all possible β-values.

To determine the best match more precisely, a χ^2 test was applied to the densities obtained with the various temperature runs for each model setup. Figure 3.7 shows a map of the χ^2 values with the corresponding α,β pairs.

A number of models were very close in error. An α-value of 0.7 or 0.8 was the best fit; β-values of 0.7 were the best fit for α=0.7. A β-value of 0.7 was the best for α=0.8. Based on these outcomes, several extra models were run in intervals of 0.05 for α and β. The resulting best fit was α=0.7, β=0.75. The χ^2 error was a quarter of the error associated with the α = 0.7, 0.8 and β= 0.7 models. For the remainder of the study, the [0.7, 0.75] values are selected as the best match.

Images of the ices employing our relaxation treatment are shown in Figure 3.8; the ice produced by a model with immediate relaxation, i.e. α=0 and β=0, is shown on the left. Increasing α produces a significant smoothing on small scales, removing porosity, as well as an increase in uniformity on large scales, such that the ices appear flatter. The β-values shown are the most extreme; this parameter has a relatively strong effect on structure when α is adequately high. The reason for this is more apparent in Figure 3.10, which shows the efficiency and distribution of hops for a range of α and β values at 30 K. For an α-value of 0.7, all β-values are mostly dominated by single-hop events, until extreme β values; at lower α values, essentially all particles hop once. Starting at intermediate β values, the number of hops switches from 1 hop to a distribution of hops. At extreme β values 4 to 5 hops are dominating the structure. A broadly similar outcome is found for larger α-values, except in the case of α=0.9, with high β; here, for β=0.6, the two-hop outcome is as probable as a single-hop event, while for β=0.9 the most probable outcome is four consecutive hops. In this case, four *or more* hops will occur with a probability close to 50%.

For individual α,β pairings, the probabilities for different numbers of hops per deposition event are quite stable over the entire temperature range tested. The results presented in Figure 3.9 are therefore a good representation for all temperatures.

It should be noted that for α=0.7 and β=0.75 the probability of one hop is greater than ∼25%, and for two hops ∼51%. While it is likely that the particle hopping twice can move back to its initial position, this only occurs in about 17% of cases. When β is large, more hops for a single particle are able to occur, because less energy is lost every hop. The number of particles and hops is also affected by the surface temperature (not shown), because diffusion may also occur thermally, which allows the molecules to find and occupy stronger sites, smoothing the ice and reducing the fraction of strongly-binding sites available. This reduces the energy required to hop, making multiple non-thermal hops more likely.

Figure 3.9 shows the structure of model ices produced at several temperatures, using the best-fit α and β values. The structure of the ice clearly changes between each tem-

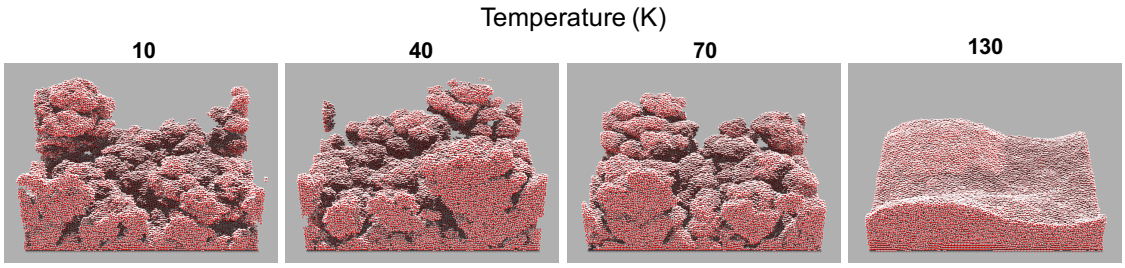

Figure 3.9: Stimulated ices, shown in side-view, with the best fit α and β values of 0.7 and 0.75, respectively. The temperatures are varied from 10 to 130 K with a constant deposition rate of 10^{13} molecules cm^{-2} s^{-1}.

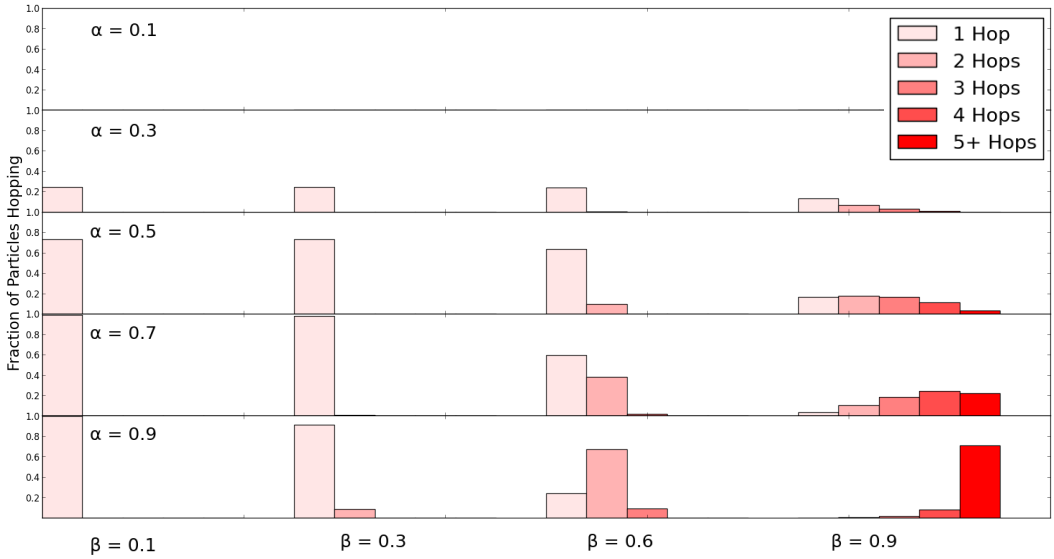

Figure 3.10: Probabilities of varying numbers of consecutive hops, obtained from the simulations for different α and β values at 35 K. The bar colors correspond to number of hops carried out in succession.

perature shown. At 10 K the ice has its highest level of porosity. As the temperature is increased, from left to right, the structure becomes increasingly smooth and the pores gradually disappear. At high temperature (130 K), the structure is completely smooth with no porosity.

3.1.8 Interstellar and Protoplanetary Disk Conditions

The simulations presented here allow water ices to form through direct deposition of water molecules; however, in many regimes in the interstellar medium, including dark clouds, ices are expected to form through surface chemical processes. One regime in which direct deposition of water molecules onto dust grains is a plausible formation process is within protoplanetary disks, where water may be repetitively desorbed and re-deposited, due to variable dynamical and physical conditions. [39, 3] The simulations so far have included model runs using deposition rates of 10^{1} molecules cm^{-2} s^{-1} (similar to that suggested by Cuppen and Herbst, 2007), which are appropriate for a typical dark cloud with a density

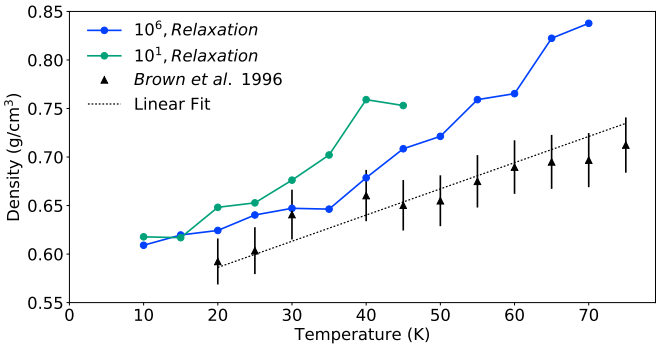

Figure 3.11: Densities of deposition rates corresponding to a protoplanetary disk (blue) and a dark cloud (green). Laboratory data from Brown *et al.* (1996) are shown in closed squares with corresponding error.

of 10^4 cm^{-3}.[25] Densities in protoplanetary disks, however, may be significantly higher. To test the effects on a water ice formed through direct deposition in this regime, models were run with a deposition rate of 10^6 molecules cm^{-2} s^{-1}, which corresponds to a gas density of $\sim 10^9$ cm^{-3}.

The results of these simulations for various temperatures are plotted in Figure 3.11, with data from Brown *et al.* 1996 for comparison. We use the best-fit values, α=0.7 and β=0.75 for the relaxation parameters. The dark cloud and the protoplanetary disk rates are shown in green and blue, respectively. When considering the relaxation process, the deposition rate relating to a dark cloud yields ice densities higher than the experimental values, indicating lower porosities. The porosity could be considerably lower, however, if the ice is formed through surface reactions. There is reasonable agreement between the protoplanetary disk conditions and the experimental data in a temperature range of ∼30–40 K, so laboratory data may be directly applicable to regions in disks that are within that temperature range. For other temperature values, and for the dark-cloud regime in general, porosities produced in experimental studies are unlikely to be a close match to interstellar ice structures, if formed through direct deposition. Closer correspondence may be obtained by producing laboratory ices at somewhat higher temperatures than interstellar conditions would suggest.

To this end, we provide in Table 2 a list of density values for interstellar and protoplanetary conditions, calculated at specified model temperatures, accompanied by the temperatures at which those same densities could be achieved under laboratory conditions. The temperatures were found by using a linear fit for the Brown *et al.* data for the temperature range between 20 to 110 K, shown in Figure 3.10. The temperatures with laboratory conditions are significantly higher than those from the models using dark cloud and protoplanetary disk conditions to acquire the same density.

Table 3.2: Ice densities grown with deposition rates representative of dark cloud and protoplanetary disk regions are shown with the corresponding temperature at which ices grown using laboratory conditions have the equivalent density.

Model Temp (K)	Dark Cloud ρ (g cm^{-3})	Temp Equivalent (K)	Protoplanetary Disk ρ (g cm^{-3})	Temp Equivalent (K)
10	0.618	32	0.609	28
20	0.648	43	0.624	34
30	0.676	53	0.647	43
40	0.759	84	0.679	54
50	–	–	0.721	70
60	–	–	0.765	86
70	–	–	0.838	113

3.2 Conclusions

The simulations presented here demonstrate a good match with experimentally determined amorphous water-ice densities. While the basic models produce a poor fit to lower temperature results (<80 K), they indicate that the production and prevalence of porous structures is significantly controlled by non-thermal diffusion. The modification of the model to incorporate a non-thermal diffusion mechanism based on the kinetic energy gained through the adsorption process allows the laboratory data to be well reproduced over all measured temperatures.

The degree of porosity under various conditions may be determined through ice-density measurements, which can also be calculated for the simulated ices. However, the models also indicate that the physical scales associated with the porosity can change, with higher temperatures and lower deposition-rates producing smoother ice surfaces with wider pores.

Simulations of ices produced with fixed angles of deposition are more difficult to compare directly with laboratory data, due to the lack of direct density measurements, but the trends with temperature, angle and deposition rate are appropriately reproduced, with the exception of the results for deposition normal to the surface. A more detailed computational reproduction of all laboratory conditions, including the adsorption of porosity tracers like N_2 will allow such discrepancies to be explored in their proper context.

We note that, while the experiments and simulations considered here involve pure water ices, interstellar ices consist of mixed water, CO and CO_2, as well as other components. Direct deposition of water ice is also unlikely to be the dominant interstellar ice formation mechanism, and experimental deposition rates are typically larger than those that are expected in the interstellar medium. The use of detailed kinetic models of laboratory ice deposition are therefore valuable in allowing experimental results to be understood in terms of microscopic kinetic processes, allowing extrapolation to interstellar conditions using the models.

Specific conclusions from this work include:

• The requirement of non-thermal diffusion in the formation of laboratory ices appears essential to explain low-temperature porosity measurements.

• We suggest that the energy gained by the adsorption of a water molecule to the surface is sufficient to produce enough diffusion to match experimental ice densities. A combination of one or two hops for ∼70% of newly-adsorbed water molecules is adequate to correct for the failure of the model at low temperatures. The majority of hops produce a net displacement of two surface sites from the original adsorption site. Around three quarters of the adsorption potential must be converted to kinetic energy of the adsorbed molecule to produce this result.

• Application of the model to protoplanetary disk conditions (in which direct deposition of water ice onto dust grains may be the dominant mechanism) suggests that laboratory ice porosities may be higher than those in protoplanetary disks at temperatures above 40 K. Under dark interstellar cloud conditions, laboratory ices were found to be too porous, under all temperature conditions tested.

4

Amorphous Water Surface Area

Contents

The work presented here was in collaboration with Jiao He, SM Emtiaz, Francis Toriello, and Gianfranco Vidali and has been published in The Astrophysical Journal.[46] A number of the plots below were taken from the publication to clarify and give context to the modeling provided.

As discussed in the introduction, H_2O acts like a reservoir for species, which may provide material for chemical reactions. Further, the ice may act like a third body allowing energetic reactions to occur that would otherwise destroy their newfound products. Laboratory measurement of the surface area available for catalysis is therefore important for understanding the chemistry on and in ice mantles. However, the question still remains whether the ice mantle covering dust grains is porous or compact.

It was initially thought the use of infrared features known as OH dangling (dOH) could establish the porosity of water ices. Two features are present at 3720 cm^{-1} and 3696 cm^{-1} for double and triply coordinated water molecules, respectively. [15, 27]. Experimental studies [69, 77, 54, 64] show that the total number of dangling bonds is not proportional to the porosity, and some porosity is retained when the signature of dangling bonds disappears. This is an important point, since dOH IR signatures have not been seen in observations so far [55]. It is also known that the position and strength of dOH dangling bonds are affected by the presence of other atoms or molecules (see [48] for a recent investigation of change in the IR bands of the dangling bonds due to adsorption of H_2, D_2, Ar, CO, N_2, CH_4, and O_2). Furthermore, the thermal treatment of ASW irreversibly changes the network of pores: as the temperature is increased, the ice morphology changes, and pore collapse occurs. In this work, we investigate again the relation between dOH bands and porosity and hope to find new insights into this decades-old problem.

Compared to the numerous studies which focus on measuring the porosity (or equivalently the density) of the ASW, fewer details are available about the link between morphology and catalytic properties of ices. [77] performed energetic ion bombardment of ASW and found that the surface area of porous ice decreases at a faster rate than the pore volume during ion-induced compaction. The underlying reason for this difference is still not well understood, but several mechanisms have been proposed, including coalescence of micropores, preferential destruction of smaller pores, and smoothing of pore wall topology [77]. Prior laboratory measurements of porosity based on density [11, 16] do not reflect the true catalytic potential of the ASW surface. It is important to measure the pore surface area that is accessible for the adsorption of volatiles from the gas phase. [69] studied the accessible pore surface area after compaction of the ASW by energetic ions. However, in highly shielded clouds, thermal processes should dominate over energetic processing, and the temperature dependence of the pore surface area is most important. One of the main goals of this study is to fill this gap and use the infrared absorption spectrum of CO as a tool to quantify the temperature dependence of the catalytic surface area that is accessible by volatile molecules condensed from the gas phase.

4.1 Laboratory Setup

Detailed description of the apparatus can be found in previous publications [50, 48]. Experiments in this study were carried out using an ultra-high vacuum (UHV) apparatus with a base pressure of 4×10^{-10} Torr. A gold coated copper disk was used as a grain analog. Ices were grown utilizing background deposition using a precision leak valve. Ice on the sample are measured using a Fourier Transform InfraRed (FTIR) spectrometer in the Reflection Absorption InfraRed Spectroscopy (RAIRS) configuration. First 200 ML of porous ASW were deposited at 10 K, then the ice was heated at a ramp rate of 3 K $minute^{-1}$ to 200 K. The RAIR spectra were measured continuously during the heating and the two dOH bands were monitored.

The RAIR spectra were measured continuously during the heating. Next, a set of experiments where CO was deposited on top of 200 ML of ASW, then was subsequently annealed. ASW samples were grown at 10 K, and then annealed at 20, 40, 60, 80, 100,

120, and 140 K for 30 minutes. Afterward, the ice sample was cooled back to 20 K (except for the 20 K annealing) before depositing CO until the ASW pore surface was saturated, as indicated by the emergence of the longitudinal optical (LO) mode of CO at ∼2143 cm^{-1}. The CO deposition temperature was chosen to be 20 K, because at this temperature, CO has enough mobility on the surface of p-ASW to access the pores of ASW. (He et al. 2018b)

4.2 Modeling

To duplicate laboratory parameters water is deposited at interstellar temperatures (10 to 20 K) and then heated at laboratory rates (1 to 3 K min^{-1}) up to a temperature of 150 K. First, the water molecules are deposited using background deposition onto a square surface of length 650 Å. A deposition rate and temperature of 10^{13} cm^{-2} s^{-1} 10 K were used to replicate the methods above and two thicknesses were tested (25 ML and 200 ML). Surface area and density are calculated for each ice and measured during heating.

The ice surface area (including pore surfaces) is calculated by counting the number of surface molecules. This value is then divided by the total number of water molecules in the ice. This ratio corresponds to the fractional coverage of surface to the total ice thickness in monolayers. With the microscopic model the surface coverage can be directly measured instead of using a proxy like those used in He et al. 2019, such as adsorption of CO or another volatile species. [46] Images were created using the freeware POV˘Ray to visualize the entire ice or cross sections to see the connectedness of the pores.

4.3 Results

4.3.1 Infrared characterization of pure ASW

ASW has three main absorption modes in the mid-infrared region: OH stretching at ∼ 3300 cm^{-1}, the bending mode at 1640 cm^{-1}, and the libration mode at ∼ 700 cm^{-1}. Two smaller features on the OH stretching mode at 3720 cm^{-1} and 3696 cm^{-1}, indicating the dangling OH bonds, are the focus of this work. These features are generally attributed to three-coordinated and two-coordinated water molecules, respectively (Buch & Devlin 1991). The dOH region of the laboratory RAIR spectra for 200 ML ASW during heating is shown in Figure 4.1. As the ice temperature is raised, both dOH bands decrease. By 70 K, the 3720 cm^{-1} band is almost gone, while the 3696 cm^{-1} band persists until above 140 K. To quantify the temperature dependence of both bands, Gaussian and Lorentzian fits were used. The fitting is described in more detail in the publication.[46] Typically, disordered ices have relatively broad Gaussian line shapes, while crystalline ices have narrower Lorentzian line shapes. The band areas of both dOH bands during warming of the 200 ML ASW are calculated and presented in Figure 4.2. At ∼60 K, the 3720 cm^{-1} band becomes negligible, which suggests the disappearance of two coordinated dangling bonds. This is consistent with previous experimental studies [77, 14]. While the

3696 cm^{-1} band drops linearly with temperature from 60 K to above 140 K. It does not disappear completely as shown in Figure 4.2.

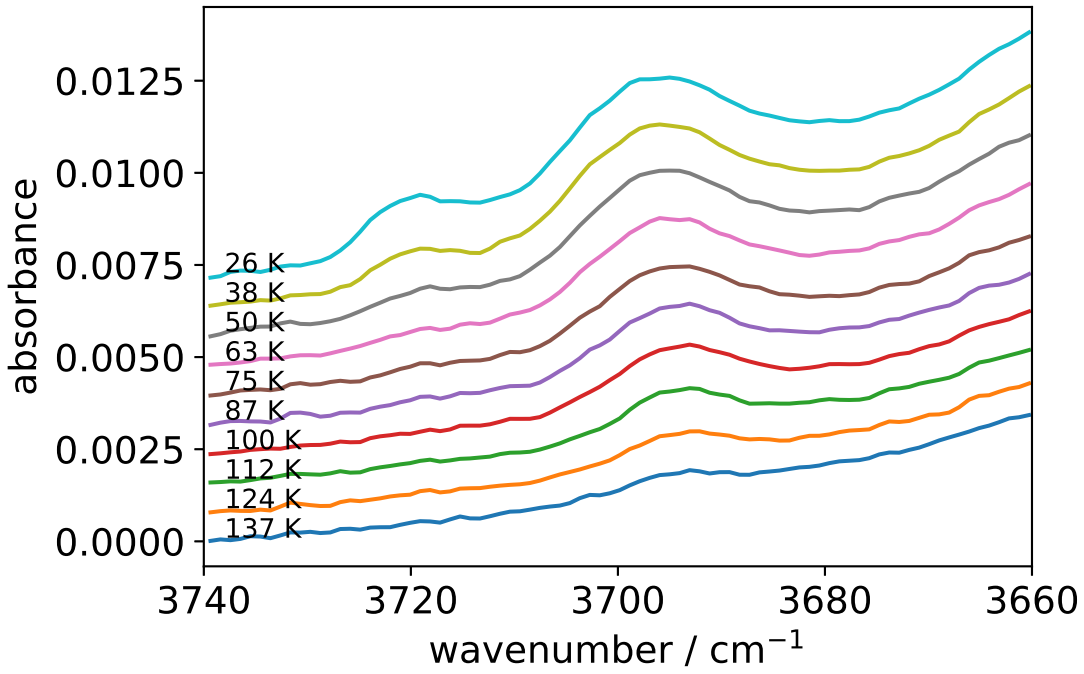

Figure 4.1: RAIR spectra of 200 ML water ice during heating at various temperatures. The water ice was deposited from the background when the surface was at 10 K. The heating ramp rate is 3 K/minute. Spectra are offset for clarity.

4.3.2 CO on ASW

In a second set of experiments, we use the infrared bands of CO to probe the pore surface area of ASW annealed at different temperatures. It is well established that the infrared absorption feature of CO interacting with water is different from that of pure CO. The RAIRS of pure CO shows the longitudinal optical (LO) mode at 2143 cm^{-1}, while CO interacting with water shows two bands at ∼2140 cm^{-1} and ∼2152 cm^{-1}.

According to our previous laboratory measurements, the diffusion of CO on the surface of porous amorphous solid water (p-ASW), becomes significant at about 15 K. [49] At 20 K, the diffusion is very efficient. If CO is deposited on top of ASW at 20 K, where diffusion is very efficient, this allows CO to diffuse into the pores and occupy the pore surface of the ASW. Once the water surface area is covered by CO, the pure CO LO feature begins to grow. By examining the amount of CO deposited when the LO peak emerges, the accessible surface area of p-ASW can be obtained.

There have been several experimental studies of the interaction between CO and ASW surface [e.g. 35, 23]. Although it is generally accepted that the ∼2152 cm^{-1} feature is due to the adsorption of CO on the dOH sites of ASW, no direct experimental evidence in the literature demonstrates a direct correlation between dOH bands and the 2152 cm^{-1}

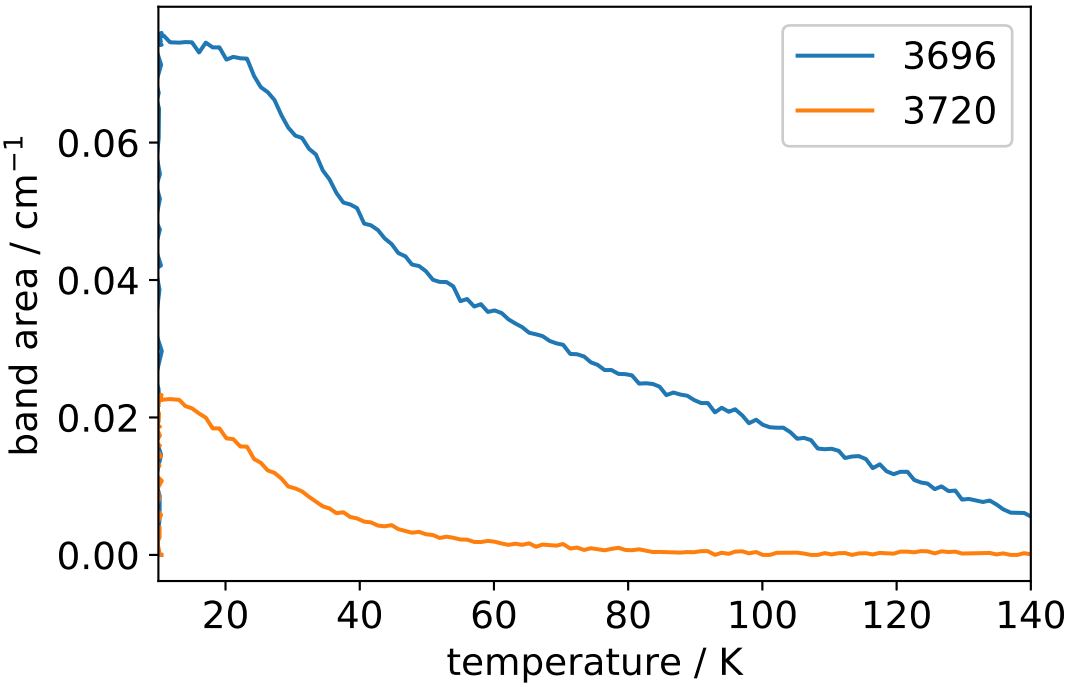

Figure 4.2: The area of the two dOH absorption bands during warming up of a 200 ML water ice grown at 10 K and heated at 3 K/minute.

component. Thus, we used two Gaussian functions to fit the 2140 cm^{-1} and 2152 cm^{-1} components, and one Lorentzian function to fit the 2143 cm^{-1} component, and then we studied how these three components change with CO deposition dose.

As was discussed in [48], introducing CO in ASW shifts the dOH bands. In Figure 4.3, the dOH region of the RAIRS spectra before and after the CO deposition is shown. Before CO deposition, the dOH band is at 3694 cm^{-1} (there is a slight shift of dOH position from 3696 cm^{-1} to 3694 cm^{-1} when annealed at 60 K), while after CO deposition, the area of the 3694 cm^{-1} peak decreases to zero and transitions to ∼3636 cm^{-1}. We used one Gaussian function to fit the 3694 cm^{-1} peak and one Gaussian function to fit the 3636 cm^{-1} peak and obtained how the two peaks change with increasing CO deposition. The area of the 3694 peak is shown in Figure 4.4, together with the peak areas of the three components of C-O stretching mode. Between 0 and 12 ML, the 3696 cm^{-1} band area decreases to zero. At the same time, the band area of 2152 cm^{-1} component increases from 0 to the saturation level. The anti-correlation between these two bands is evident. This is direct evidence that the 2152 cm^{-1} component is associated with CO binding to the dOH bonds.

At about 27 ML of CO deposition, the 2140 cm^{-1} band begins to saturate, while at the same time the 2143 cm^{-1} LO band emerges. This demonstrates that at about 27 ML of CO deposition, all the pore surface area is occupied, and "pure" CO starts to build up. We take the CO dose at which 2143 cm^{-1} component just starts to show up, 27 ML in this case, to be the pore surface area. The fact that the 3694 cm^{-1} band disappears after CO deposition indicates that all of the pore surface area is accessible for CO adsorption, and there is no isolated cavity inside the ASW. Therefore 27 ML is the accessible and the total pore surface area of the 200 ML ASW annealed to 60 K.

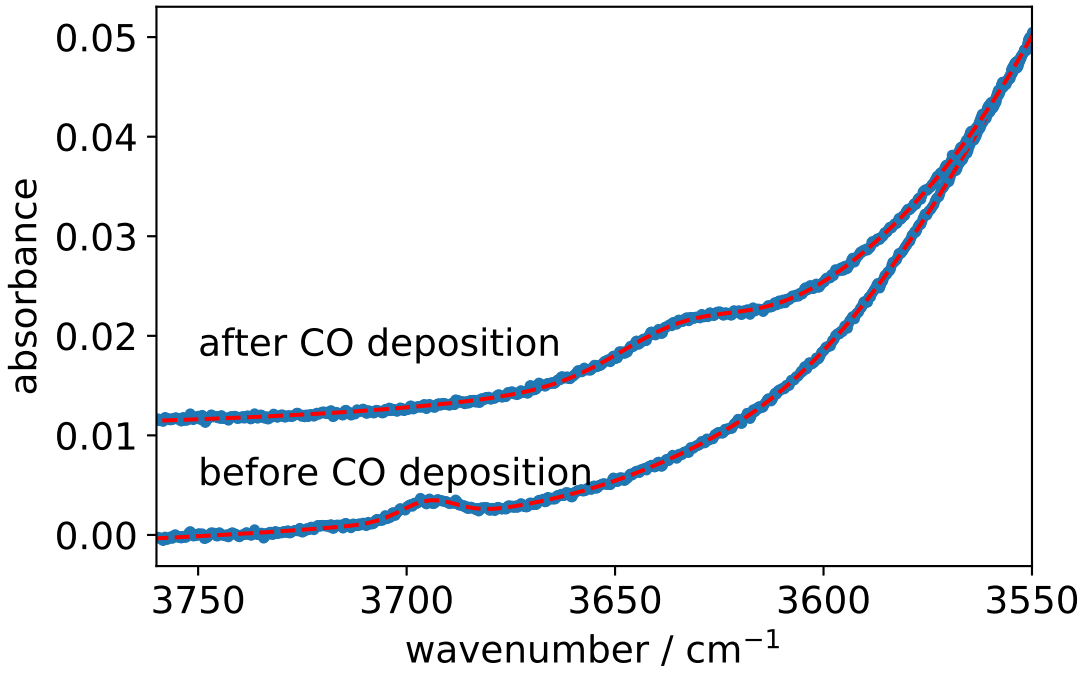

Figure 4.3: The dOH region of the RAIR spectra of 200 ML water ice annealed at 60 K and cooled down to 20 K (1) ; and after CO deposition (2). Dashed lines are the fitting. Spectra are offset for clarity.

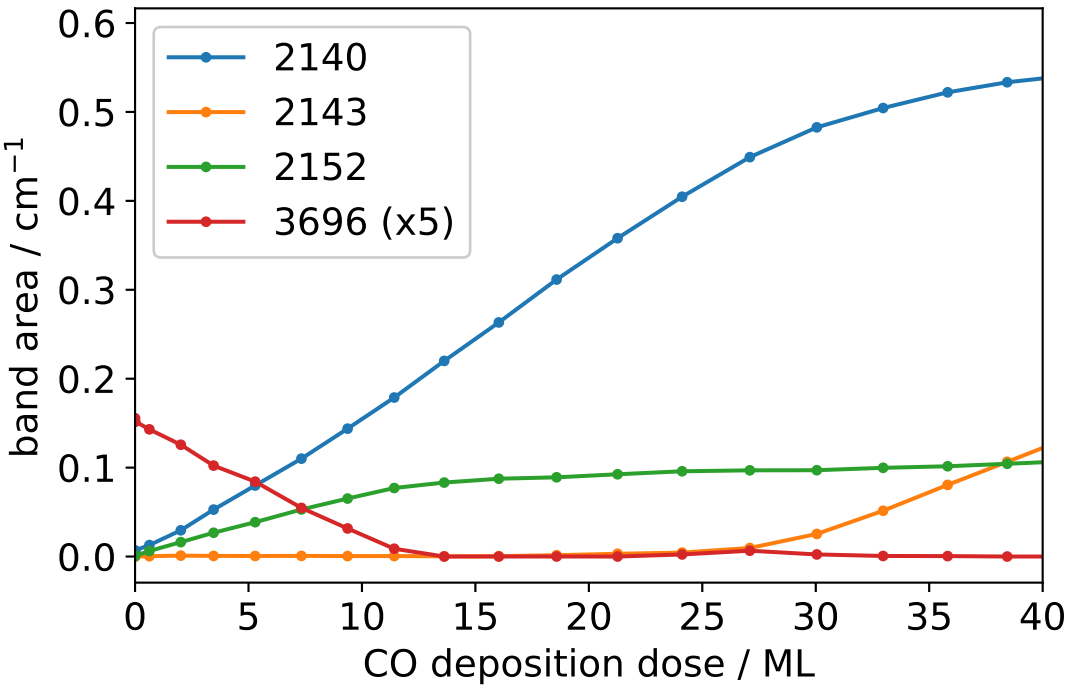

Figure 4.4: The band area of the three components of the CO absorption profile and the dOH band at 3694 cm^{-1} during CO deposition on 200 ML ASW annealed to 60 K.

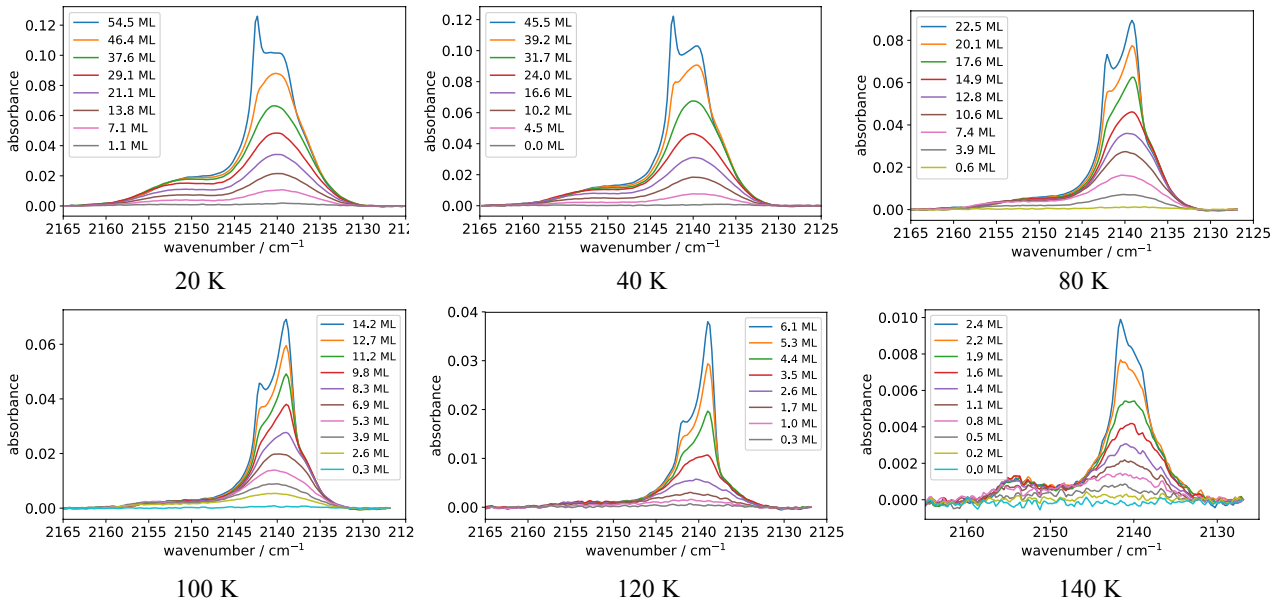

Figure 4.5: The RAIR spectra of CO deposited on top of 200 ML ASW that is annealed at 20, 40, 80, 100, 120, and 140 K, and cooled down to 20 K. The CO dose for each spectrum is shown in the inset.

Similar CO depositions at 20 K were carried out on 200 ML ASW samples that were annealed at 20, 40, 80, 100, 120, and 140 K. RAIR spectra were recorded during CO depositions at 20 K. We determine the pore surface areas for the ASW annealed at different temperatures by visually examining the CO deposition dose at which the 2143 cm^{-1} component emerges. The ASW surface area versus annealing temperature is shown in Figure 4.6. The pore surface area decreases linearly with annealing temperature almost up to 120 K, above which the surface area becomes about 2 ML. Consider that the surface of ASW is rough, 2 ML is probably due to the very top of the surface, i.e., the ice–vacuum interface. The ice becomes fully compact at 140 K.

4.3.3 Trapping of CO in ASW

In the previous section, we focused on the infrared spectra during CO depositions. Here in this section, we focus on the TPD stage of the same set of experiments. After deposition of CO on ASW at 20 K, the ice was heated up from 20 K to 200 K at a ramp rate of 0.1 k/s while RAIR spectra were measured continuously. The band area of the C-O stretching mode was calculated for each spectrum during warming up (see Figure 4.7). For ices that are annealed at 80 K and above, the C-O stretch band area becomes zero after the temperature reaches above 60 K. In the figure, the desorption of CO from the ice can be separated into three regions. The first region is below about 55 K, which is the temperature at which CO on ASW surface (including the surface of pores) desorbs. The second region is from about 55 K to about 150 K, during which the CO band area drops linearly with temperature. CO molecules that are trapped in the ASW matrix are released back into the gas phase gradually. Here we don't exclude the possibility that the band strength of CO buried inside bulk ASW can change with temperature. Indeed,

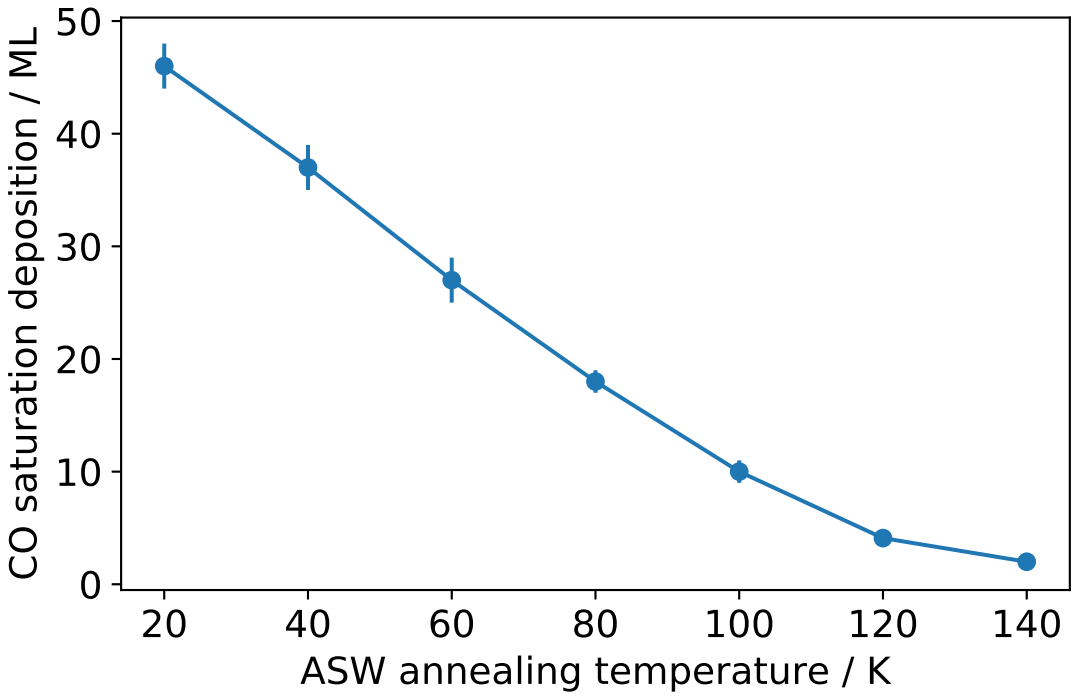

Figure 4.6: Accessible pore surface area in 200 ML of ASW that are annealed at different annealing temperatures. The pore surface area is measured by the amount of CO that fully covers the pore surface.

experimental measurements by [79] have found that the band strength of C-O stretching for CO buried in water ice has a reversible component that decreases almost linearly with temperature between 50 K and 120 K. The irreversible component corresponds to the gradual releasing of CO from the bulk ASW. The third desorption profile occurs when the ASW crystallizes, and all of the remaining CO molecules are forced out of the ice. This is sometimes referred to as the "molecular volcano" [81]. The amount of CO that is in the ice at about 60 K represents the CO that is trapped inside the ASW matrix, and we define it as the trapping amount. When the ASW is annealed at 60 K or above, the ASW does not trap any CO. The lower the annealing temperature, the more CO molecules that can be trapped. The linear decrease of C-O stretching band area during heating is similar to that of CO_2 (see Figure 4 of [47]). This suggests that the linearity may be a general phenomenon that occurs to all volatiles that are trapped in ASW.

4.3.4 Dangling OH bonds during CO deposition

During CO deposition on ASW, as the pore surface is gradually covered by CO, the dOH band at 3694–3696 cm^{-1} decreases, and the band at 3636 cm^{-1} increases. A fitting was as discussed in the paper [46] to obtain the area of the dOH band during CO deposition. Figure 4.8 shows the area of the 3694 cm^{-1} dOH band during CO deposition for ASW that are annealed at different temperatures and cooled to 20 K. For the ASW that was annealed at 140 K, the dOH band area is too small, and is not presented in the figure. For annealing temperature of 20 K and 40 K, there are two dOH bands after annealing,

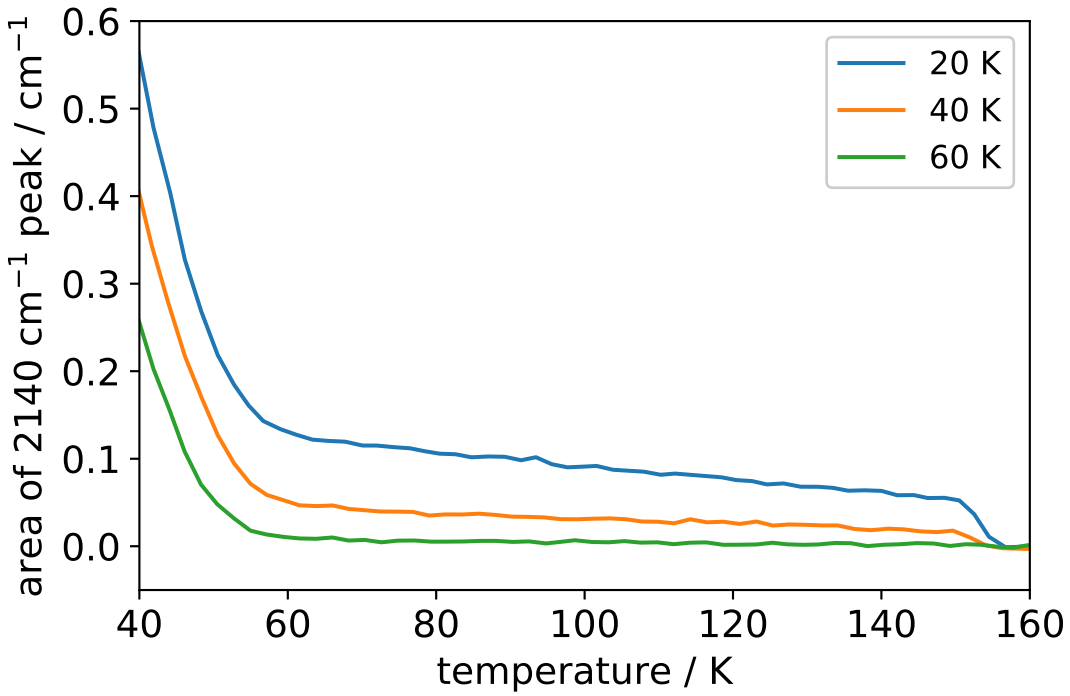

Figure 4.7: Band area of the 2140 cm^{-1} peak during warming up of (1) CO adsorbed on ASW that is annealed at 20 K; (2) CO adsorbed on ASW that is annealed at 40 K and cooled down to 20 K; (3) CO adsorbed on ASW that is annealed at 60 K and cooled down to 20 K.

and the fitting of the peaks is more complicated and are not considered here. The main finding from Figure 4.8 is that the dOH always drop to zero at high enough CO doses, regardless of the annealing temperature. This suggests that all of the pore surface inside the ASW is accessible to CO, and the pores throughout the whole ice are interconnected. This agrees with the previous results by [76] which demonstrated that all of the pores are interconnected and are accessible to CH_4 adsorption.

4.3.5 Modeling of ASW Ice Porosity

Figure 4.9 shows the structure of simulated water ice; the column-like structure becomes smoother with increasing temperatures, until eventually an entirely smooth structure is obtained at 140 to 150 K. In the model, the initial ice was deposited at 10 K and then heated to ∼150 K where the ice starts to desorb into the gas phase. The first two images of the model (at 10 and 70 K) have essentially the same structure. The model indicates there is little to no re-arrangement of the ice until the temperature of 60 K is reached. At 60 to 80 K, diffusion of water becomes efficient enough to play a role in the surface area and porosity, and only increases at higher temperatures. The structure begins to smooth, by eliminating first the smaller pores until gradually all the pores are removed. Through this process, the ice reaches its maximum density at 150 K. It is important to note the model does not include the phase change from amorphous to crystalline ice, which would occur at ∼140 K; this does not alter the results of the model as the main focus is between temperatures of 10 to 140 K.

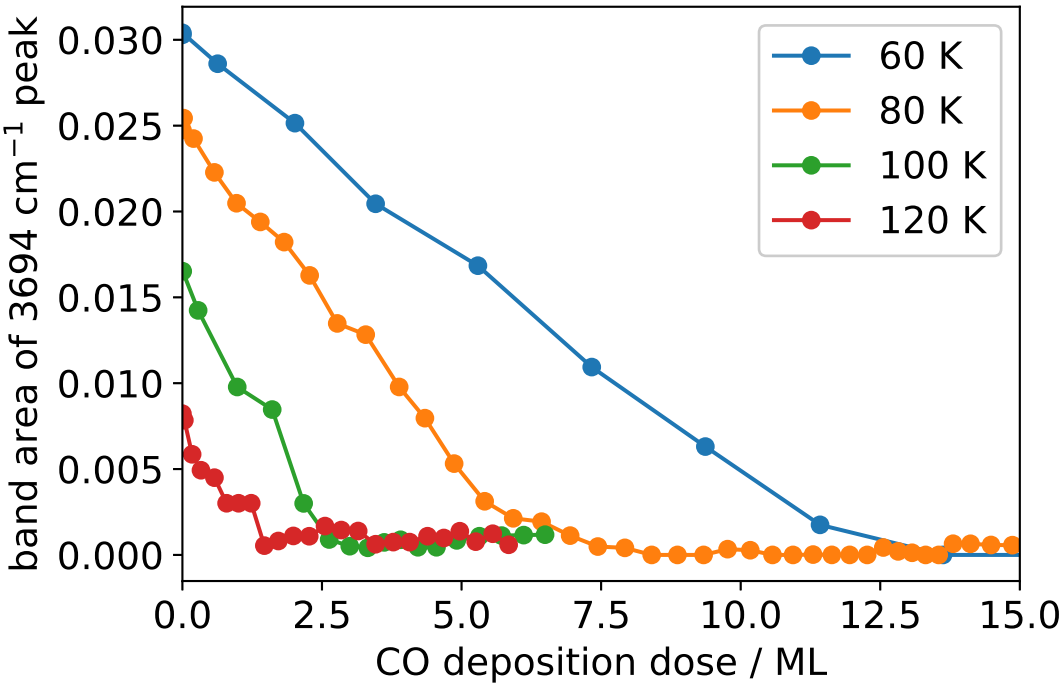

Figure 4.8: Band area of the dOH bond absorption at 3694 cm^{-1} after deposition of CO on 200 ML ASW that is annealed at 60, 80, 100, and 120 K, and cooled down to 20 K.

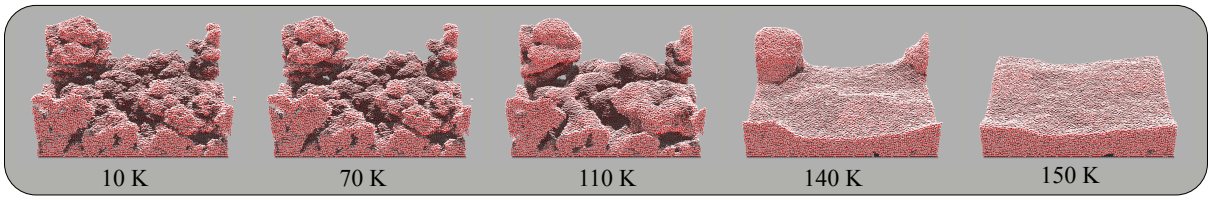

Figure 4.9: A 25 ML amorphous water deposited and heated at 3 K min^{-1} to 160 K.

In the laboratory results shown in Figure 4.5, we see that the accessible surface area decreases steadily up to 140K. As stated above, the 3-coordinate dOH absorption band (3694–3696 cm^{-1}) linearly decreases from 60 to 140 K, likely corresponding to the decrease in the surface area; this matches the decrease of the exposed surface in the model. As seen in Figure 4.10 the coverage steadily decreases after 80 K is reached. Until that temperature is reached, very little rearrangement and pore collapse occur; this is probably due to the fact that the model uses isotropic potentials and is not sensitive to defects (OH dangling bonds) which the experiment is sensitive to. However, within the model we see a reasonable match at lower temperatures given that CO is a proxy for the extent of the accessible exposed H_2O network.

Figure 4.11 shows the interconnectedness of the pores. A portion of ice was imaged to show the inner structure and not the total structure. Visually it shows that most pores are connected within the shown plane. As the ice is heated the pores collapse until eventually empty cavities within the water ice are left. The cavities appear to be the remnants of the initial column-like structure, which minimize their potentials by forming approximately spherical structures. The encapsulated pores are fairly small in size with

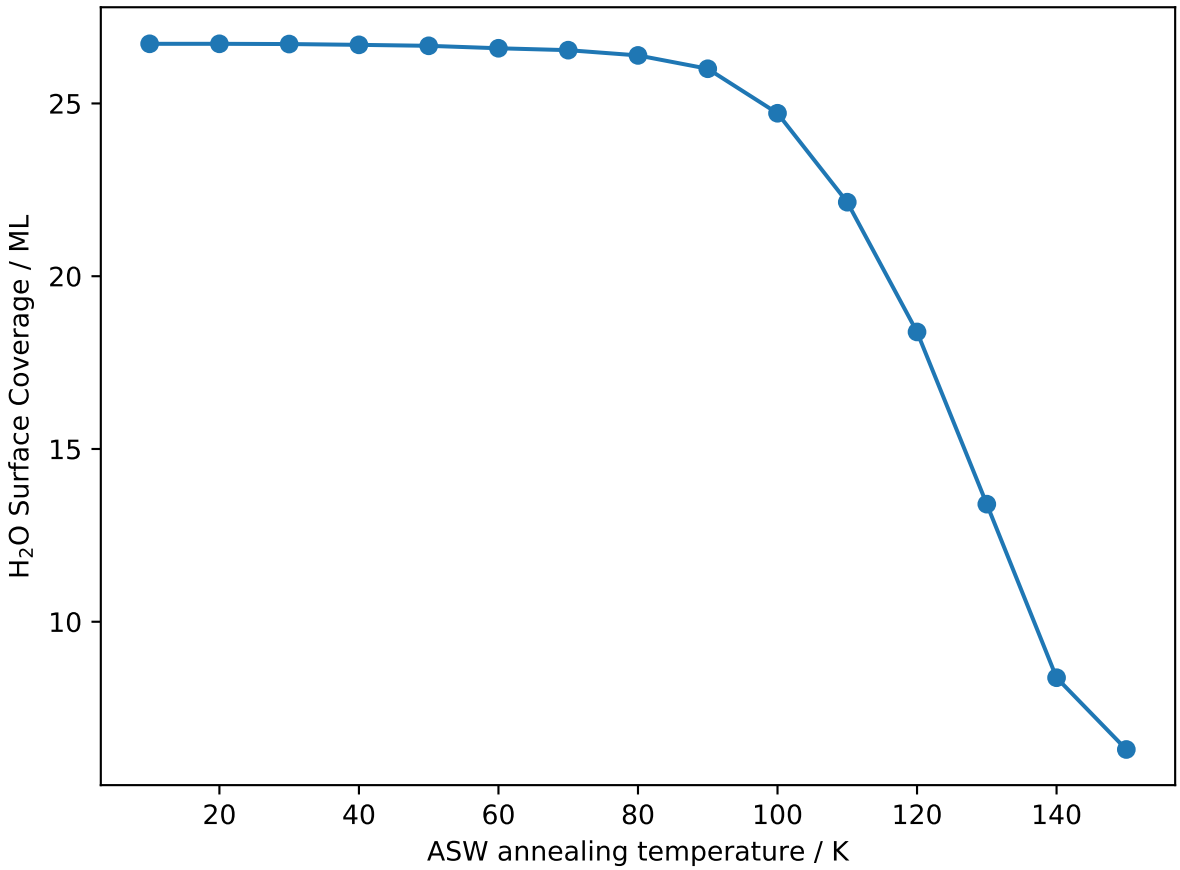

Figure 4.10: Accessible pore surface area in the model of ASW as is heated at a 1 K min^{-1}. The pore surface area is measured by the percentage of surface to total water molecules. The error bars are calculated by using both 25 and 200 ML model coverages.

widths around 2 to 3 nanometers. These cavities may allow entrapment of some volatile species such as CO until a later temperature. By 150 K all cavities have collapsed, and the volatiles have either been desorbed or are stuck within a water matrix.

4.4 Discussion and Astrophysical Implications

One of the main spectroscopic pieces of evidence of porous ASW is the presence of dOH bonds, which have been seen in numerous laboratory experiments. Whether the infrared signature of dOH bonds at 3696 cm^{-1} and 3720 cm^{-1} is a good measurement of porosity has been debated. [69] performed energetic ion bombardment on ASW and found that the decrease of pore surface area is four times less than the decrease in dOH absorption. From this experiment, one might conclude that the dOH band area is not proportional to the pore surface area. However, ion bombardment also induces chemistry that produces molecules such as O_2, O_3, H_2O_2, which may interact with the dOH bonds and shift or shield the dOH bands [48]. It is unclear from their experiments what is the relation between dOH band area and pore surface area for pure ASW. In this regard, thermal

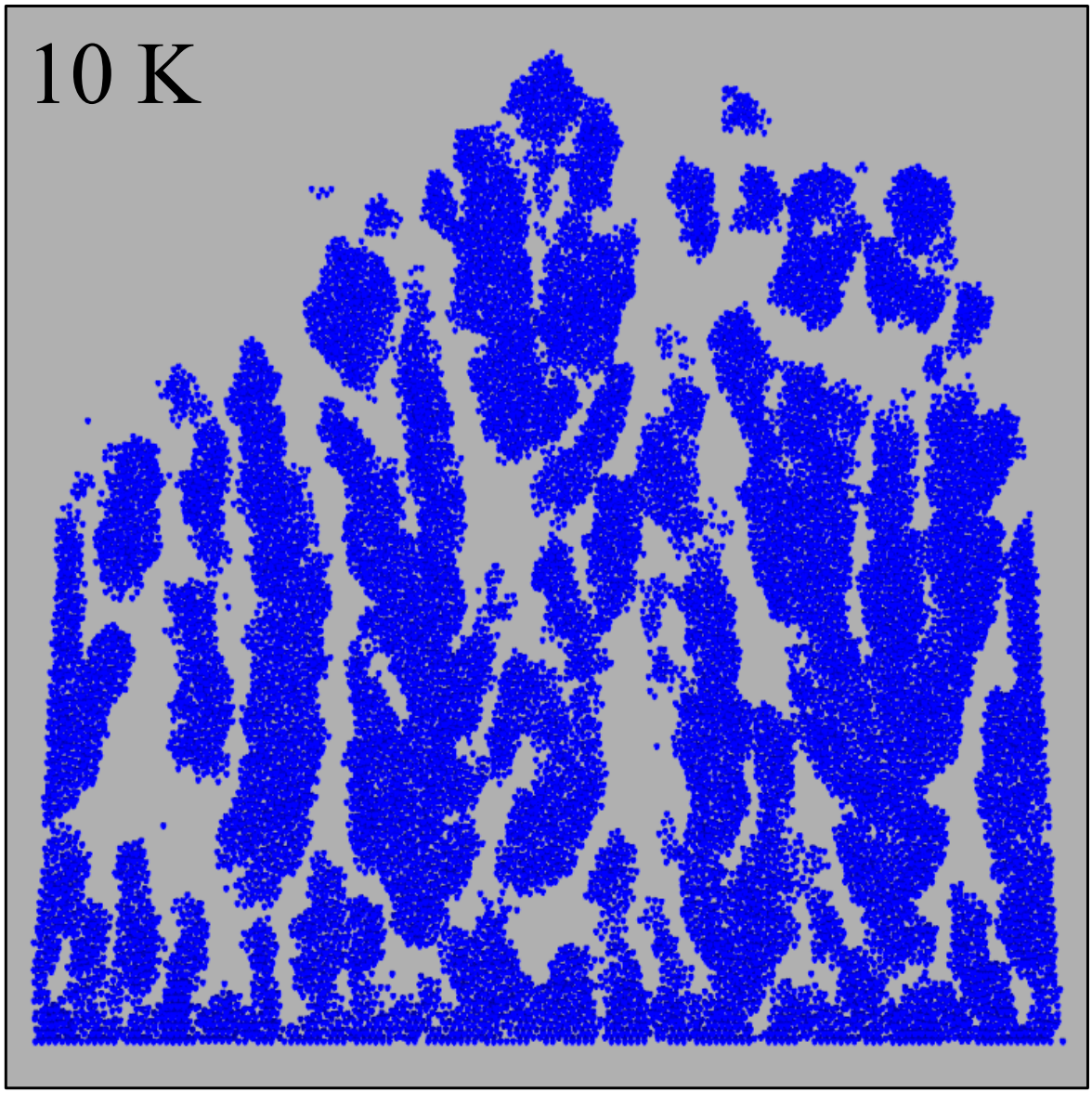

Figure 4.11: A slice of a 200 ML thick amorphous water deposited at 10 K imaged with POV˘Ray. The thicker ice was used to demonstrate the connected as it was a more obvious than in the much thinner ice of 25 ML.

processing of ASW is a more appropriate experiment. There have been experiments that focused on thermal processing of ASW [10, 11, 54]. However, those studies quantified the density of the ice instead of the pore surface area. In this study, we measured the pore surface area of ASW that is annealed at different temperatures, and also quantified the temperature dependence of dOH band area during heating of ASW. Additionally, we used a kinetic Monte Carlo model to determine the porosity of ASW during heating, by computing directly the total number of surface molecules. We have shown in Figure 4.2 that the 2-coordinated dOH (3720 cm^{-1}) decreases sharply between 10 K and 60 K, and disappears almost completely by ∼60 K. There is possibly a smoothing of the pore surface or merger of smaller pores to form larger ones. The 3-coordinated dOH absorption band (3694–3696 cm^{-1}) decreases almost linearly between 60 and 140 K. This linear decrease with temperature can be compared with the linear decrease of pore surface area shown

in Figure 4.6. Both seem to decrease linearly with temperature, although the curve in Figure 4.6 drops to the minimum at a slightly lower temperature that in Figure 4.2. This small difference can be explained by the fact that in measuring the pore surface area using CO adsorption, ASW was annealed for 30 minutes, while when measuring the dOH bands shown in Figure 4.2, the temperature was ramped up continuously without the annealing step. The comparison between these two figures suggests that at least under our experimental conditions, the infrared absorption band of 3694–3696 cm^{-1} seems to be a good measurement of the pore surface area in the temperature range from 40 K to 140 K.

The presence of cavities inside ASW has been reported or mentioned in several prior studies [31, 53, 94]. However, it is unclear whether these cavities are closed inside the bulk ASW or interconnected and accessible from the vacuum–ice interface. In Figure 3 of [77] and Figure 8 of [16], it was hinted that there are closed cavities, but there was no discussion about the connectivity of the cavities. In Figure 4.8 in this work, it is evident that after CO adsorption, the 3694 cm^{-1} band always drops to zero, regardless of the annealing temperature. This suggests that the there is a negligible number of closed cavities inside the bulk ASW, and almost all of the cavities (pores) are connected to the vacuum–ice interface. Further, the model presented here shows that volatile species should indeed be able to access all of the surface, but at higher temperatures the collapse of the pores leads to pockets within the ice that could trap volatiles and prevent other species from sticking. This conclusion holds for both ice thicknesses tested (25 and 200 ML). This is in agreement with the experimental results of [76], who found that the number of closed pores is insignificant in a 1000 ML ASW. However, we have to point out that this conclusion may not be applicable to an ASW much thicker than 1000 ML. [13] reported that thick ASW may crack spontaneously during growth or during warming up. It remains a question how the spontaneously cracking affects the connectivity of the cavities/pores inside ASW.

From Figure 4.8, we can also reach a conclusion that all of the dOH bonds are located on pore surface instead on inside the bulk ASW. On the surface of pores, a water molecule can form 2, 3, or 4 bonds with neighboring water molecules, and they are called 2-, 3-, or 4-coordinated, respectively. Figure 4.2 shows that as long as the ASW is heated to ∼60 K, 2-coordinated water molecules disappear, leaving 3- and 4- coordinated molecules. Based on the comparison of Figure 4.6 with Figure 4.2, we can see that between 60 K and 140 K, the number of 3-coordinated water molecules is roughly proportional to the total pore surface area. This indicates that the ratio between 3- and 4-coordinated water molecules is constant. Other than the differing in the total pore surface area, the properties of the pore surface should remain the same between 60 and 140 K. From a laboratory perspective, this suggests that in some scenarios, one may be able to carry out experiments on a porous ASW that is annealed to 60 K, and the result would be the same—aside from a scaling factor— as that on an ASW that is annealed to 140 K, which has a compact structure. Since experiments on a porous ASW would in general have a much higher sensitivity than on the very top surface of a compact ASW, this conclusion is very useful in laboratory studies of ASW. One example of its application is presented in [48], who measured the diffusion of volatile molecules on the surface of porous ASW. Conclusions in that study would be applicable to the surface of any ASW (porous or compact) that is annealed to 60 K and above.

The surface of ASW is known to catalyze the formation of molecular species on dust grains in the ISM. Porous ASW possesses a specific surface area up to a few hundred

m^2g^{-1} and therefore may account for most of the catalytic surface on the dust grains. Even if ASW undergoes thermal processing, significant residual porosity may be retained [54]. However, it was unclear how much of the residual porosity can actually contribute to catalysis of chemical reactions. The key question here is whether these remaining pores are closed cavities buried inside the bulk ice, or they are accessible to volatiles from gas adsorption. Our experimental results in Figure 4.8 show that all of the dOH in the ASW can be covered by CO molecules, which suggests that all of the pore surface area is accessible for reactive species condensed from the gas phase. The large pore surface actually contributes to the catalysis of the formation of complex species in the ice. The fact that all pores are connected all the way to the vacuum–ice interface suggests the possibility that volatile molecules that are formed on the pore surface can diffuse and desorb from the ice before the desorption of water. The desorption of molecules before water desorption has the potential to explain the observations which found complex organic molecules in regions with high-extinction [86, 1] and regions outside the water snow line in protoplanetary disks [68].

4.5 Conclusions

In this study we used the infrared absorption spectrum of carbon monoxide as a tool to measure the pore surface area of amorphous solid water grown by vapor deposition and annealed at different temperatures. A kinetic Monte Carlo model was used to visualize the porosity and measure the surface area directly. Below are the findings from this study:

- The total pore surface area in 200 ML of ASW at 20 K is equivalent to 46 ML, and decreases linearly with annealing temperature to 120 K.
- All pores are connected to the vacuum–ice interface and accessible for volatiles adsorption.
- All dangling OH bonds, as inferred by the 3696 cm^{-1} and 3720 cm^{-1} features, reside on the surface of pores.
- The 3720 cm^{-1} dOH band, which is due to 2-coordinated water molecules, disappears when the ASW is heated to 60 K.
- The 3696 cm^{-1} dOH band, which is due to 3-coordinated water molecules, decreases more or less linearly between $\sim$50 K and 140 K.
- The ratio between 3- and 4-coordinated water molecules on the surface of pores remains constant between 60 K and 140 K; this indicates that the surface properties, as adsorption of volatiles is concerned, do not change significantly in this temperature range, except for the change in the total surface area.
- The 2152 cm^{-1} absorption peak observed for CO on ASW is due to the interaction of CO with dOH bonds on pore surfaces.
- ASW annealed to 60 K or above loses the capability to trap CO molecules from the gas phase indicating that the remaining pores close off and form pockets.

5

CO Diffusion on ASW

Contents

Amorphous solid water (ASW) ice has been shown experimentally to be capable of incorporating and trapping other chemical components such as CO, CO_2, NH_3, CH_3OH [21] and potentially more complex organic molecules [38]. The trapping of these species may have a substantial effect on the chemistry both within ice mantles and in the gas phase during the star- and planet-formation process.[87, 18, 80, 74] The trapping efficiency in laboratory-deposited ices is dependent on the ice morphology; for instance, porous amorphous water ice has been shown to absorb 20-50 times more gas (such as N_2, CO, Ar, O_2, and CH_4) than compact water ice [4]. The rates of chemical reactions involving the adsorbed molecules may also be affected by the underlying water ice structure. For example, hydrogenation of both CO and C_2H_4 occurs more frequently on ASW than

on crystalline ice due to an increase in the sticking coefficient and adsorption energy of the H atoms on ASW.[59, 52] These structural effects will be important to simulations of interstellar ices, in which chemical reactions are critical to both the composition and structure of the ice [40]. It is therefore necessary that structural treatments become available for interstellar grain-surface kinetics simulations and that these treatments also be consistent with the available experimental data. Before we can account for trapping within ices, the diffusion of volatile species such as CO must be understood, because this will dictate where CO will move within an ice before temperatures are achieved that result in desorption.

Laboratory studies have used infrared spectroscopy to measure diffusion barriers of CO layered with H_2O ices. The polar environment of water can shift the pure CO band at 2139 cm^{-1} and produce two spectral features at 2152 and 2137 cm^{-1}; [63] used these to track the amount of CO diffusing into a porous water ice, analyzing the mixing ratio data with a Fickian diffusion model. The surface diffusion barrier was found to be 160 K, lower than standard values used in astrochemical simulations. Other research has utilized IR spectroscopy, but instead measures mixing by observing the shift in the water dangling hydrogen bond (dOH) at 3635 cm^{-1}. The diffusion barrier associated with the change in the dOH is considerably higher than the result from Lauck et al, at 490 K. [49] Kouchi et al. (2020) employed an entirely different method using transmission electron microscopy, which produced a barrier of 350 K, intermediate to the two previously reported values [60].

Some details cannot be physically observed with laboratory methods, but with a detailed microscopic kinetic Monte Carlo model one can directly observe individual molecules and their response to kinetic parameters such as temperature. One measurement that has escaped current methods in terms of chemistry is the location of a diffusant. IR methods as discussed above can provide kinetic details, such as the rate at which something mixes, and even can show coordination of molecules like CO moving from homogeneous to a heterogeneous mixture with water. Kouchi et al. (2020) measured the CO diffusion barrier using transmission electron microscopy, a direct measure of diffusion and found a barrier of 350 K $\pm$ 50 K of CO on ASW.

The lower barrier observed by Lauck et al. may be indicative of the diffusion of CO on a CO surface, due to large volumes of CO entering and coating the pore structure, while the higher experimental barriers may indicate a more water-dominated diffusion barrier for CO. Fitting to a simple diffusion model cannot directly address this question.

Here, we investigate the movement of CO with respect to the underlying, mostly-unchanging, water ice (16 to 23 K) and how that structure impacts the ability of CO to penetrate porous structures in water ices. A model named MIMICK, a kinetic Monte Carlo model, was used to replicate the changes in surface area and confirm our replication of the behavior of water ices. MIMICK provides a unique look into mixed ices as it is off-lattice, which enables true amorphous water ice structures to form while following each individual molecule in time. The use of this method allows the binding and diffusion characteristics of CO to be explicitly traced.

We focus on the direct deposition of water ices followed by carbon monoxide (CO) at various conditions to measure the mixing barrier of CO into H_2O. This barrier has been well-established in the laboratory setting, but it is unknown how this relates to interstellar conditions like those of a dark cloud. Where dark cloud conditions produce ices with more compact structure compared to their laboratory ice counterpart under all temperature conditions tested (10 to 40 K).[20] This finding raises the question of

whether our fundamental understanding of surface science at the microscopic scale is directly applicable to the physically processes occurring in conditions where timescales are greatly reduced, such as dark clouds and even protoplanetary disks.

5.1 Methods

We use *MIMICK* to simulate the laboratory deposition of water onto a cold surface. CO molecules are then deposited on top, and diffusion of those molecules into the structure of the water ice is simulated at various temperatures, in order to broadly approximate the conditions used in specific literature experiments.[63] To analyze the simulation data, a method of calculating the mixing fraction is presented that considers the probability of CO molecules having a polar interaction with nearby H_2O, in order to replicate an infrared spectroscopic measurement of mixing. As well as being analyzed independently, the mixing data are also incorporated into a Fickian diffusion model where the fits produce a diffusion constant. The diffusion constants are then analyzed using an Arrhenius fit to find diffusion barriers.

During the simulation of water and CO deposition, the adsorption (i.e. accretion) process also competes with any surface diffusion or desorption events. A small change is made to the adsorption treatment in the present model. Whereas in previous versions of *MIMICK*, an incoming molecule would follow a straight-line trajectory toward the surface (whose starting point and/or direction would be randomized, depending on the deposition method), the new method attributes a velocity to the molecule (taken randomly from a Maxwellian distribution) and allows the velocity vector to adjust to the potentials that it experiences as it approaches the surface.

5.1.1 Binding characteristics

In the simulations described here, it was necessary to test various pairwise interactions for CO to H_2O and to itself. The interaction between water molecules should be significantly higher due to hydrogen bonding, which provides a starting upper limit. We use the laboratory data for CO desorption from H_2O as a means to test our model. This is done by normalizing the CO desorption to ensure the model and laboratory data is easily comparable and overlaying the profiles. The maximum desorption temperature for the peak between CO between H_2O and CO should match is the leading curve temperature, but this is should be used with caution as this is very sensitive to the abundance of CO within the model and the underlying structure of the amorphous H_2O ice. This is repeated for each pair-wise interaction. The binding of CO to itself was determined using similar methods, but with pure CO ices. Further, when coverages of CO are large an addition peak forms that is indicative of CO interaction with itself. Figure 5.1 shows the resulting early temperature desorption profile with various pair-wise interactions (all in different colors) compared to that found in the laboratory setting (shown in black) [32]. The profiles shown with various colors demonstrate the profile produced for simulation with a different pair-wise interaction for CO and H_2O. The profile with the best match has an interaction of 210 K, this is the value used for the entirety of this paper. The radii

for the grain, H_2O, and CO are shown in table 2. The grain is roughly representative of a carbon atom at 1.6 Å. The size and potentials for the grain are not as important when ices have considerable thickness (>∼1 ML). The size of carbon monoxide was tested using the same methods described in Clements et al. 2018 where CO was deposited and the density was calculated at 20 K. The densities were compared to those from Pipes et al. 1978 which were also taken at 20 K and found to be 0.8 g/cm^3.[71]

Table 5.1: The pair-wise interactions in Kelvin for the species of importance to the models presented here. The interactions to the grain are adequately high to ensure sticking at reasonable temperatures but is not parameterized for a specific surface type.

	Grain	H_2O	CO
H_2O	550	850	210
CO	120	210	120

Table 5.2: Van der Waal radii used for each species in the presented models. The grain radius is based on the size of a carbon atom.

Grain	H_2O	CO
1.6	1.75	1.859

The diffusion of individual molecules can be traced over time, at various temperatures. The temperature as expected dictates kinetic probabilities such as thermal diffusion and the model provides random selection to replicate the stochastic behavior of surface chemistry.

5.1.2 Model setups

The selection process within the model ensures all processes can be in competition with one another. So, for example, diffusion of CO is dominant from 16 to 23 K and CO desorption occurring at higher temperatures. To simplify analysis only diffusion rich temperatures are investigated here. At temperatures 23 K and above desorption becomes significant and will diminish diffusion. The experiments include a warm up stage where the layered CO-H_2O ice was heated at a rate of 1 K min^{-1} and then an isotherm was performed at 1 Kelvin increments from 16 to 23 K. These temperatures are low enough to reduce desorption.

A number of different conditions were used to elucidate the relationship between the initial deposition conditions and the resulting structure in order to achieve the following goals: (i) establish diffusion behavior in various ice environments; and (ii) compare dark-cloud conditions to those used in previous laboratory studies.

We utilize both background deposition (random angle) and uniform angled (0 and 45 degrees) deposition. The data set was also used to ensure ices were comparable to laboratory experiments. Unlike previous work we present results of diffusion on a compact water ice (deposited at 100K). Water is deposited at 10 K (except those for the compact water ice) followed by the deposition of CO. To test our ability to measure mixing we also produced a number of control ices. We co-deposited CO and H_2O with varying concentrations. A deposition rate and temperature of 10^{13} molecules cm^{-2} s^{-1} were used

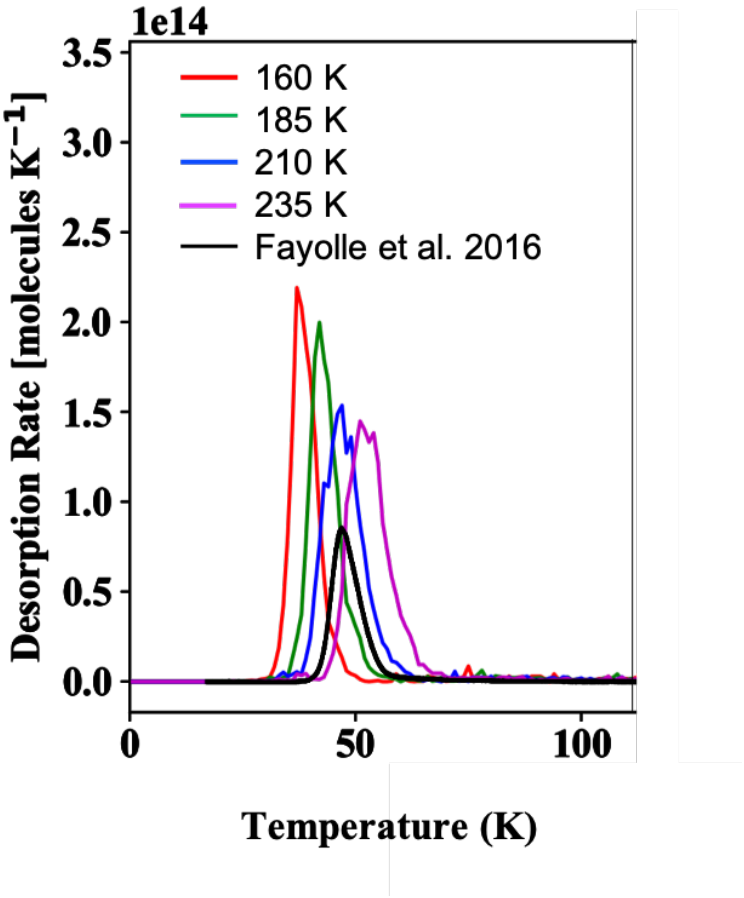

Figure 5.1: Desorption of CO from porous water ice with temperature programmed desorption profile from Fayolle et al. 2016 for reference. The pair-wise interaction of 210 K between CO and H_2O shows the best match.

to replicate the methods used in laboratory experiments. The codeposition of CO and H_2O ensure ideal mixing. The ideal ratio for CO is shown with a black dashed line and the calculated mixing ratio at each time step is shown in light blue. We find our method is more sensitive than infrared spectroscopy as is to be expected. When CO is within either extreme, surrounded by mostly CO or mostly by H2O, laboratory means do not have the sensitivity one would expect from a Monte Carlo model where every molecule location is explicitly defined.

For the isotherm experiments water ices were deposited (thickness of 30 ML) followed by CO (10 ML). To see the definition of a monolayer within this paper please see the definitions section. To tease out the kinetics of the ice a series of isotherms are used. Each ice is heated to a desired temperature and then kept at that temperature for 90 minutes. The change in mixing is observed with time and then fit with a standard method. The top and bottom layers are switched compared to the standard method used in diffusion experiments. Historically, the volatile species has been deposited followed by water. Here, the volatile species is deposited on top of water because the authors wanted to test many water ice structures and ices with CO first are limited to temperatures below the desorption barrier of CO. The physics and mathematics as we will show do not change nor does the Fickian fit implemented. A Fickian fit is used to calculate the barrier

which should be directly relatable to barriers calculated using macro-measurements such as infrared spectroscopy.

For comparison, an ice was produced using interstellar conditions where H, CO, and O were deposited at accretion rates of 4.37E04, 4.489E+03, and 1.642E+04 particles cm^{-2} s^{-1}, respectively. These rates correspond to gas-phase abundances of 3, 0.85, and 2.3 cm-3. The deposition temperature was the same at 10 K. The ice instead of having H_2O directly deposited will form it through the hydrogenation of O. The CO can also react with other species, primarily making CO_2 and CH_2O. Because of the various species present in the ice, an alternative measurement of the compactness was needed. We define a measure of porosity by using a ratio of the volume of the entire ice including pores (sections ice summed over all x and y) and the sum volume of each species volumes defined as $4/3 * pi * r^2$. As defined, the ratio describes how tightly packed the ice is. The control experiments are shown alongside the interstellar ice as a reference point.

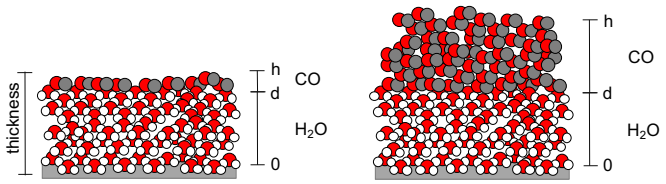

Figure 5.2: Example of two configurations used in the experiments where the water ice is the same thickness and the CO width is variable. The top of the ice or the interface with the vacuum in the laboratory work is indicated by h, and d indicates the interface between CO and H_2O.

5.1.3 Measuring Movement of CO

The movement of CO was an essential component to understand what is physically happening within the ice. To measure movement differences of coordinates were calculated. The explicit location of each individual particle is known at each output and can be traced in time. While the average movement of CO is interesting what was essential to understand was the location of CO with respect to the layer of H_2O that is initially under the CO. The H_2O was divided into five zones where each zone is equal in height and are stacked on top of one-another. CO within in a zone will have a z-coordinate between the zones minimum and maximum. A schematic of the zones is shown on the cartoon ice in figure 5.5.

5.1.4 Quantifying Mixing

One of the most advantageous features of the model is knowing the location of each molecule. This attribute was applied to calculate the mixing at each output/time-step. The changes in the mixing was calculated by counting nearest neighbors using the same method as MIMICK: the number of neighbors is counted within a sphere with a radius of 2.5σ. The radius of CO and H_2O are 1.89 and 1.75 Årespectively. The percentage of mixing is defined here as a ratio of the CO-H_2O interactions compared to all interactions with CO.

The largest challenge of these experiments is to relate our mixing measurements to the macro-observations in the laboratory setting. For instance, infrared spectroscopy will

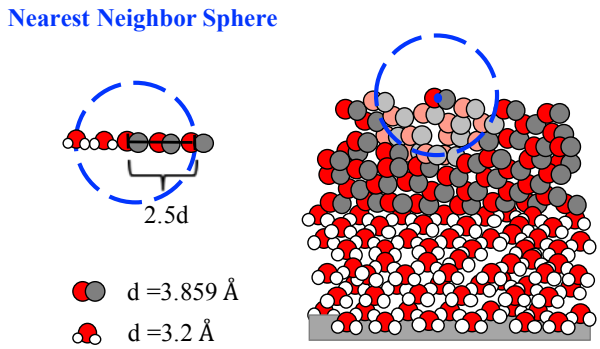

Figure 5.3: A cartoon of a layered ice consisting of H_2O followed by CO. To measure mixing we count nearest neighbors for each particle and use a sphere with a radius of 2.5 times that of the diameter of the particle in question. A CO molecule is highlighted, and the nearest neighbors are shown in a lighter color to demonstrate how the nearest neighbors are counted.

produce a spectrum with features indicating local environments for each species, but as one might imagine features may overlap and band strengths of individual species will change with mixing further complicating the analysis. Band strengths are an observable that are essential to calculate abundances. In making multi-component ice mixtures, it is important to know the amount of each component initially present, and this can be done by careful calibration using the IR band strengths of each individual substance.

We measure the mixing by counting the number of H_2O neighbors for each individual CO molecule. A simple cartoon in figure 5.11 demonstrates how this may look if a slice of the ice is considered. A blue dot is used to show the selected particle and the corresponding nearest neighbor sphere. The number of neighbors or N_i is weighted by a factor P_i, signifying the probability that approximates the interaction of CO to with the available hydrogen bonds. This probability increases with the number of water neighbors because the likelihood of CO aligning and interacting with a hydrogen are greater. Misalignment can occur if CO and H_2O are neighbors but the dangling bond, for example, may be oriented away from the CO. When the probabilities are averaged the resulting ratio can be considered the amount of mixing. We believe this should be comparable to laboratory observables measured from infrared spectroscopy. The mixing ratio will approach unity as most CO molecules are surrounded by H_2O. The probability is calculated by:

$$P_n = P_{n-1} + 0.5 * \frac{1}{2^{n-1}} \tag{5.1}$$

The subscript n denotes the number of neighbors associated with each CO. For example, the first two factors are:

$$\begin{aligned} P_1 &= 0.5 \\ P_2 &= 0.75 \end{aligned} \tag{5.2}$$

The mixing can be thought of as an average over all particles at each time step t.

$$Mix(t)_{tot} = (\sum_{i=0}^{N_{CO}} P_i)/N_{CO} \tag{5.3}$$

To ensure our method of measuring was reasonable, a number of control models were performed. CO and H_2O were co-deposited at various ratios and the mixing was

calculated for each. The use of co-deposition allows an ideal amount of mixing, or a mostly uniform mix throughout the entire ice.

5.1.5 Fickian Fit

To ensure consistency of measurements we adopt a Fickian diffusion model modified from [63, 6, 24]. The general form of Fick's second law describing the mixing with time for a 1-D system is:

$$\frac{\partial c(z,t)}{\partial t} = D(T)\frac{\partial^2 c(z,t)}{\partial z^2} \tag{5.4}$$

where $c(z,t)$ is the concentration of the diffusant CO as a function of time, t, and position, z, and $D(T)$ is the temperature dependent diffusion coefficient. In the layered CO:H_2O system we define $z = 0$ as the substrate height, $z = d$ as the interface height between CO and H_2O layers, and $z = h$ as the vacuum interface. The heights are calculated by the coordinates inherent in the model. Temperatures below the desorption temperature of CO were used to ensure the flux of CO leaving the ice is constant at zero i.e. $\frac{\partial c(z,t)}{\partial t} = 0$ at $z = 0$ and $z = h$. Initially, we assume all CO is in the CO layer and zero everywhere else.

$$f(x) = \begin{cases} C_0, & \text{if } d < z < h \\ 0, & \text{if } 0 < z < d \end{cases}$$

Applying these boundary conditions gives a general solution:

$$N_{mix}(t) = \frac{1}{h}\int_d^h c(z,t)dz \tag{5.5}$$

$$N_{mix}(t) = C_0 * \frac{h-d}{h} + \frac{2}{h} \tag{5.6}$$
$$\sum_{n=1}^{\infty} \frac{C_o h}{n\pi} sin(\frac{n\pi d}{h}) exp\left(-\frac{n^2\pi^2}{h^2}Dt\right)$$

Then, to calculate mixing we integrate over the water layer or from z=0 to z=d and divide by total CO, $1/C_o$*(h-d), which yields N_{mix}:

$$N_{mix}(t) = \frac{d}{h} - \frac{2h}{n^2\pi^2(h-d)}\sum_{n=1}^{\infty} sin^2(\frac{n^2\pi d}{h}) \tag{5.7}$$
$$exp\left(-\frac{n^2\pi^2}{h^2}D(t+t_o)\right)$$

The parameters that are representative of the thickness of the ice and the CO-H_2O interface are h and d, respectively. Each molecule within the model has an x, y, and z coordinate, which can then be used to calculate the height of the total ice and the location of the interface. Parameters h and d are calculated by averaging the z coordinate

Table 5.3: The parameters needed for the Fickian fit h and d, the height of the ice and the height of the interface, respectively, are shown. The density of the bottom ASW layer is also calculated for reference.

Exp #	T_{dep} (K)	h (Å)	d (Å)	Density (g cm^{-3})
Porous	10	192.69	54.06	0.61
Compact	100	150.82	44.35	0.80
0°	10	145.54	42.49	0.80
45°	10	163.70	47.57	0.71

over all x and y values. It is assumed h and d do not change with temperature and our calculations at all desired temperature this approximation was true. The resulting parameters are shown in 5.3. D and t_0 are free parameters that are fit to the experimental mixing fraction of CO over time. We use a python non-linear least squares routine *scipy.optimize.curve_fit* to fit equation 5.8. This can then be converted to coordinates like those from Lauck et al. 2015 where the height of the water ice spans 0 to d. The interface coordinates in terms of Lauck et al. would now be h-d and substituting the coordinates produces the same Fickan fit as seen in equation x in Lauck et al. 2015.

5.1.6 Arrhenius Fitting

$$k = Ae^{\frac{E_a}{RT}} \tag{5.8}$$

where k is the rate of the process and in this case the rate of diffusion or the diffusion constant. A is the pre-exponential factor that can be determined during the fitting, E_a is the energy required to perform the process, or the diffusion barrier, R is a constant and T is the temperature. The expression ratio between the diffusion barrier and the temperature and gas constant represents the fraction of the molecules present in which have energies equal to or in excess of barrier energy at a particular temperature. The equation can then be arranged to:

$$\ln k = \frac{E_a}{RT}\frac{1}{T} + \ln A \tag{5.9}$$

Various diffusion constants can be measured at different temperatures and then plotted and fit using a linear regression. The diffusion barrier and pre-exponential can then be determined from the linear fitting as the slope and intercept.

5.1.7 Definitions

Monolayer (ML) is defined here as a particle count divided by the surface size. For instance, if we have 50 ML that would mean we must have 328,050 particles on top of a surface of 81 x 81 atoms.

Surface area is defined here with a percentage which reflects what percentage of the ice is defined as surface particles, fewer bound neighbors than that of the bulk ice. The surface area does not necessarily have access to the ambient vacuum chamber.

5.2 Results

Here, we show a number of control experiments to demonstrate the reliability of our definition of mixing and discuss the microscopic movement of CO and its resulting macroscopic measurable diffusion barrier within four varying amorphous water conditions.

5.2.1 Control Experiments

Control experiments were run to ensure the factor method to calculate mixing was reasonable. Three experiments were used as controls, where CO and H_2O are co-deposited with varying ratios (1:1, 1:2, and 1:10 CO:H_2O). Given the random nature of the model, CO-deposition is expected to and indeed produces ices that are homogeneous with no apparent segregation. The theoretical mixing can be calculated by: 1 - CO/total ice. For example, the control experiment with a deposition ratio of 1:1 should produce a mix of 0.5 or 50%. Indeed, the mixing calculation discussed in the methods section seems to be a reasonable approximation to represent the amount of mixing at one time step. Another method was used to measure mixing, where the number of CO with any H_2O neighbors was counted. This method overestimated the mixing and thus we adjusted our measurements to include a factor to demonstrate the measurement as more of a gradient than a switch. Figure 5.4 shows the calculated mixing ratio using the factor method for each mix. The theoretical mix is shown with a black dashed line. The mixing ratio fluctuates during the beginning of the deposition experiments and stabilizes when coverages reach about 15 ML. At lower coverages it is likely to have irregular structures where ice is does not uniformly cover the surface.

5.2.2 Movement of CO

The density or porosity, we will see plays a role in the ability for a volatile diffusant to penetrate the deepest layers of an ice. The four deposition methods produced ices with unique water ice structures and porosities and thus will be discussed individually. The change in x, y, and z coordinates are recorded for each experiment, where each experiment corresponds to an individual isotherm. The last time step, t=90 mins, was used as the final locations and the initial time step was taken at t=0 min.

Porous Ice: Exp 1-8

The definition of a porous ice within this paper is water ice deposited at 10 K and utilizing background deposition. These conditions produce an ice with the lowest density of 0.61

g cm^{-3}. Experiments 1 through 8, the porous ice experiments, show the greatest amount of CO movement. The movement in the lateral or the x and y coordinates was minimal but there was clear mobility downward. The average in the lateral direction was less than 10 Åin either direction and the standard deviation was more substantial implying random motion in x and y. However, motion in the z direction did have a larger average movement; he CO on average moved the entire length of the ice or 91.73% of the ice. Again, the average had a large standard deviation associated with it. The final time step at the highest temperature, T=23 K, compared to the initial ice had the largest CO movement of all deposition methods. The large standard deviation for all coordinates demonstrates the randomness of Monte Carlo models. Molecules appear to be sampling a large portion of the ice before sticking to higher potentials, which corresponds here to a water-rich environment.

While the average movement shows CO can span the majority of the water ice, we wanted to see if the particles individually demonstrate some pattern of movement. The H_2O was sectioned into five zones demonstrated in a cartoon in figure 5.5. The water ice is unmoving at these temperatures within the model, which was also demonstrated with laboratory experiments.[49] The percentage of CO in each layer was traced and shown in figure 5.6. Before the heating of the ice the majority of CO 73% began within the water boundaries. POV-Ray images for the initial and final time were produced for the 23 K isotherm for each desorption setup. This particular temperature was chosen as the most diffusion could occur it being the highest temperature studied. The plots on the right show the amount of CO (%) within each zone of unchanging water ice and the stars with the designated zone color indicate the surface area for each layer of H_2O ice. Percentages are used through a scale indicating the location in the ice where 100% corresponds to the initial interface between CO and H_2O and 0 is the substrate. The surface area should give an indication of the maximum amount of CO that can diffuse in each zone. Within the first 5 minutes the majority of CO has moved from z1 to z4. After 20 minutes about 50% of CO is within the lowest zone, z5. The final amount of CO in each zone is slightly greater than the amount of H_2O surface area in both z4 and z5. The surface area here appears to directly relate to the amount of CO capable of being trapped.

POV-Ray images without H_2O were produced to demonstrate the spread of CO for each model and clearly shows the relationships shown in figure 5.6. Further, POV-Ray was also used to follow the diffusion and visualize the path used for diffusion. Figure 5.8 shows the movement of CO during the 23 K isotherm. The images show the ice as it annealed at 23 K. The distribution at t=0 at 23 K shows that CO is relatively well distributed throughout the ice and as the time progresses during the isotherm the majority of CO moves in a downward direction toward the deep pores of water. The times were selected to demonstrate the step-wise movement of CO along the surface of H_2O. At t=0 minutes, the first image starting on the left, few particles are in the pores. As time progresses, left to right, lone CO molecules move from a collection and travel deep in the pore. Individual particle movement is shown with yellow circles and arrows indicate a number of particles moving downward. This demonstrates how the CO moves in a wave-like manner where CO along ridges of CO were the first to diffuse downward followed by all CO surface particles. The particles on the surface and especially in places that are edge-like CO should be neighboring fewer neighbors and hence a smaller diffusion barrier. The topmost layer of CO becomes smoother and compacts, as is seen in pure H_2O ices as well, but at considerably higher temperatures. This smoothing effect continues to the interface between CO and H_2O and the excess CO moves downward sampling

more potentials before becoming stuck in deeper potentials, likely to be nearer to the water layer. The empty H_2O pore structure is thin (less than 4 CO particle widths) and provides an invisible path for CO to spread to deeper portions of the pore. Once a CO crosses the thin pore it appears to lodge itself into a deep pore potential and is unable to diffuse. The yellow circles show when CO moves and lodges itself. The lodged CO then provides a lower the diffusion barrier enough for neighboring CO to gravitate toward. The CO continues to diffuse in this step-like manner until the pores are filled with CO, which is likely vibrating and shifting amongst itself, but the temperature is too low for CO desorption.

The expected mechanism is likely CO diffusing in a step-like manner where CO diffuses and then gets "stuck" in a large potential. The newly stuck CO then slightly reduces the surrounding diffusion barriers which allows the next CO molecule to penetrate deeper into the pores. This process repeats until the entire zone 1 has a thin layer of CO, about 25 minutes into the model. Then, it appears the CO is able to more gradually fill the resulting gaps resulting in most of the CO in the bottom-most, highest porosity region of the water ice.

Compact Ice: Exp 9-16

For experiments 9 through 16, H_2O was deposited at a high temperature (100 K) to ensure the formation of a compact amorphous water ice (cASW) using background deposition. Then, CO was deposited at 10 K. As defined here, compact ices to the knowledge of the authors, have not been used for diffusion studies such as this, because of the tendency to deposit volatile species first followed by water. The water density of cASW, 0.8 g cm^{-3}, is the same as the ice deposited at a normal angle (nASW). While the resulting density of these ices are the same, visually it can be seen that the inner pore network is significantly different, where cASW has very little pore structure but has large smoothed gaps. There appears to be no pore structure in cASW, but the minimization of the potentials yields very round structures.

The motion was monitored using the coordinates within the model and motion in the lateral directions appears to be mostly random. The average was small with a slightly larger standard deviation. At the final temperature there was motion CO in the z direction where the CO was able to penetrate 60% of the total ice. The standard deviation was equal to the length of the entire ice so the motion appears to be quite varied. Desorption at 23 K did occur in significant amounts, where 41% of the original CO has left by t=90 mins. Desorption from compact water ice at this temperature is reasonable if coverages are adequately high, greater than 1 ML. The remaining CO left at this time has filled the gaps within the ice. Ridges form during deposition and provide a lower-barrier path for CO to travel along until reaching a high-potential trap where local water packing increases

When depositing water ices at high temperatures initial islands of ice are created and merge as the islands grow outward. Figure 5.6 validates this as the volatile CO is not limited to top-most layer but is able to fill the gaps between each compact section of ice. Surprisingly, CO can reach the lowest portion of the H2O ice and the majority of CO end in zone 4.

Uniform Angle Experiments: Exp 16-32

The final deposition parameters included uniform angle deposition of all species at 0° and 45° to the surface. The densities of the resulting ices are 0.8 and 0.71 g cm^{-3}, respectively. The CO on average was able to penetrate the top 2± 7% and 7± 18% of the water ice for the ices at 23 K. CO appears to be limited to uppermost layers of the water ice even with high CO coverages (10 ML).

Figure 5.6 demonstrate the movement of CO in a layered CO and H_2O ice where both are deposited at the same angle. Very little changes in the distribution of CO in the water ice. The CO can access further into the ice deposited at 45° but appears to be limited most likely from the water being too compact and the pores are not accessible to the larger species. The amount of CO within the water increases from 51 to 59% for the normal angle ice.

The ices deposited at 45°, which are more porous than the ice deposited at a normal angle, demonstrates more movement of CO. Figure 5.6 and Figure 5.7 show the movement of CO about the water ice. The amount of CO within the H_2O ice increases from 48% to 81%, which is the greatest increase in CO of all models. Additionally, the CO begins to span the bottom 20 to 40% of the ice, but it appears the pores are not readily accessible otherwise there would be more of a spread through the entirety of the ice. The coverages are adequately high enough to promote movement like within the porous ice. This is also demonstrated in figure 5.6 where 50 to 60% of CO, respectively, is in the top 20% of the water ice at the end of the 23 K isotherm and about 10% of the CO spans the rest of the ice.

The behavior described above agrees with previous N_2 adsorption experiments. [29] Dohnalek et al. 2003 showed the uptake of N_2 is dependent on the angle of deposition, where a normal angle is unable to trap CO within its pores and a 45° ice can trap around 5 ML. Likely, the differences in the pore structure allow a greater CO penetration depth which likely increases the chances of trapping at high temperatures. It would be anticipated a more porous ice, utilizing higher deposition angles or background deposition, would allow CO to span more of the H_2O, and indeed we see that in the porous random angle model. The porous ice shows the most CO movement into the lower layers of the water ice.

5.2.3 Fickian and Arrhenius Fitting

To understand the kinetics dictating the processing we observe, we use the Fickian law of diffusion and the work that has since been used in surface astrophysical experiments.[63, 6, 24] The mixing ratio for each isotherm is shown in figure 5.10 where each temperature is shown in a different shade of blue. We show the generated fit from Python's library *scipy.optimize.curve_fit*. Three weights were used to generate fits and hopefully clarify some of the early- and late-time behavior. Two of the fits are shown in figure 5.9 where the black shows an evenly distributed weight, and the dashed blue fit is heavily weighted toward the first 30 minutes of the isotherm. The times selected for the weighting was chosen because of the mixing behavior demonstrated in the left bottom plot, where some of the experiments show a rapid increase in mixing at earlier times and the change in the mixing ratio slows after 30 minutes. This change corresponds to what was described in the CO movement section; the CO rapidly diffuses into the water ice and forms a thin

layer around 30 minutes into the simulation. Then, CO fills the pores, which appears to be a slower process than the lining with CO. The difference in speed can likely be explained by in the barriers before and after CO has formed a thin layer. The thin layer of CO will lower the barrier for the rest of the CO to diffuse, which increases the surface accessible to the CO and likely the time it takes for each individual to find a deep potential. When coverages of CO are greater than the H_2O surface area coverage, CO will fill the accessible pores and then have remaining CO left over stacked upon itself, which within the model cannot mix further without implementing a swapping mechanism.

Utilizing the Fickian fitting described in the methods, the calculated diffusion coefficients increase with temperature from 7.40E^{-17} cm^2 s^{-1} at 16 K to 1.26E^{-14} cm^2 s^{-1} at 23 K for the porous ice produced from background deposition. Diffusion constants for each individual isotherm is shown in table 5.5. The three fits are shown and designated with named subscripts. For the porous ASW it appears diffusion doesn't really turn on until 18 or 19 K. This will be important when the Arrhenius fit is applied because it is a linear fit. It was found that at most times the diffusion constant is larger at earlier times and lower at end times. This ice in particular demonstrates the greatest change in mixing and further, shows the widest range of diffusion constants from 16 to 23 K. Again, the porous ice shows a rapid increase in mixing at earlier times and the change in mixing slows around 30 minutes.CO at this temperature has trapped itself in the deepest water pores and coverages are high so the CO pools on top of itself. As opposed to the control experiments where CO and H_2O are co-deposited the mixing is maximized and does not rely on diffusion. For the layered experiments, it would be anticipated that the theoretical maximum (the ratio of CO to total ice) is unattainable because the water ice is immobile. At low temperatures random angle deposition produces large pores spanning the majority of the ice producing larger accessible surface areas like discussed in 5 and produce the largest barrier of all the models.

A weighted linear regression of the Fickian Law Arrhenius plot (Figure 5.10) yields a diffusion energy barrier of 267 ± 39 K. When eliminating the first two points (16 and 17 K), where diffusion seems limited, the barrier jumps significantly to 373 ± 50 K. Further, the coefficient of determination or R^2 fit improved from 0.89 to 0.93. The error given to each barrier is the error associated with the slope calculated from a best fit using a least-squares method, LINEST. The weighted fits with the eliminated data points have barriers of 352 ± 92 and 471 ± 63 for the 30 and 60 weights, respectively. The barrier for the normal fit, as one might expect, is a rough average of the two barriers. He et al. 2018 calculated the CO diffusion barrier for ices also grown with background deposition and found a barrier of 490 ± 12. This value very much agrees with our weighted barrier of the second part of the curve, which given the rapid speed at which mixing occurs, could imply He et al. measured the late-time mixing bahaviour.

For compact ASW, the rates decrease at higher temperatures, because at these temperatures desorption begins for the compact ice and actively competes with diffusion. The diffusion rates range from 1.51E^{-18} to 8.06E^{-17}, which implies little change. A barrier was calculated for the compact ice and it was found to be 108 ± 69 K with an R-squared value of 0.29. Because of the desorption and the low rate at 10^{-18} cm^2 s^{-1} that occurs at 23 K the data point was removed from the fit and a resulted in a new barrier of 167 ± 72 and a coefficient of determination of 0.52. The barrier being significantly lower is expected. To our knowledge barriers for compact ices have not been tested because typically volatiles are deposited first and limits the deposition temperature the top water layer.

Both barriers associated with the ices deposited with uniform angles (0° and 45°) produce barriers around 210 ± 11 K and an R^2 fit of 0.98. These values seem reasonable as the ices were of limited accessible porosity and fall between the porous and compact ices desposited with background deposition. They both have limited diffusion not because of kinetic limitations but because of the water structure itself. The column-like pores produced are too narrow to allow CO to pass. Lauck et al. produced ices with little to no porosity as they deposited ices at a normal angle. The diffusion barrier they calculated was 158 ± 12.

The resulting barriers are lower than the most recent diffusion barrier from Kouchi et al. 2020 at 350 ± 50 K. [60] The experimental ice was deposited at 55°, which would produce an ice with considerable porosity and could produce pores wide enough to allow CO to access the entirety of the ice. Their resulting barrier of CO on ASW is a more direct measure of the diffusion and is likely more reliable than infrared measurements. While infrared methods are extremely useful, as a tool it does not directly measure surface diffusion, and this may explain the variances from experiment to experiment.

5.3 Astrophysical Implications

In structures such as dark clouds and protoplanetary disks ambient gas will hit grains and stick if temperatures are adequately low. The angle at which incoming particles come in should be random increasing the porosity. It is important to note H_2O is not directly deposited but chemically formed on the grain surface, which will decrease porosity, but as seen from Garrod 2013 ices chemically formed still have significant porosity.

Here we deposit a mixture of H, CO, and O and measure the porosity using a ratio described in the methods. The ratio is defined by the ratio of the total ice volume and the total volume of each species summed together. This value should be 1 when the two values are the same and increase as porosity increases. We see the compact ice does not produce an ideal ratio of 1, but of 1.67. The use of isotropic spheres intrinsically produces empty spaces. Further, as seen in figure 5.6, the compact ice is not perfectly square and contains gaps that will raise the ratio. An additional temperature was run to see if slightly more compact ice could be achieved at a deposition temperature of 120 K. The resulting ratio was 1.49 and a resulting density of 0.8 g/cm^3 Other ices produce ratios significantly higher at 2.18 and 2.12 for the ices deposited at 10 and 35 K. The interstellar ice produced the same ratio as seen in the compact ice of 1.67. Surprisingly, the ice is as compact as ice deposited at 100 K. The diffusion and formation of the ice through hydrogenation and other chemical pathways significantly decrease the porosity. As we have seen from the previous models where H_2O and CO are deposited directly compact ices prevent diffusion and potentially trapping, but this ice does not have this issue. CO is mixed throughout the ice and further will likely not lose CO to the vacuum because the potential of CO should be greater as long as H_2O is present in large quantities.

The ices with laboratory deposition rates are shown in red (porous in light red and compact in dark red). The various ratios of CO to H_2O for the porous ice were codeposited to ensure ideal mixing as discussed in the control section. Ideal behavior where there are no empty spaces would produce an inverted ratio of 1. The compact ice, where packing is closest, has a value of 1.5 due to the spaces still present between particles. The curve in bright red demonstrates the unique behavior when using two species with different

Table 5.4: CO and H_2O desorption experiments grouped by experiment type, together with Fickian diffusion coefficients with all weights discussed (normal, first 30 mins, and last 60 mins).

Exp # Porous Ices	T_{dep} (K) CO:H_2O	Angle (°)	T_{mix} (K)	D_{norm} (cm^2 s^{-1})	D_{w30} (cm^2 s^{-1})	D_{w60} (cm^2 s^{-1})	Δ Mix %
1	10	Ran	16	7.40E-17	8.72E-17	3.82E-17	1.5
2	10	Ran	17	1.40E-16	8.86E-17	3.57E-17	2.6
3	10	Ran	18	1.94E-16	7.21E-17	2.36E-17	3.7
4	10	Ran	19	2.63E-16	1.04E-16	3.17E-17	4.3
5	10	Ran	20	4.34E-16	1.00E-16	6.64E-17	5.8
6	10	Ran	21	1.88E-15	1.77E-16	4.75E-16	15.0
7	10	Ran	22	6.51E-15	2.38E-15	2.11E-15	29.3
8	10	Ran	23	1.26E-14	4.48E-15	4.00E-15	27.2
Compact Ices	CO:H_2O						
9	100	Ran	16	1.51E-18	2.22E-18	1.23E-18	0.7
10	100	Ran	17	8.60E-18	1.03E-17	6.94E-18	2.16
11[a]	100	Ran	18	2.07E-17	2.70E-17	1.70E-17	4.2
12[b]	100	Ran	19	5.21E-17	7.39E-17	3.93E-17	6.6
13	100	Ran	20	7.24E-17	1.01E-16	4.23E-17	8.1
14[a]	100	Ran	21	8.06E-17	1.13E-16	4.32E-17	8.2
15	100	Ran	22	1.26E-17	1.02E-17	9.77E-18	5.7
16	100	Ran	23	1.19E-17	5.06E-17	4.87E-18	3.5
Normal Angle Ices	CO:H_2O						
17	10	0	16	2.59E-18	5.91E-18	1.82E-18	0.09
18	10	0	17	3.30E-18	6.68E-18	2.56E-18	0.11
19	10	0	18	7.62E-18	1.52E-17	5.23E-18	0.25
20	10	0	19	1.52E-17	2.17E-17	7.47E-18	0.33
21	10	0	20	2.26E-17	4.71E-17	1.50E-17	0.73
22	10	0	21	3.98E-17	2.65E-17	3.65E-17	1.21
23	10	0	22	8.11E-17	1.40E-16	5.46E-17	2.21
24	10	0	23	1.17E-16	4.48E-17	4.48E-17	3.05
45 Degrees	CO:H_2O						
25	10	45	16	1.00E-17	1.80E-17	9.09E-18	0.33
26	10	45	17	2.27E-17	4.40E-17	1.63E-17	0.73
27	10	45	18	5.80E-17	1.10E-16	3.67E-17	1.70
28	10	45	19	1.18E-16	2.31E-16	8.37E-17	3.35
29	10	45	20	1.68E-16	4.34E-16	8.91E-17	4.75
30	10	45	21	1.99E-16	5.60E-16	1.14E-16	5.62
31	10	45	22	3.71E-16	5.77E-16	2.95E-16	7.36
32	10	45	23	6.47E-16	1.51E-15	3.70E-16	8.58

Table 5.5: Calculated energy barriers for each experiment with various weighting. Some points were removed from fit to see whether certain temperatures were too low for diffusion.
*Removing data points, a Fickian fit to the initial 30 min, b Fickian fit to the final 60 min

T_{dep} (K)	Angle °	E_{mix} (K)	R^2
10	Ran	267 ± 39	0.89
10	Ran	373 ± 50*	0.97
		237 ± 35 [a]	0.88
		337 ± 37 [b]	0.89
100	Ran	108 ± 69	0.29
100	Ran	167 ± 72*	0.93
		130 ± 66 [a]	0.39
		80 ± 70 [b]	0.18
10	0	210 ± 11	0.98
		212 ± 18 [a]	0.96
		190 ± 13 [b]	0.97
10	45	210 ± 11	0.98
		220 ± 14 [a]	0.98
		194 ± 12 [b]	0.98

particle sizes. Ideal behavior produces the lowest packing, and this can be achieved with homogeneous ices. As ices are further mixed the ratio increases and falls as the introduced species begins to dominate. The interstellar ice has a ratio of 1.65 implying the ice is quite compact. While this provides a promising look into interstellar ices it is important to note the ice consists of more than two species complicating the interpretation. In some regions CO_2 can be more abundant than CO. CO_2 being larger than CO and H_2O, would likely produce larger ratios than the control experiments shown here.

5.4 Conclusions

Diffusion barriers found using experimental methods span 150 to 490 K, where the deposition parameters and analysis are significantly different. The computational barriers found here span a strikingly similar range from 167 to 450 K depending on deposition conditions. Because the model presented here only considers pore-surface diffusion and produces similar diffusion barrier, the mechanism of CO diffusion into water is likely a surface process and not bulk diffusion or swapping.

The ability for the model to measure from exactly t=0 provides insight into the kinetics and how it might change at different stages in the mixing. As stated above, the higher barrier of 450 K was produced using a weighting for the last 60 minutes of the most porous ice, resulting from background deposition.

The degree of porosity under various conditions directly determines the amount of CO that can penetrate the H_2O and thus the associated mixing barrier. Ices deposited at a uniform angle (>45°) produce ices with visible porosity but is mostly inaccessible to the larger molecule CO. Potentially higher angles will be accessible to the CO and would produce higher barriers.

We present several key conclusions from this work below:

1. Pore structure of ices deposited using background deposition are dramatically different than those using uniform-angle deposition

2. Background deposited ices are dramatically more accessible to CO than ices deposited at angles below 45°, defined here by the ability of CO to penetrate deeper portions of water ices given large enough CO coverages

3. CO diffuses into H_2O in a wave-like manner where the first wave of CO covers the surface and the rest fills empty spaces in water pores.

4. The mixing barrier for a porous background deposited ice ∼350 K, higher than the barriers associated with ices deposited with uniform angle

5. The models ability to reproduce experimental results indicate CO diffusion into H_2O is likely a pore-mediated process

6. Interstellar conditions produce ices with compactness comparable to water ices deposited at temperatures as high as 100 K

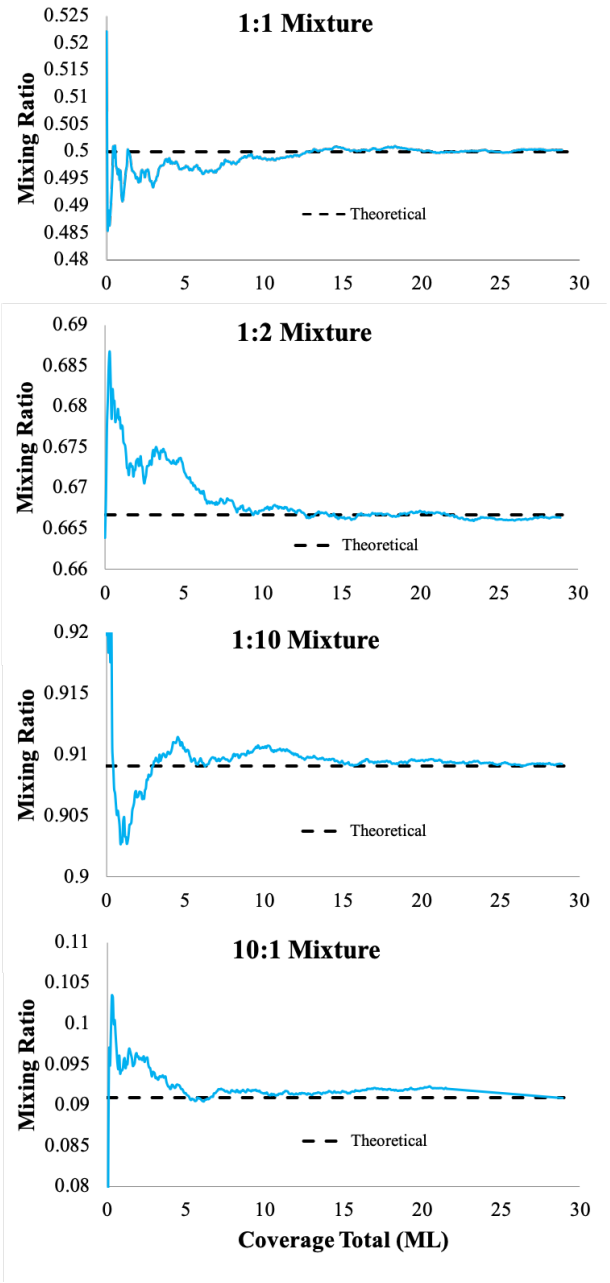

Figure 5.4: Control models where mixed CO:H_2O ices were deposited at 10 K. The ratio of CO was changed from 1:1 to 1:2. The theoretical mixture percentage is shown in black and measured mixture percentages were calculated for each coverage with two methods.

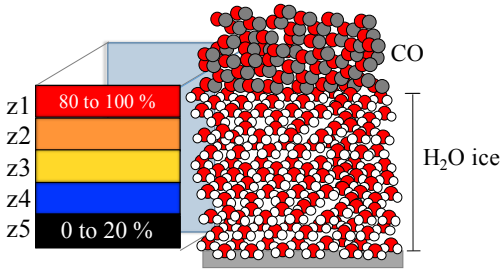

Figure 5.5: A scheme demonstrating how the zones are defined, having equal heights.

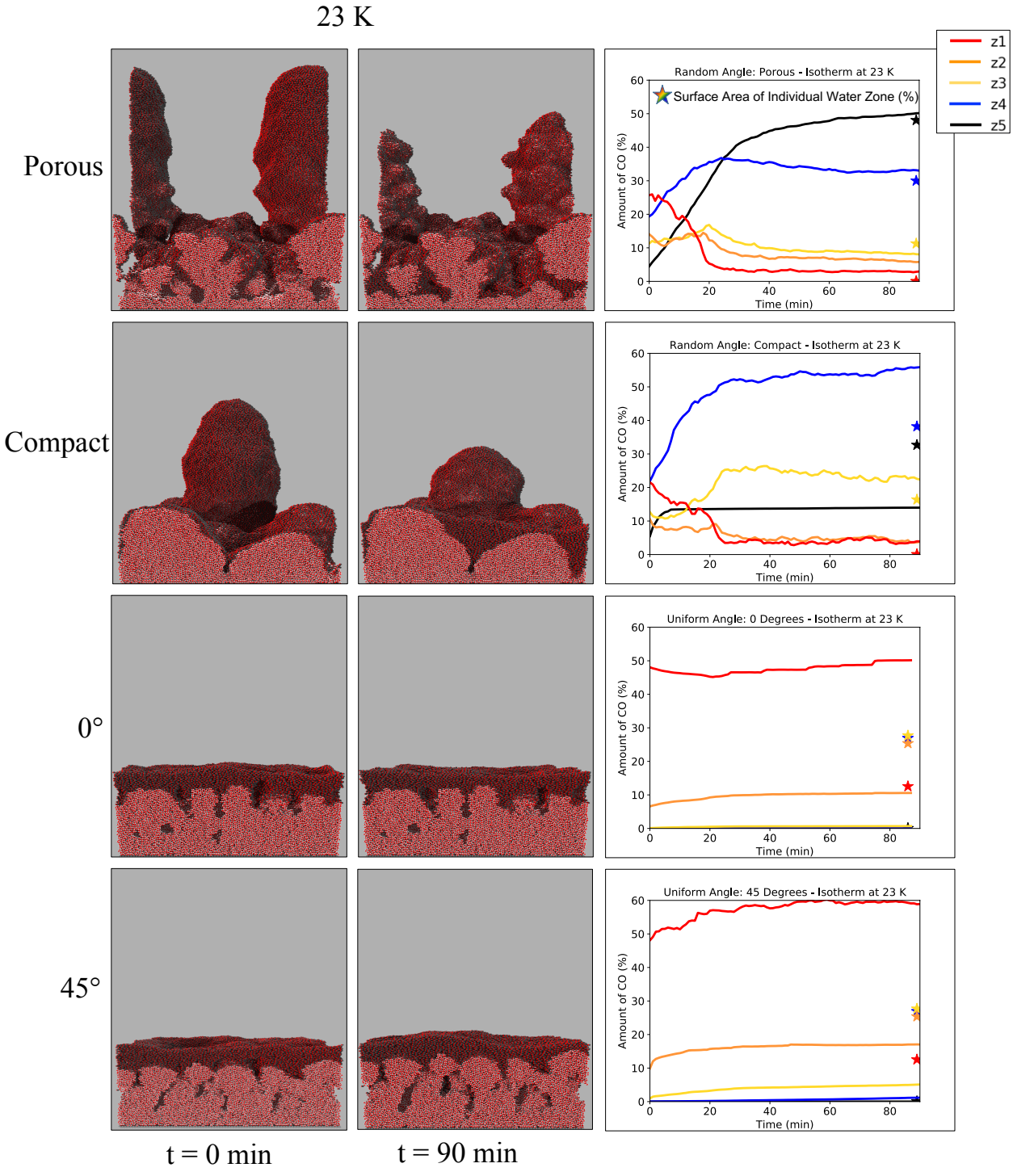

Figure 5.6: POV-Ray images of each ice of the 23 K isotherm at time = 0 and 90 mins. The right plots show the amount of CO within each zone. The stars indicate the surface area for each layer of H_2O ice.

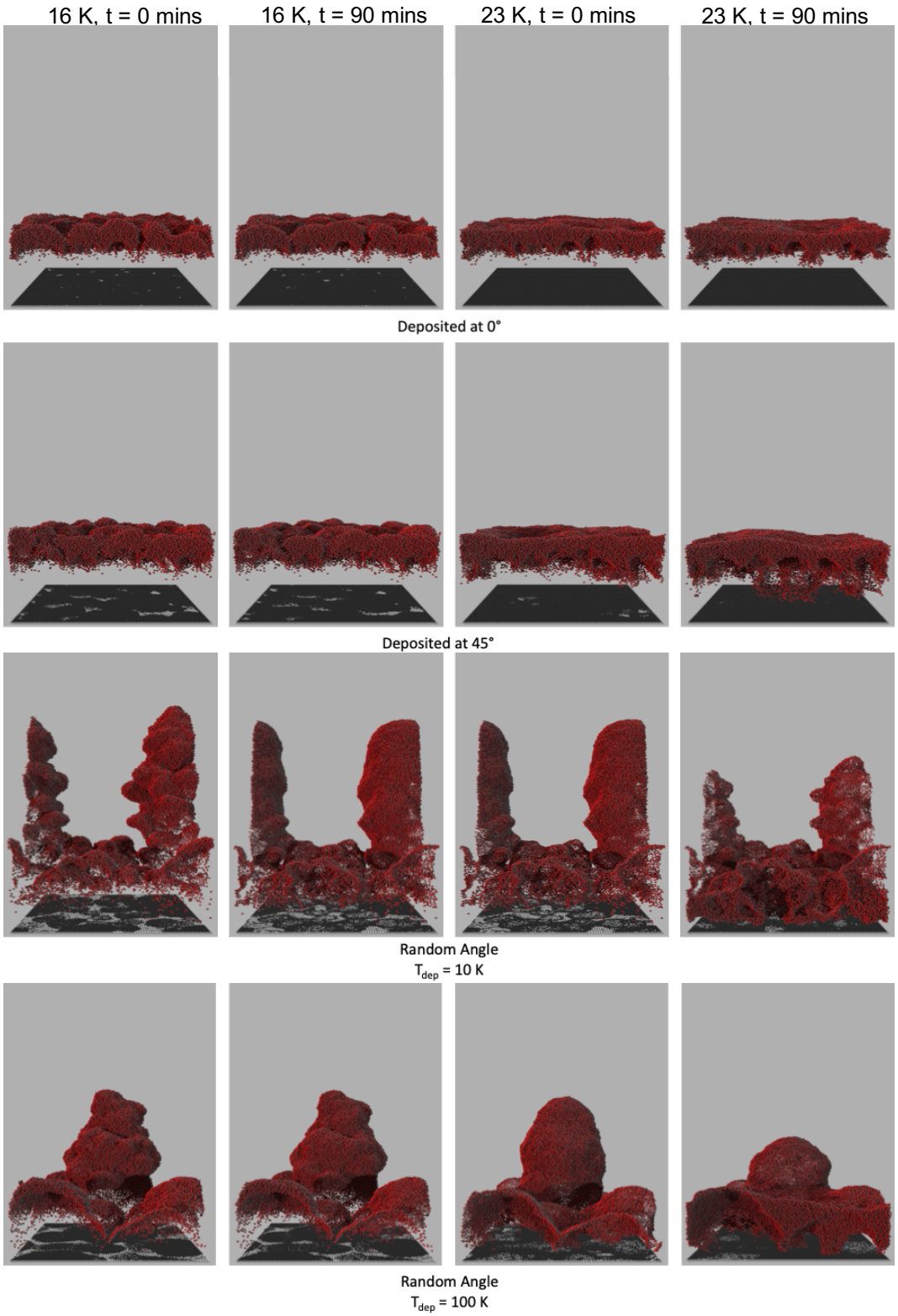

Figure 5.7: Images created using the freeware POV-Ray where only CO is imaged for ices deposited at 0°, 45°, and with background deposition. The compact ice is the only one not deposited at 10 K. The surface is left for reference to the height of the ice. The temperature and time increase from left to right.

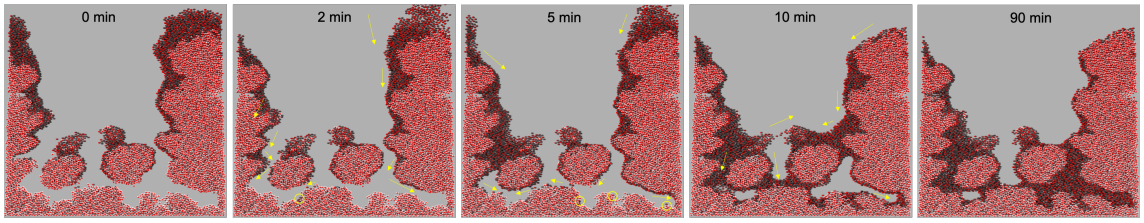

Figure 5.8: Ray-traced images of the isotherm at 23 K, at various times. The yellow circles indicate CO that has migrated to the deep pores of H_2O and arrows show a large number of CO moving in a wave-like manner. These provide a local decrease in the potential, which allows more CO to migrate until at the end time CO has mostly filled the pores.

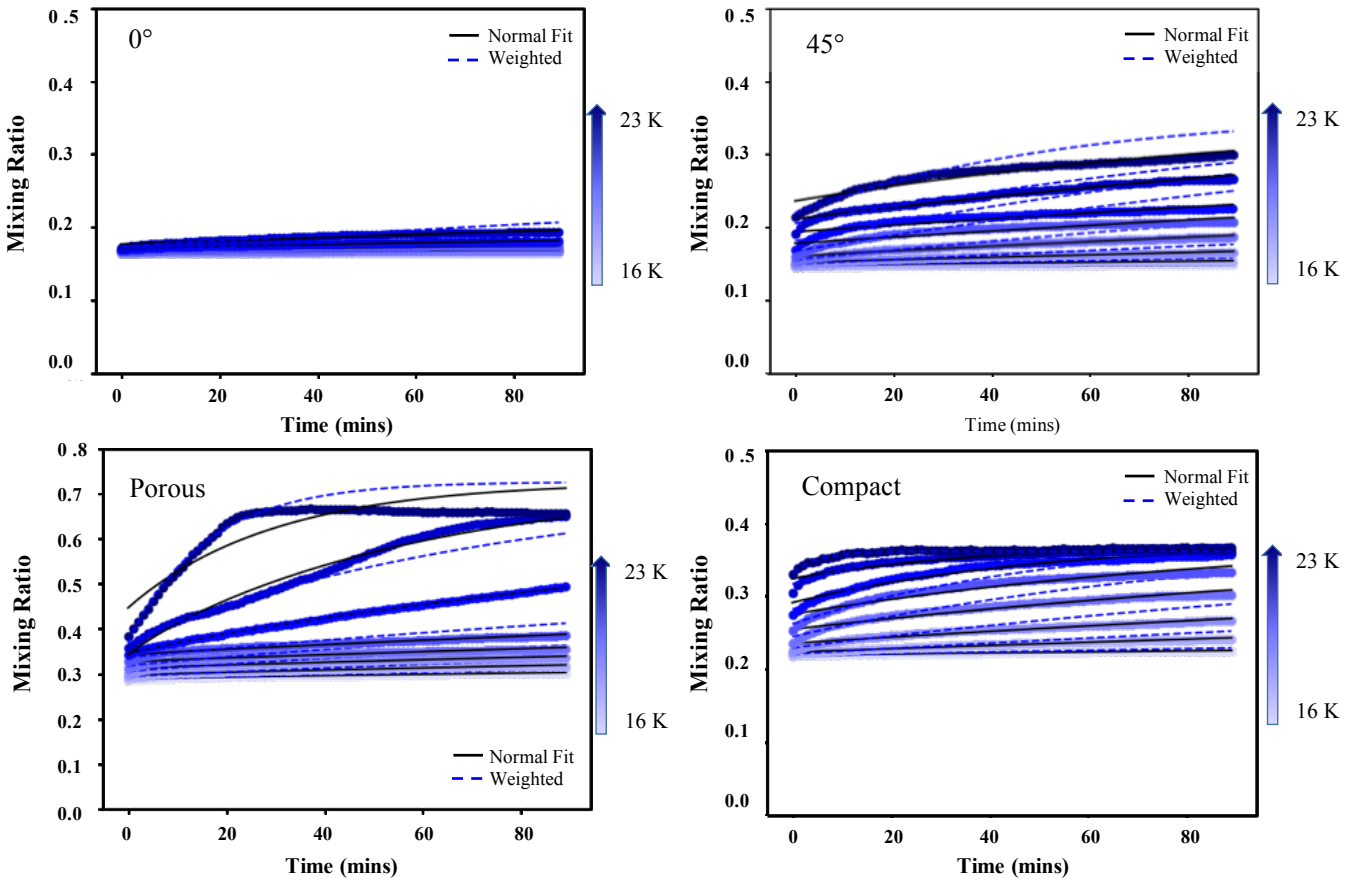

Figure 5.9: Fits of the mixing ratio calculated from equation 5.3 with time. The fits are shown in red and black with the weighted fit being the red dashed line.

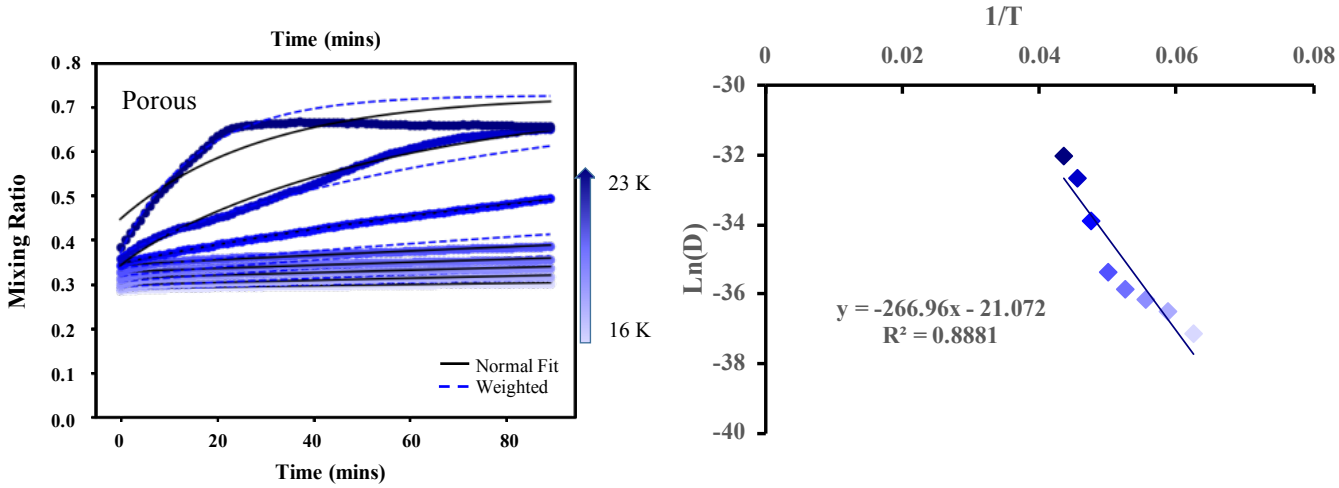

Figure 5.10: The original mixing ratio with fittings and the corresponding Arrhenius fit for the porous ice. Arrhenius fits all look relatively the same with different slopes and associated least squared fitting parameters.

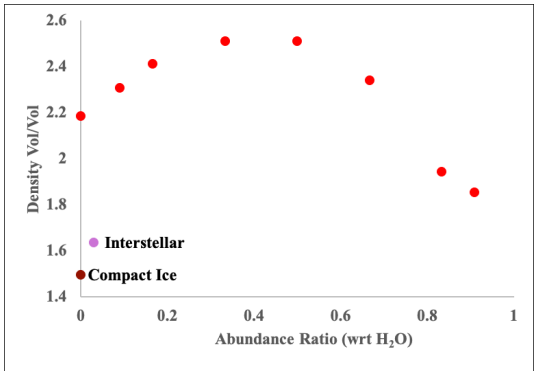

Figure 5.11: Our measure of porosity for various ices. The red shows ices deposited at 10 K with increasing amounts of CO to the right. The compact ice, deposition of 100 K, is shown in dark red. The interstellar ice is shown in pink and is comparable in porosity or packing to the compact ice.

6

Kinetic Monte Carlo modeling of Temperature Programmed desorption experiments

Contents

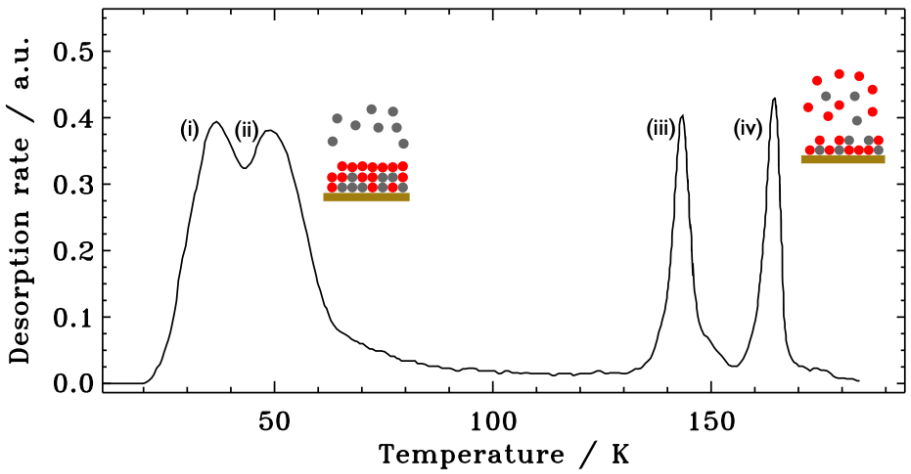

Figure 6.1: Example CO TPD profile from laboratory experiments.[32] The cartoon demonstrates a mixed ice where CO (gray) is desorbing before and then along with H_2O (red). The temperature is shown on the x-axis and CO desorption rate on the y-axis. At regions i and ii, CO is leaving the surface either from a CO-rich environment (i) or a water-rich environment (ii). Stages iii and iv correspond to CO leaving during the rearrangement of water (iii) and sublimates from the surface (iv). This figure was adapted from Fayolle's thesis.

Laboratory experiments have been used extensively to understand ices and their changes upon heating. As discussed in chapter 5 at low temperatures (16 to 23 K) CO diffusion is highly active. For compact ices, 23 K was adequately high to begin desorption as the barrier of CO desorption from a CO-rich environment is lower than CO from a H_2O-rich environment. From temperatures 23 K onward, the competition between diffusion and desorption begins to favor desorption if the CO coverage is larger than the available water surface area, because the CO interaction to itself is lower than to H_2O. The standard of measuring desorption in the laboratory is using mass spectrometry. This may be used in tandem with IR spectroscopy, which provides more details of details such as mixing. These types of experiments are referred to as temperature programmed desorption (tpd) experiments. CO and H_2O are mixed or layered, then heated and desorption is recorded. The different environments of mixed ices vs. layered produces significantly different desorption profiles.[22, 21, 33, 32] The generated CO desorption profiles typically has 3 to 4 peaks which correspond to various binding sites and energies. An example tpd profile is shown in figure 6.1, which was modified from Dr. Edith Fayolle's thesis 2013. At regions i and ii, CO is leaving the surface either from a CO-rich environment (i) or a water-rich environment (ii), respectively. Stages iii and iv correspond to CO leaving during the rearrangement of water (iii) and alongside the sublimation of H_2O from the surface (iv). The CO profile gives insight to the underlying structure of layered ices. For example, the presence of peak i implies saturation of the accessible surface area of H_2O and the shape of peak ii can indicate whether the ice is compact or porous and mixed or layered. The porosity is determined by the deposition parameters as shown by Clements et al. 2018 and discussed in chapter 3. We showed the deposition of ices at interstellar rates produced ices with more compact structure, which we theorize will change the CO desorption features. In addition, we propose using a stellar warm up rate will significantly change the desorption temperature of CO from amorphous water.

Here we utilize the fully updated model and investigate the effects of various parameters including stellar heating rate, deposition order (layered/mixed), and ice thicknesses or coverages. We adapt the model used in Garrod 2013, Clements et al 2018, and Clements et al. in prep to include a non-thermal kinetic relaxation process, heterogeneous molecular sizes, and non-linear accretion trajectories. The use of an off-lattice Monte Carlo model with heterogeneous species sizes allows the application of interstellar and laboratory ices that tend to be amorphous in nature. The use of heterogenous species sizes should account for size-exclusion that may be a fundamental part of trapping or lack thereof. CO and H_2O are treated as spheres with different sizes (1.859 and 1.75, respectively). A fully three-dimensional picture of the ice structure can be traced during thermal processing, which was shown in chapter 5 vital to understand the kinetics of CO diffusion into water ices. Again, the kinetic model is vital to this task due to the nature of the desorption chemistry which is dictated by local temperatures and chemical environments. Here, we show the models ability to accurately replicate laboratory experimental results, which confirms we are accurately treating the chemistry and physical processing. This then allows us to extend the model to prestellar and protoplanetary conditions that provides a unique means to test whether laboratory ices analogs are representative of these astrophysically environments.

The order of the work presented throughout this thesis was very much intentional; structure dictates diffusion. Diffusion and structure control accessibility of volatile species and this will determine the amount of trapping and the overall desorption behavior. The potential for water and structure was first parameterized within the model by Clements et al. (2018), using experimental density data from the literature for amorphous water deposited at various temperatures[12] [29]. Then, the potential for CO-H_2O was tuned for the purposes of studying CO diffusion in various H_2O environments discussed in chapter 5. This chapter is the accumulation of all previous work in the purpose of determining ice behavior in in various star-formation environments and the gas-phase chemistry that results from ice sublimation.

The model can simulate every stage of a TPD experiment, the deposition and subsequent temperature ramp. The stages of simulation include the deposition of the desired ice either being a mixture of CO and H_2O or a layered ice. Then, the ice is heated, and the structural changes are visualized with the changing temperature. We can also trace the gas- and solid-phase abundances and monitor volatile desorption as it is the focus during TPD experiments. We then can generate desorption profiles for analysis and comparison to those produced in laboratory settings. Multiple temperature regimes are considered: CO diffusion (20 to 25 K), then the beginning of desorption of CO from a CO-rich environment ($\sim$25 to 30 K), followed by the desorption of CO from a H_2O-rich environment ($\sim$30 to 60 K). The temperatures for each regime are not exact for every set of experiments because of the varying structures, but this will be discussed in more detail in the discussion. The amount of trapping at temperatures above 60 K are presented here. Volatiles that are trapped will be released during crystallization or desorption of H_2O and released at a much higher temperature changing the gas- and solid-phase abundances and thus the local chemistry. The details above 140 K will not be discusses as these desorption features will likely be unreliable as the model does not account for the crystallization of H_2O. These details include the temperatures when the volcano desorption occurs, or when the volatile species are released due to the restructuring of H_2O, and then the subsequent desorption of H_2O.

6.0.1 Deposition Parameters

Experimental ice thicknesses are typically defined by the number of monolayers (ML). In these models, we define a monolayer as a single sheet of molecules (without pores), that will fit precisely on top of the bare substrate. To achieve similar thickness to laboratory studies (less than 50 ML in this instance) we use varied thickness from 25 to 50 ML. These thicknesses also are relevant for dense cloud ices which are around 100 ML in thickness, on the order of tens of nanometers. In the models presented here, ices are deposited onto the surface at temperatures at 10 and 100 K for porous and compact ices, respectively. For interstellar ices, 10 K is used throughout. Deposition rates are varied from 10^1 to 10^{13} molecules cm^{-2} s^{-1} (equivalent to the number of molecules delivered to the surface at 10^{20} to 10^5 Torr). The standard deposition rate is around 10^{13} molecules cm^{-2} s^{-1} and will be referred to throughout as the standard. Additionally, a deposition rate of 10^6 molecules cm^{-2} s^{-1} was used to replicate conditions pertaining to protoplanetary disks. Two different deposition methods are used to reproduce experimental treatments: (1) deposition angles are randomly generated individually for all molecules, to replicate experimental background deposition, or (2) incoming particles are all deposited at an angle normal to the surface. The primary focus of this work will be ices deposited at a normal angle as we have access to the data and can easily compare them. Heating rates were varied to account for the varied environments explored. Standard laboratory heating rates are $\sim$1 K min^{-1}, which is considerably higher than the rates associated with stellar evolution. Stellar heating rates are assumed to be linear for this work (10 to 200 K in 10^5 yrs).

6.0.2 TPD Profile Measurements

We normalize the CO desorption profiles to ensure the model and laboratory data is easily comparable. This is done by finding the difference in CO abundance between each time step and normalizing by the sum of all desorbed CO. The laboratory data is then scaled to ensure the time step matches those in the models. Then, the data can be overlaid to visualize the differences between both methods.

6.0.3 Dark Cloud and Protoplanetary Disk Models

Models were run with deposition rates for water consistent with dark clouds (10^1 molecules cm^{-2} s^{-1}) and protoplanetary disks (10^1 molecules cm^{-2} s^{-1}). The deposition rate of CO was comparable to that used for H_2O, to ensure reasonable ratios. While it is unlikely that in dark clouds water would be directly deposited on the surface, it is a reasonable practice for protoplanetary disks where gas-phase species may re-accrete onto grains. For the purpose of this paper, we wanted to simplify the ice mantle as much as possible, so we directly deposit water. Future work will be utilized to investigate the differences between directly deposited water and an ice consisting of H and O where water can form.

Once ices were deposited, the warm up was used to act like stellar heating, and the CO desorption profiles can be compared to those in laboratory experiments. The

laboratory data is scaled so the desorption rate has the same temperature time difference as those in the model. The newly defined desorption rate is defined as the percentage of CO leaving at that time step with respect to the total CO that was deposited initially. We used a number of heating rates including the change in temperature from 10 to 200 K for various time periods ranging from 10^4 to 10^6 years. A linear warm up rate was used, because laboratory experiments are heated linearly, and it provides an initial simple model. Future work could entail the use of various temperature profiles to better replicate specific sources.

6.1 Results and Discussion

6.1.1 Pure H_2O Desorption Profile

We test pure water desorption with the previously tested potential from Clements et al. 2018 with the question of whether the model can accurately account for the changes that occur at higher temperatures (>80 K): water compaction and desorption. Water undergoes a phase-change from amorphous to crystalline ice at around 140 K and the model as of now is not equipped to account for the directionality and long-rage interactions required. While we cannot achieve the phase-change, the model may be able to desorb at reasonable temperatures. Fraser et al. 2001 have an excellent figure (figure 1) demonstrating the behavior of H_2O desorption at various coverages.[36] The coverages were 1, 2, 5, 10, 20 and 50 Langmuir. A Langmuir (1 L = 10^{26} torr s^1) was previously used before the use of monolayers became the new standard. The desorption profile is highly dependent on the coverage and will move to higher temperatures at higher coverages. Though, no matter the coverage desorption is always completed by 170 K.

Figure 6.2 shows the coverage-dependent desorption curves from Fraser et al. 2001 and our model in blue. The peak desorption temperature is written in the figure (157 K from Fraser et al. and the model at 175 K). The desorption temperature is well above the endpoint of 170 K, confirming the potential is not sophisticated enough for this temperature regime. Because of this finding we will can only confidently report the trapping of CO above 80 K and not the exact desorption temperatures of peaks generated after 120 K. We expect the profiles above these temperatures are predicted to not match experimental profiles and be unphysical.

6.1.2 Deposited vs Heated Ice

While the structure and density of ices grown at various temperatures was established in chapter 3, the structure of water was still a mystery during the heating process. The annealing of ices is more realistic when considering stellar evolution where an ice is established during the molecular cloud stage and then heated during the advent of gravitation collapse leading to the birth of a star. A comparison of ices that were deposited at a temperature vs an ice that was heated to that same temperature is shown in figure 6.3.

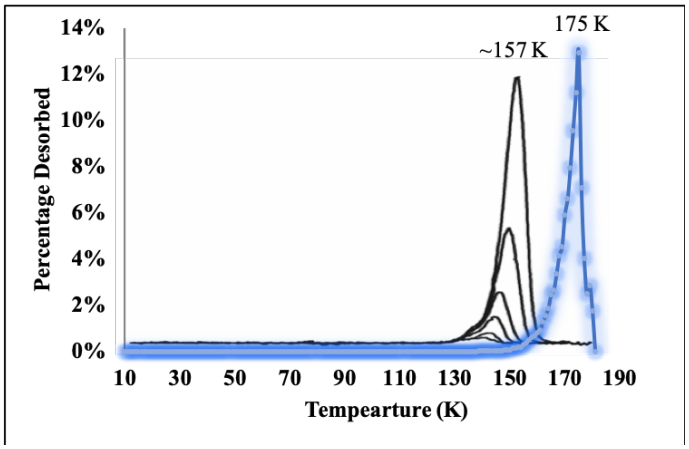

Figure 6.2: Pure water TPD profile at various coverages of 1, 2, 5, 10, 20 and 50 L.[36] The maximum desorption temperatures for both the experiments (black) and simulation (blue) are labeled to clarify the exact temperature for comparison.

The heated ice is shown with black circles and the deposition at the designated temperature is shown with blue triangles. The density was used as the measure of the structure as established previously. The ices begin at about the same density (within the error associated with using a different random seed) and increase in density with an increasing temperature. Deposited ices show a significant increase in the density around 40 K and steadily increase therein. The ice grown at 10 K and linearly heated (1 K min^{-1}) doesn't show an increase in density until ∼80 K. It is important to note, as discussed in chapter 4, the model does not have molecular directionality and will not show changes associated with the alignment of dangling bonds, but our diffusion treatment will not be altered by this. We believe this change occurs at lower temperatures as water can more easily flip itself in its potential, but this is not water diffusing but a new minimization within its pre-existing potential.

The differences demonstrated between the two methods of heating vs depositing at a desired temperature indicate the water ice network is strong, as one would expect from hydrogen bonding. The ices deposited at higher temperatures, because of the low binding to the surface, require water to clump together to ensure sticking; the water clump then grows outward with a compact structure. The pores present in an ice deposited at 10 K are numerous and appear to be eliminated through the accumulation of pores into a few larger pores. This is demonstrated in figure 6.4 where a porous ice is shown at 100, 120, 130, and 140 K. The crystallization of water ice is known to crystallize around 140 K which no images above these temperatures are shown as they are unphysical. The accumulation and merging of pores were also demonstrated from Cazaux et al. 2015 where they use an on-lattice Monte Carlo model. [16] As discussed in Cazaux et al. the accumulation of pores could promote chemical reactions of species trapped in pores. He et al. 2019 also discuss that ASW annealed to 60+ K can no longer trap CO molecules from the gas phase indicating that the remaining pores close off and form pockets. The last panel in figure 6.4 shows enclosed pores or pocket.

Unfortunately, interstellar ices are far more complicated than either pure water or CO and H_2O mixed ices, which would not only alter the chemistry but the structure of ices. For example, a mixed ice of CO and H_2O would show similar characteristic as figure 6.3, but depending on the amount of CO, the decrease in density would occur sooner as the potentials would be weaker. Further, interstellar rates heating rates would

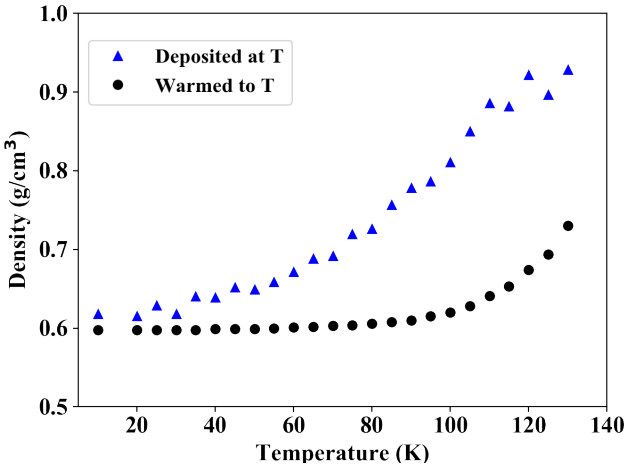

Figure 6.3: Comparison of densities of an ice deposited at 10 K and heated at a linear rate of 1 K min^{-1} and ices deposited at various temperatures. Both were deposited with the typical laboratory deposition rate of 10^{13} molecules cm^{-2} s^{-1}.

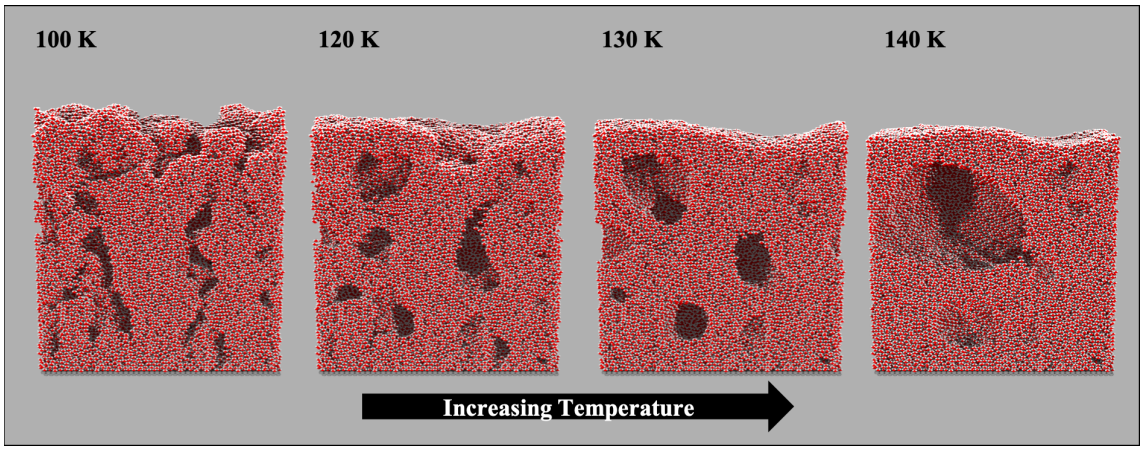

Figure 6.4: POV-Ray images of a water ice that was heated to 140 K. The temperatures selected demonstrate the accumulation of the pores into fewer larger pores.

be dramatically smaller than 1 K min−1. The next few sections will demonstrate what these changing conditions will do using laboratory conditions and then finally what might be occurring in interstellar regions.

6.1.3 Mixed Ices

A mixed ice was deposited with a CO abundance of 5% with respect to H_2O using background deposition at 10 K. The approximate final thickness was 50 ML. Once the ice thickness was achieved, the ice was heated at the standard laboratory rate of 1 K min^{-1}. The desorption profile is shown in the top panel of figure 6.5. The y-axis is the amount of CO desorption occurring at the corresponding temperature with respect to the total amount of CO that was initially deposited. The laboratory results (shown in black) has been scaled to ensure the desorption time step is the same as was used in each

model. The maximum desorption temperature for the first peak was around 48 K with a barrier of 1963 K. The average desorption barrier for every individual molecule at each time step is calculated for the purposes of determining the order of events within the model's algorithm. The desorption peak begins at 40 K and has an extended tail that drops around 80 K. The extended desorption peak demonstrates the changing binding behavior likely from the changing concentration of CO within the mixture. The barriers for the beginning and ending desorption temperatures (40 and 80 K) were found to be 1837 and 2114 K, respectively. The end of the tail can be distinguished as CO desorption drops significantly. Then, significant desorption begins again around 90 K.

The location of the beginning and end of the desorption peak matches well with the laboratory profile shown in black in figure 6.5. The data was taken from Fayolle et al. 2011.[33] The laboratory experiment consisted of a mixed ice with 10% CO with respect to H_2O. The desorption peak begins at a slightly lower temperature of 38 K and goes to zero ∼85 K. This slight difference in temperature for the first desorption peak is reasonable because of the differences in coverages. Figure 6.6 demonstrates how larger coverages will shift the CO desorption profile to lower temperatures. This model demonstrates this with a porous ice, but this pattern is present amongst all setups. Lower coverages ensure CO finds the highest potentials in the water ice before desorption, shifting the binding energy and desorption temperature to higher values. Images of these ices are not shown as they look like a pure water ice that have been heated.

The potentials for the mixed ice are significantly higher than those discussed in the layered ice, the next two sections, which is to be expected given its desorption profile (starting at a higher temperature). Further, the desorption profile has an extended range implying a large variant in binding character. CO on the surface can desorb in the normal manner but a higher temperature as it is pre-mixed. Then, CO accessible to the vacuum but slightly buried desorbs. The first desorption peaks accounts for half of the initial CO in both the model and the laboratory data. This finding confirms the findings of chapter 4: pores are connected to the vacuum–ice interface and are accessible for volatiles adsorption/desorption.

The middle panel shows the binding energy as the ice is heated and the potentials at the beginning and end of the first desorption peak are indicated with light blue lines. The same lines are shown in the bottom panel where the coverage and the potential are plotted. The potential changes with temperature at first likely from rearranging (20 to 37 K). Then, desorption of CO begins, and the potentials increase, again indicating various binding behavior, until it becomes fairly steady.

The last panel shows the coverage of CO (inverse trend of temperature) and the average CO potential. Again, the blue lines indicate the where the beginning and end of desorption profile occur. The coverage begins with 2.4 ML of CO and begins to drop after reaching ∼38 K. The coverage curve was scaled to account for the differences in size by a factor related to the ratio between the size of the CO and the surface particle size.

The initial amount of CO corresponded to ∼2.4 ML and 1.6 ML or 69% was retained above temperatures of 80 K or more. The experiment shown in black in the top panel of figure 6.5 consisted of a mixed ice with a CO to H_2O ratio of 1:10. The amount trapped within the experiment was 47%, but this cannot be directly related as the ices had different thicknesses (25 ML vs 50 ML in the simulated ice). Further, the amount of trapping depends on the amount of CO mixed in the ice initially (more CO produces less strong binding sites and less trapping) and the thickness of the ice.

Mixed ices when relating to interstellar conditions are likely the most relevant, but a

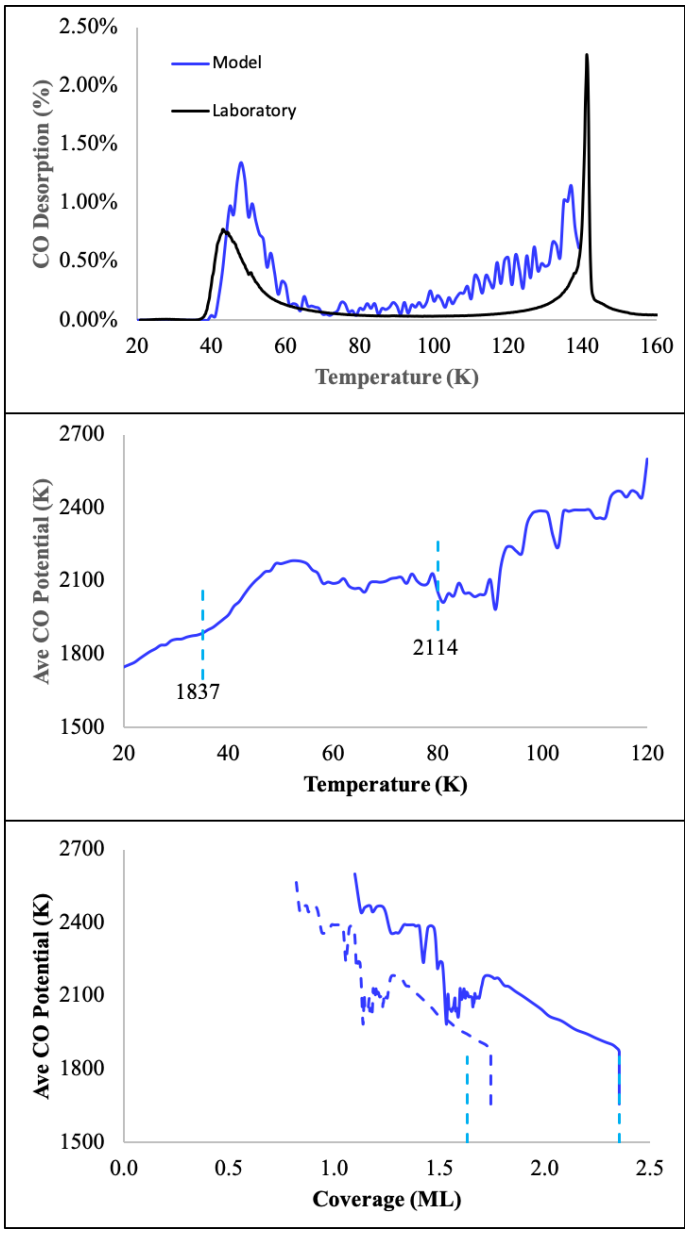

Figure 6.5: **Top**) The simulated tpd profile is shown in blue. The CO abundance was the 5% CO wrt H_2O. The total ice thickness was about 50 ML. The black profile is from the laboratory experiments with a ratio of 1:10 CO:H_2O. [33] The profiles were generated by taking the ratio of CO that left at that time step over the initial amount deposited at the beginning of the experiment. **Middle**) The average CO potential at all temperatures. The light blue lines indicate the beginning and end of the desorption peak. **Bottom**) The coverage of CO and the corresponding average potential (K). The blue vertical lines indicate the beginning and end of the desorption peak. The original coverage is shown with a solid blue line and the scaled with a dashed line. The scaling factor is defined as the ratio between the size of CO and the size of the atoms of the surface.

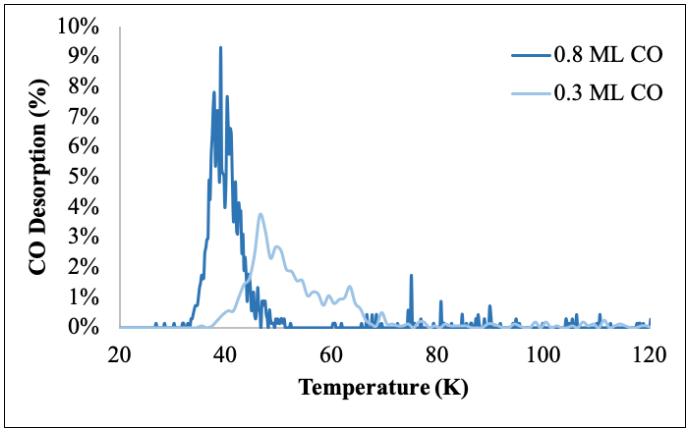

Figure 6.6: A figure demonstrating the relationship between the coverage of CO and the desorption temperature. Smaller coverages access larger potentials and will desorb at higher temperatures. If coverages are larger than the available surface area another peak will emerge that corresponds to the interaction with CO to itself.

series of other simulations were run to test the accuracy of the model when comparing to laboratory conditions. The next sections include layered ices. Layered ices are not entirely unreasonable when considering ices that are re-accreted from the gas phase. For example, if grains experience movement within the mid-plane of a protoplanetary disk it can experience any number of snowlines. Water desorption occurs at a much higher temperature than CO and would first accumulate onto the grain. As surrounding temperatures decrease during grain movement, the CO snowline could follow that of water. This is an overly simplistic view as there are many more species in the gas-phase but layered structures are not entirely unrealistic and should be considered.

Layered CO and H_2O Desorption Profiles

Ice were deposited using normal angle to the surface, or an angle perpendicular to the surface, at 10 K and 100 K with laboratory deposition rates. The angle used for deposition is of great importance as it will dictate porosity and as stated throughout this work porosity greatly affects diffusion, desorption, and trapping. Water was deposited until a thickness of 50 ML was achieved. CO was layered on top at 12 ML, to ensure the H_2O surface area was saturated.

A normal porous was directly compared to a laboratory TPD profile shown in black in the top panel of figure 6.7. [32] The other panels show the average potential of CO with temperature and coverage. Both plots indicate barriers are more complicated than a single value, which tends to be reported in experiments and used in simplistic astrochemical models. The middle panel demonstrates the potentials in K for the beginning and end of each desorption peak (first peak is shown with light blue and second in dark blue). They are placed at the corresponding temperatures. The last panel demonstrates the relationship of the coverage and the potential with the same dashed orange lines. The coverages were calculated by first dividing the total number of molecules by the surface area of the bare surface. We also scale the coverage by a ratio of the size of CO and the surface particle size as their different sizes will dictate how efficient the packing will be. The desorption barrier calculated from Fayolle et al. is shown with a black cross (coverage of 0.7 ML and 1575 K barrier). The calculation to find the barrier involves the use of Polyani-Wigner equation, which at times may simplify the kinetics. The barriers

calculated from the model are defined by each molecule's local environment and will reflect characteristics like changing CO concentrations.

The blue lines are difficult to distinguish because the first and second peak have the same ending and beginning coverages. The dip at 3.4 ML is the turnover between the two regimes: H_2O- and CO-rich saturation. This is confirmed by the surface area of H_2O ice which was found to be 4.02 ML. Because CO is larger than H_2O it will take fewer particles to fill the surface. The ratio between the coverages at 0.85 is roughly equal to the ratio between the particle sizes squared (to account for the dimensionality). Then the potential steadily decreases as the pores are filled with CO topped on top of itself. The last dip at 12.2 ML then can only correspond to CO growing beyond the water ice, the CO-rich environment. When coverages of CO are larger than the available H_2O surface area, CO-CO interactions will begin to dominate and result in the desorption peak beginning around 25 K. When coverages are increased past this point the profile will grow toward the CO-H_2O peak. This is clearly demonstrated in figure 2 from Fayolle et al. 2016. [32]

Images were created using the free-ware POV-Ray to visualize the physical changes occurring in the ice. The temperatures were chosen to match temperatures of interest (the temperatures corresponding to the beginning and end of the desorption peaks). Imaging of the entire ice from 10 to 100 K for the porous ice is shown in figure 6.8. Only CO was imaged in figure 6.9 to demonstrate location of the CO amongst all of the H_2O. The temperatures from left to right are 10, 25, 35, 65 and 100 K. At 10 K, the initial layered ice with CO (dark gray and red) and H_2O (red and white) is shown. At 25 K, the some of the CO has percolated into pores of H_2O and the topmost layers have started desorbing. The middle image, at 35 K, shows the CO has either desorbed from the top of itself or diffused into the porous water layer. By 65 K more CO has desorbed from the higher potential of water. Water has begun diffusing and trapped $\sim$ 0.1 ML of CO (1% of the deposited amount). In the laboratory experiment significantly more of the deposited CO was trapped at 69%, but significantly less CO was deposited initially. If we instead use coverage, we trapped $\sim$0.13 ML and the remaining coverage in the experiments is 0.5 ML. This is reasonable agreement when considering the errors associated with this measurement. The model successfully replicated the temperature-dependent characteristics observed in experiments, including the diffusion and trapping of CO into H_2O pores, desorption of CO at temperatures below 60K, and the diffusion of H_2O leading to the compaction of the ice.

A normal compact ice was also directly compared to the same dataset. The compact ice was deposited at 100 K with laboratory deposition rates. The coverages were the same as above, 50 and 12 ML for H_2O and CO, respectively. To reiterate, this was done to ensure saturation of the water because the definition of a true monolayer is not well established. The same analysis was performed as shown in figure 6.10. Similar behavior is shown where the potentials increase with temperature as CO is lost and solely interacts with H_2O. The blue lines indicate desorption peaks for first a CO-rich environment (light blue) and then followed by a water rich environment (dark blue). Temperatures above 60 K are not shown because essentially no CO was trapped at 0.01%. The laboratory data shows no entrapment of CO with these conditions. In the bottom panel, the surface area of the compact H_2O appears around 1.4 ML, where the CO potential begins to increase more rapidly. The surface area calculated directly was found to be 1.62 ML. Again, this discrepancy corresponds to the size differences within the model.

The last topic that will be discussed is utilizing the model with conditions analogous

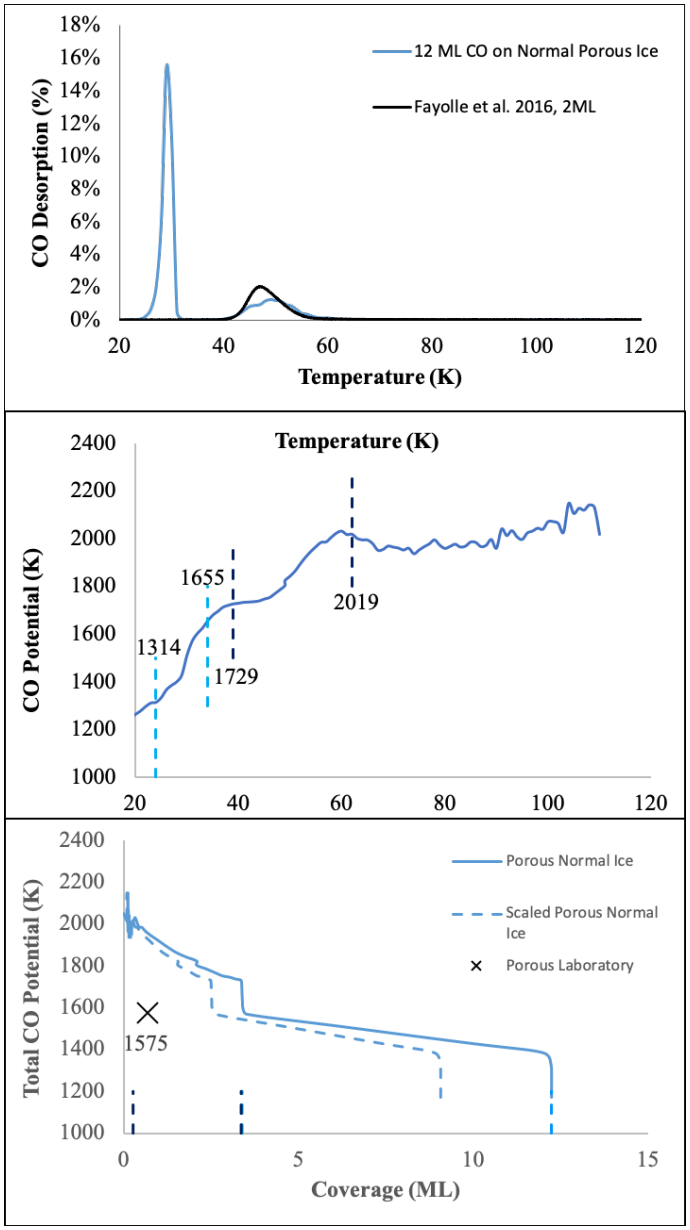

Figure 6.7: **Top**) The simulated tpd profile from the model in blue where 12 ML of CO were deposited on 50 ML of H_2O. All molecules were deposited at a normal angle at 10 K to match the laboratory methods. The black profile is from the laboratory with coverages of 0.8 and 50 ML for CO and H_2O, respectively. **Middle**) The average CO potential at all temperatures. The light and dark blue vertical lines indicate the beginning and end of the two desorption peaks with the light being the lower temperature peak (starting around ∼25 K). **Bottom**) The coverage of CO and its corresponding average potential (K). Again, the blue vertical lines indicate the beginning and end of the desorption peaks. The coverage dependent potential is shown with a blue dashed and solid line. The dashed line was scaled by the ratio between the size of the particle and the size of each binding site. The solid line is the ratio between number of surface particles and the size of the surface. The x indicates the coverage and potential observed in Fayolle et al. 2016.

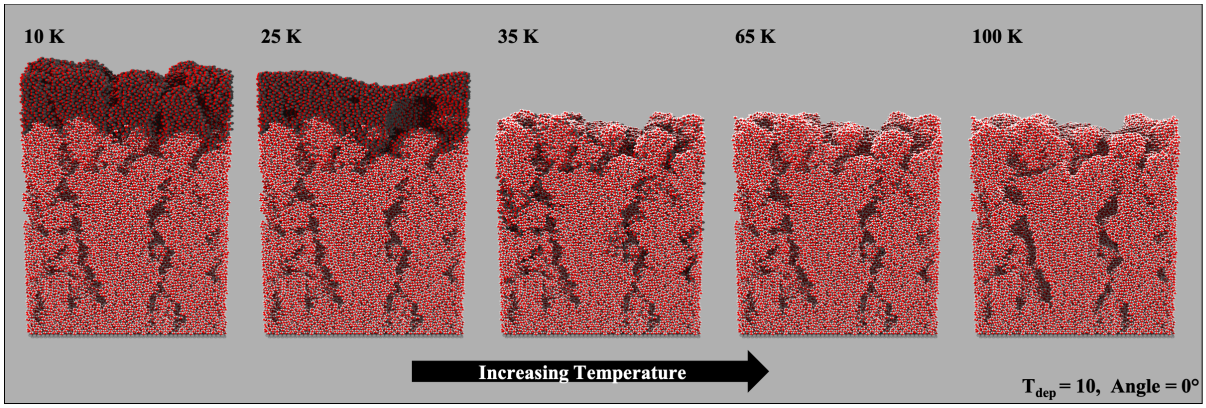

Figure 6.8: POV-Ray generated images of a layered CO and H_2O ice and how the structure changes with temperature. At 10 K the original layered ice is shown. At 35 K the CO has diffused into the pores of the H_2O ice and by the last image the H_2O has begun collapsing.

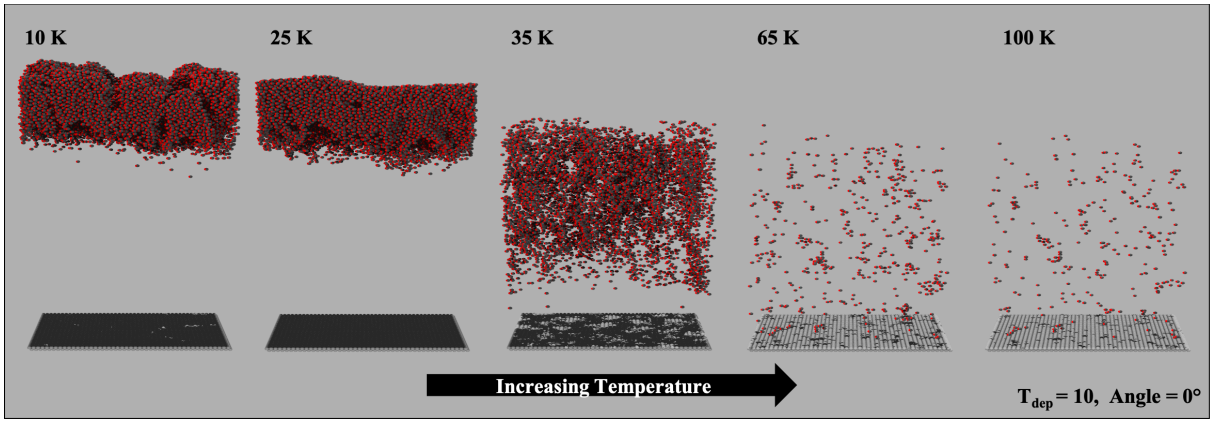

Figure 6.9: POV-Ray generated images of a layered CO and H_2O ice where only the CO is shown.

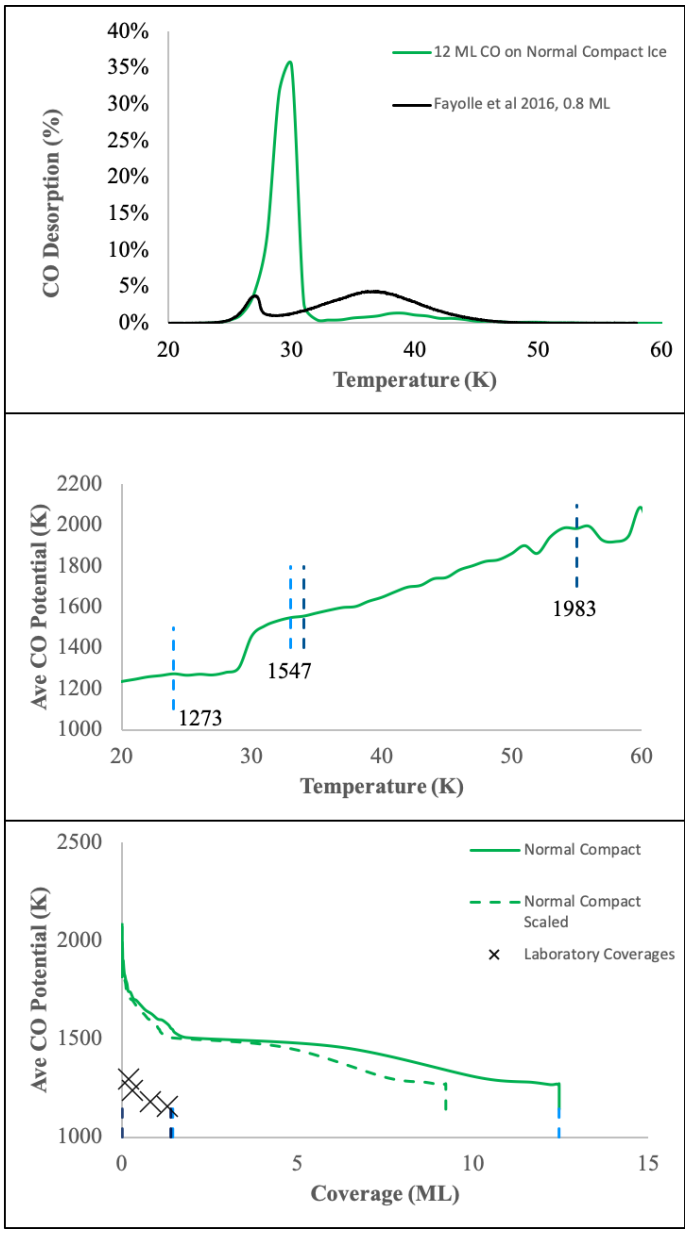

Figure 6.10: **Top**)TPD profile for 12 ML of CO on top of a compact ice (T_{dep} = 100 K) at a normal angle. The amount of trapping above 60 K is negligible. The peak corresponding to the binding of CO in a CO-rich environment occurs at the lowest temperature. As in the previous figure, the coverage is significantly larger than those of the laboratory example.[32] The coverages for the model were 12 and 50 ML for CO and H2O, respectively. The experimental data had coverages of 0.8 and 50 ML. **Middle**) Shows the change in potential with the changing environment caused by the increasing temperature. The light blue lines indicate the first desorption peak indicating the binding to a CO-rich environment. The dark blue lines indicate the desorption from a water-rich environment. **Bottom**) Coverages and their corresponding potential produced using laboratory techniques are shown with black xs. We show the model's coverage with and without scaling and their corresponding potential.

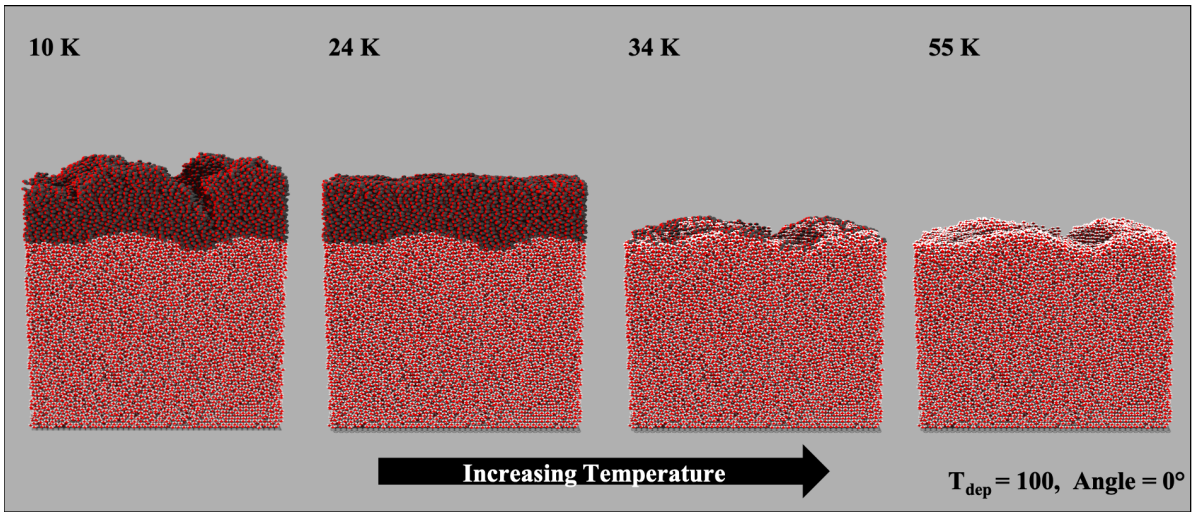

Figure 6.11: POV-Ray generated images of the ice at various temperatures during the warming phase. The first image on the left is before heating began. At 24 K the CO desorption has started. By 34 K very little of the CO is left and what remains is strongly bound to the unchanging water.

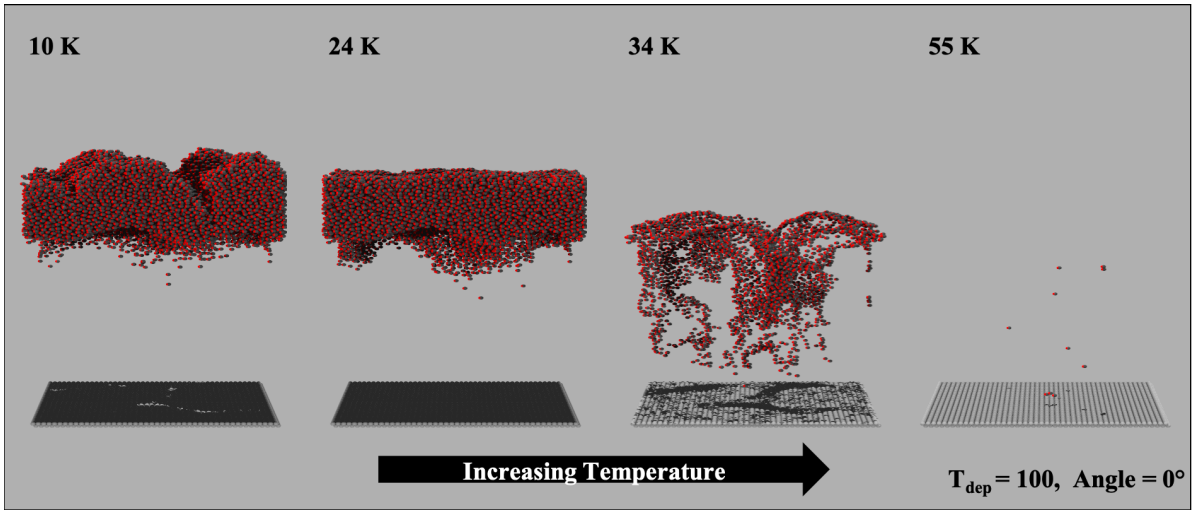

Figure 6.12: POV-Ray images of the warming (increasing temperatures left to right) of the compact ice where only CO is shown.

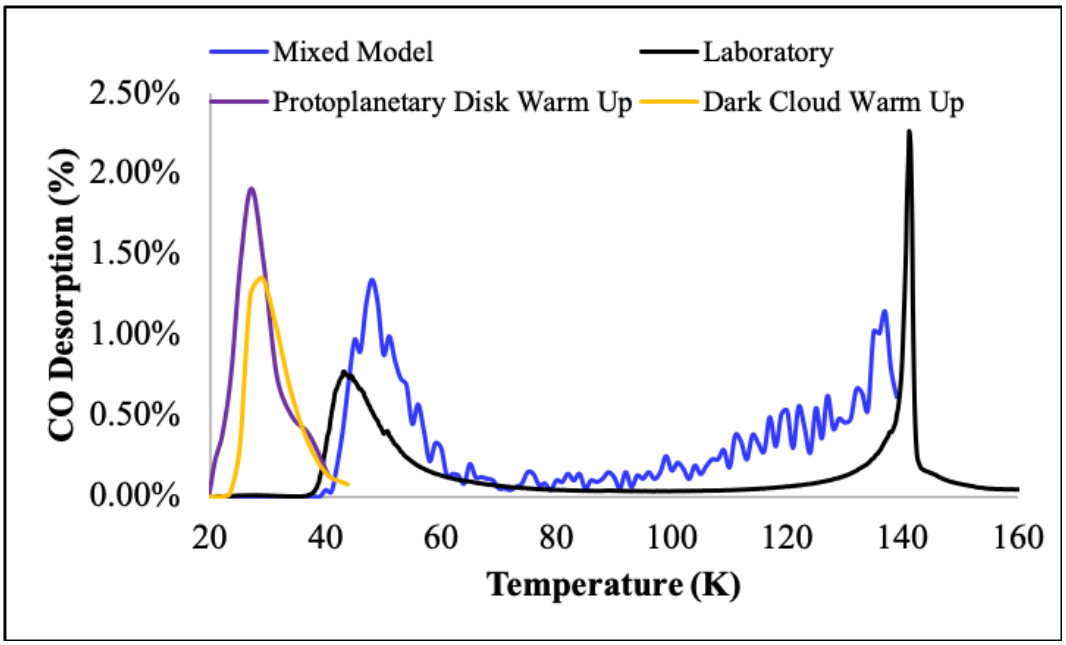

Figure 6.13: TPD profiles of the original mixed ice in blue and the mixed ice experiment in black. The disk is shown in purple and has the earliest desorption temperature. The ISM desorption profile is shown in yellow and follows right after the disk. The average desorption temperatures were found to be 27 and 29 K.

to the interstellar medium and protoplanetary disks.

Interstellar and Protoplanetary Disk Conditions

Mixed ices are shown here, but a number of models were produced using layered ices. CO and H_2O were codeposited at 10 K. The deposition rates of water were $5E^6$ molecules cm^{-3} for higher gas-phase densities like protoplanetary disks and $5E^1$ molecules cm^{-3} for molecular cloud. CO was deposited at a rate 25% of water to ensure a reasonable ratio of H_2O to CO. These rates were established in Clements et al. 2018, which is summarized in chapter 3.

The TPD profiles for both conditions are shown in figure 6.13. The laboratory and model profile for the mixed ice described above are shown for clarity. The heating rates used for the both conditions were comparable around $2E^{-4}$ $year^{-1}$. This was calculated using a simple calculation where the difference between the beginning and end temperatures (10 and 200 K) was divided by the time scale. In this case it was 10^5 years. Unfortunately, these simulations are quite limited because of the time requirement. For instance, when diffusion and desorption become efficient, which occurs at earlier times, it can be as much as a month between outputs ($\sim$ 2 K during the warm up). This has proven to be quite limiting in this work. Fortunately, the time progression that have been achieved in the simulations have been informative.

Figure 6.13 indicates the desorption process begins at a lower temperature for both conditions. The desorption temperature for the disk was around 27 K and slightly higher for the interstellar medium at 29 K. Because this profile is of a mixed ice with mostly H_2O, this desorption feature corresponds to CO leaving a water rich environment The feature in the simulation and in the laboratory (shown in blue and black, respectively) occurs at a higher temperature $\sim$46 K. As found in Clements et al 2018, the densities at

10 K does not greatly alter the density so this is not a result from the structure, but of the heating timescale (1 K min^{-1} used in the lab compared to 3.61492E^{-9} K min^{-1}). Both conditions were heated with the same heating rate and likely the difference in desorption temperature are from the randomness within the model.

The potentials were also observed for comparison. The average potential were 1754 K and 1777 K for the disk and ISM, respectively. This matches relatively well to the potentials at temperatures from 10 to 30 K seen in the middle panel of figure 6.5 with an average at 1696 K. Once again this demonstrates the difference in desorption profile is not structural but has to do with the heating rate. Because the heating rate is substantially slower, there is significantly more time before the temperature is increased. In other words, each process, in this instance desorption, is more likely to occur before the temperature is increased. The laboratory conditions are essentially so fast the chemical processing is catching up.

6.2 Astrophysical Implications

Now that we have shown the heating rates are essential when applying our knowledge to astrophysically-relevant environments, we must also discuss the potential differences in structure. The ices presented here were created through direct deposition of the desired species. Direct deposition may be of some use when considering re-accretion in protoplanetary disk, but in interstellar clouds H_2O is mostly created through the hydrogenation of atomic oxygen. Because of the exothermicity of the hydrogenation process the ice is likely to be fairly compact. [40] The ices are also likely going to be mixed except in the case when discussing infall through various snowlines. The compactness of a mixed ice should not alter the desorption temperature as CO is already mixed. It is important to note layered CO-H_2O compact and porous ices demonstrate differences in CO desorption profiles from a water-rich environment because it will change the surface area accessible to CO. However, this is not the situation with pre-mixed ices. When CO is significantly less abundant than H_2O, as is the case in interstellar ices, desorption will only be dictated by the potential of CO-H_2O. As shown in the mixed porous ice (6.5) nearly half of the starting CO was trapped above 80 K. When considering a mixed compact ice likely more will be trapped as the few pores that are present will be closed.

6.3 Conclusions

The work presented here explored various ices with the intention of unraveling the kinetics involved in the warming of ices relevant to astrophysical laboratory experiments. A number of ices were simulated including pure H_2O ice and layered/mixed CO-H_2O ices. The ices were heated at linear rates and the thermal processing was observed. First, the kinetic process of diffusion was discussed in chapter 5. This chapter was dedicated entirely to the process of thermal desorption.

The simulations demonstrate a good match with experimentally observed and deter-

mined CO desorption profiles from various ices. This includes the desorption feature below 85 K for mixed ices and the two features for layered ices with compact and porous under layers.

We note that, while the experiments and simulations considered here involve pure H_2O and CO ices, interstellar ices consist of many other species, CO_2 and CH_3OH, as well as other components. Also, direct deposition of water ice is unlikely to be the dominant interstellar ice formation mechanism, and experimental deposition rates are typically larger than those that are expected in the interstellar medium. Hence the use of a detailed kinetic model of laboratory ice deposition where we can extrapolate to interstellar conditions.

We present several specific conclusions from this work below:

- When heating ASW to temperatures of 100 K or above pores accumulate into larger pockets that are closed off to the vacuum interface.
- The surface area of H_2O is slightly less when using CO adsorption as a means of measuring instead of direct measurement.
- Mixed CO and H_2O ices can retain as much as 50% of the initial deposited CO.
- Compact ices trap essentially no CO above 60 K at 0.01%. For the porous counterpart, slightly more is retained at 1%.
- The desorption temperature for protoplanetary disk conditions was around 27 K and slightly higher for the interstellar medium at 29 K. This is considerably lower than the mixed ices in the laboratory that have standard desorption temperatures $\sim$46 K.

7

Summary & Future Work

Contents

7.1 Summary

Ices make up a critical component of the chemistry in various star-forming sources, including pre-stellar cores and protoplanetary disks. During the star-formation process, ices composed of simple molecules build up on the surfaces of interstellar dust grains. In the protoplanetary disk stage, so-called "snowlines" appear, corresponding to the threshold temperatures at which ice molecules can exist in the solid phase. These ices are thought to be the precursors of complex organic molecules (COMs) that may later be delivered to planetary bodies and comets. The formation of molecules on grain surfaces, and the subsequent production of COMs, has been demonstrated in laboratory experiments. However, interstellar physical conditions can never be exactly reproduced, and the timescales are vastly different (minutes in the lab versus many thousands of years in the ISM), making the correspondence of the two regimes highly uncertain. **What effect does this divide in timescales and conditions between laboratory and stellar environments have on the resulting chemistry and the way we interpret observations?**

7.1.1 Star Formation and Ices

Ices formed on dust grains go through a range of physical and chemical processing events between the molecular-cloud stage and the formation of a protoplanetary disk. A diagram of proto-stellar physical and chemical evolution is shown in figure 7.1a.[51] The initial stage shown, precollapse, is followed by the collapsing envelop where the gas and dust are being pulled inward by gravity. During the collapse, the gas and dust will experience heating by the protostar. At temperatures relevant to molecular clouds, atoms and molecules such as H, C, N, and CO can stick to grain surfaces. As the grains experience heating expected during the collapse, the ice components gain enough energy to diffuse on the surface and react. CO (the second most abundant molecule in ices after water)[66] can react with atoms such as hydrogen and form methanol(CH_3OH).[88, 17] An unexpected product of this mechanism is glycolaldehyde, a precursor to ribose.[73] The increasing temperature of the grain will allow ice components to sublimate, releasing newly formed species into the gas phase where they can be observed. The release of each individual molecule is dependent on the chemical composition and structure of the surrounding ice.[22, 21, 2, 32] Figure 7.1a indicates the approximate temperatures at which CO will desorb from ices (CO evaporation) and stick again (CO freezeout.) The temperatures indicated were determined using experiments like those in panel b taken from Fayolle *et al.* 2016.

The envelope will keep collapsing until eventually a star is formed. At this stage, there is a star surrounded by a disk of material known as a protoplanetary disk. Within this disk there is a complicated structure including a region, known as the midplane, where gas and dust are shielded from the harsh radiation of the star. In this region, ices can build up once again, and further surface chemistry can occur. The temperature at which molecules can stick to the grain, which determines the position of the snowline, is essential to understand the structure of the disk and the chemistry occurring. Ices on grains may provide the adhesive for grains to stick together, forming the intermediate stages of comets and planets. Interestingly, water deuteration fractions indicate that ices formed in molecular clouds are delivered with little processing during delivery to disks.[19] If this is the case, we need to understand at what temperature ices, such as CO and H_2O, desorb from the grains, because laboratory experiments indicate ices should be completely removed during the hot core stage (upwards of hundreds of Kelvin) where they would likely be processed.

To understand properly how interstellar ices sublimate and recondense, we must understand the physical surfaces they form on and how the local conditions control these structures. These effects will be crucial to determine snowlines ice behavior in protoplanetary disks, and the gas-phase chemistry that results from ice sublimation in various star-formation environments.

7.1.2 Astrophysically-Relevant Laboratory Ice Experiments

Laboratory experiments are used in part to understand observations, but the question is raised how well do the experiments reflect the processes occurring in astronomical environments. To understand the properties of interstellar ices, experimentalists have studied ices created under similar conditions (low pressure and temperature), using infrared and

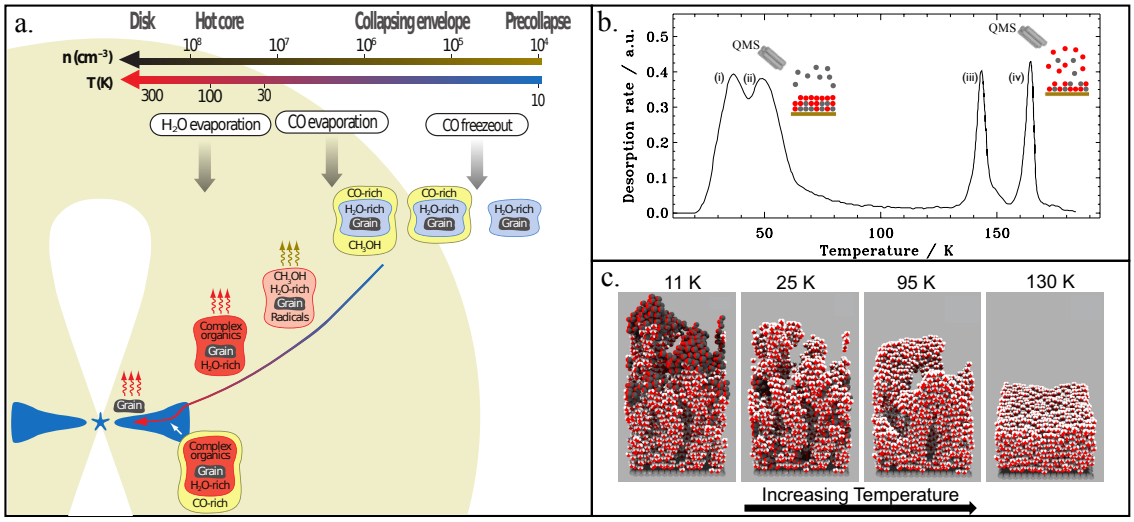

Figure 7.1: Depiction of the star formation process where the arrows indicate the physical evolution during the stellar evolution from prestellar stage and the final stage, the disk. **Panel a** is an adaptation from Herbst & VanDishoeck (2009) describing protostar evolution and its corresponding chemistry.[51] The temperature increases from right to left along with the density. The response of CO to the changing physical parameters is shown in tandem. In **panel b** there is a temperature programmed desorption profile from laboratory experiments.[32] The temperature is shown on the x-axis and CO desorption rate on the y-axis. At regions i and ii, CO is leaving the surface either from a CO-rich environment (i) or a water-rich environment (ii). Stages iii and iv correspond to CO leaving during the rearrangement of water (iii) and sublimates from the surface (iv). **Panel c** shows a model of a layered CO and H_2O ice and how the structure changes with temperature. At 11 K the original layered ice is shown. The next temperature, 25 K, shows CO has diffused into the pores of the H_2O ice where some CO may become trapped until the rearrangement and desorption of H_2O. At 95 K the H_2O has begun collapsing and the last temperature shows the water ice before desorption.

other methods to discern their physical and chemical properties.[7, 12, 57] One method used for the purpose of finding desorption temperatures of an individual species is temperature programmed desorption (TPD). A molecule of interest is typically deposited on either a water ice or bare surface and heated until all such molecules have desorbed. A profile is generated by measuring molecule desorption by a mass spectrometer. In figure 7.1b, CO desorption features are indicated with numbers i - iv and each desorption peak corresponds to CO leaving from a different environment (i.e. different composition or morphology).[32]

The ices in laboratory experiments are often amorphous and have pores. This structure is dependent on many parameters, including formation timescale, temperature, desorption angle, and desorption rates.[7, 12, 83, 57] Since there are many parameters that can alter the structure one must consider the differences in interstellar and laboratory environments. One of the theorized differences between lab and interstellar ices is the delivery of H_2O to the grain. Interstellar H_2O is primarily formed through reactions of hydrogen and oxygen atoms on grains, but, in laboratory experiments, H_2O is typically directly deposited on the surface in TPD experiments to simplify the number of species present. This different formation mechanism means that lab ices are likely to be more porous than interstellar ices. [65, 40]

Ice structure can greatly impact the efficiency of reactions, and the ability for molecules to absorb. For instance, porous amorphous H_2O can adsorb 20 to 50 times more gas than a compact ice.[4] This effect will enhance CO abundances in ices with greater porosity, allowing increased formation of methanol.[52] Thus, grain chemistry should reflect the ice

structure, which will in part change the chemical availability when forming important objects such as planets and comets. **Given the importance of the ice morphology to interstellar and protoplantary chemistry (e.g. snowlines), models are required that can simulate structure in both laboratory and interstellar conditions, extrapolating lab results reliably to interstellar conditions and timescales.**

Scientific Objective

Interstellar physical conditions can never be exactly reproduced, and the timescales are vastly different (minutes in the lab versus many thousands of years in the ISM), making the correspondence of the two regimes highly uncertain. What effect does this divide in timescales and conditions between laboratory and stellar environments have on the resulting chemistry and the way we interpret observations?

To begin to address the divide, we use an off-lattice microscopic kinetic Monte Carlo model to further understand some of the fundamental microscopic processes that govern the formation of molecules and the structure of ices: including the accretion, diffusion, and desorption of the two most abundant molecules in ices: H_2O and CO. First, we modeled the structure of H_2O ices to ensure densities would reflect laboratory results. Then, we studied the interaction of H_2O ice with CO including diffusion, desorption, and trapping. The molecules were selected intentionally because they are the major components of interstellar ices.[8] We then applied the model to some known astronomical conditions to explore interstellar ices. This project has allowed a brief glimpse into the interstellar medium –currently inaccessible in the laboratory –.

We find that the composition of deposited ices is reflected in the desorption temperatures and profiles: layered ices have a two peak structure at temperatures below 80 K whereas mixed ices have a singular desorption peak. Figure 7.3 demonstrates the differences in profiles. The three profiles have a peak around 40 to 60 K which corresponds to the interaction and desorption of CO leaving a primarily water-rich environment.

Ices deposited at 100 K or above, also referred to as compact ices, have high densities ranging from 0.8 to 0.9 g cm^{-3} depending on the exact temperature. These ices have little available surface area except for the topmost layers exposed to the vacuum. This is reflected in the diffusion and desorption characteristics described in this work. The calculated CO surface diffusion barrier was 150 K with very little mixing occurring. The lack of porosity then is reflected in the desorption profile where CO primarily desorbs at 30 K. Very little desorbs at the second desorption peak as is seen at 40 K. The peak height demonstrates no more than a monolayer is desorbing. Further, the CO cannot be trapped as there are little to no pores. We find 0.01% of the original CO is trapped above 60 K.

The porous ice demonstrates there is significantly more interaction between CO and H_2O. The diffusion barrier is higher at 210 K. Mixing is seen in the top half of the ice at temperature below 23 K and penetrates deeper at higher temperatures. Desorption of CO begins at 24 K and continues until the excess layers of CO has desorbed and all that is left is a thin coating on top of water. Around 40 K the CO fully incorporated in H_2O desorbs. By 60 K only 1% of the CO is left because of accessibility of the pores. This finding further demonstrates that the network of pores of pure water ices are accessible to the vacuum interface and provide little means to stop CO from desorbing.

The desorption profile seen in layered ices that occurs at the lowest temperature, which corresponds to CO desorbing from a CO-rich environment, is not present in mixed

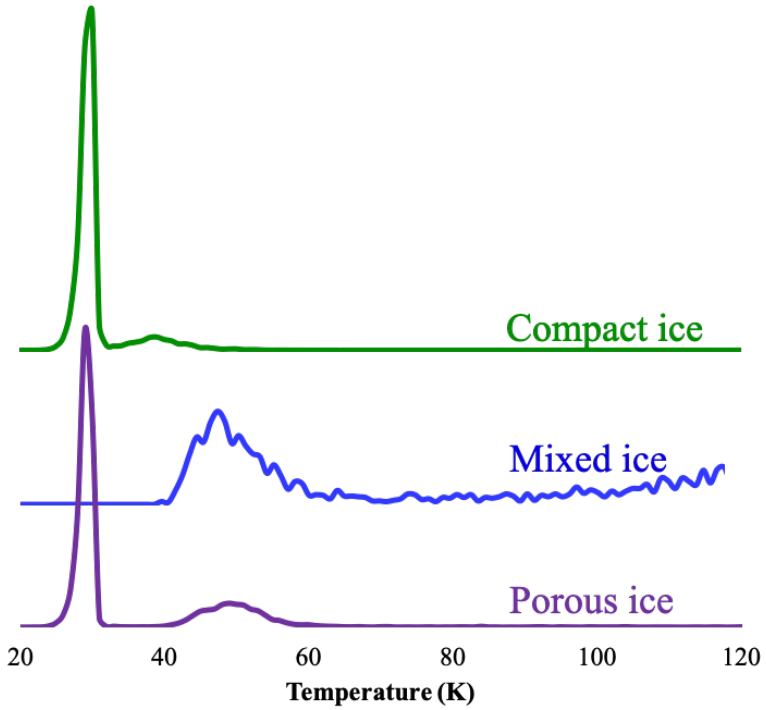

Figure 7.2: Desorption profiles with arbitrary height to show the differences in features between the various deposition parameters.Ices were deposited at a normal angle with deposition temperatures of 10 K (blue and purple) and 100 K (green). The difference between the blue and purple ice is codeposition and layered deposition.

ices. A single desorption peak is observed with a wide profile. Desorption begins at 40 K and trails off around 80 K. The trailing profile indicates a range of binding environments. For instance, in mixed ices the fraction of volatile species will change changing the overall environment. This will affect both the position and the width of the peak. Further, mixed ices allow for more CO trapping than even porous ices. By 85 K 68% of the original CO is retained in the ice.

Ices were deposited directly onto surfaces with rates relevant to protoplanetary disks and pre-stellar cores. At 10 K, the temperature most commonly associated with pre-stellar cores, densities are mostly the same compared to those deposited at laboratory rates and likely. When temperatures are increased the laboratory analog densities begin to diverge and are no longer adequate representatives see table 7.1.

Desorption experiments were tested using direct deposition at 10 K. When considering desorption profiles, we find similar behavior as described with mixed ices hold for pre-stellar cores and protoplanetary disks; the differences in the sources are not the ice structure (because at 10 K most structural differences are minor) but are the heating timescale. We find the heating timescale dramatically changes the desorption temperature of mixed ices where desorption begins as early as 20 K compared to starting around 40 K.

Table 7.1: Ice densities grown with deposition rates representative of dark cloud and protoplanetary disk regions are shown with the corresponding temperature at which ices grown using laboratory conditions have the equivalent density.

Model Temp (K)	Dark Cloud ρ (g cm^{-3})	Temp Equivalent (K)	Protoplanetary Disk ρ (g cm^{-3})	Temp Equivalent (K)
10	0.618	32	0.609	28
20	0.648	43	0.624	34
30	0.676	53	0.647	43
40	0.759	84	0.679	54
50	–	–	0.721	70
60	–	–	0.765	86
70	–	–	0.838	113

7.2 Future Work

Now, when considering astrophysically-relevant environments, the formation of ices is not through direct deposition but through the reactions of atomic species (H, N, O, etc.) and CO, which is often directly deposited from the gas phase. Direct deposition is thought to result in more porosity than when the ice is formed by surface reactions between accreted atoms. With this is mind, ices are likely to be more compact. If they were layered very little CO would interact with the surface of H_2O but when considering mixed ices, the compactness should not prevent CO trapping. In fact, our work shows porosity may hinder the ability to trap CO. Thus, a compact mixed ice may be the most efficient way in trapping CO at higher temperatures.

Many future avenues can be taken with this work. The most important next step would involve testing the reaction network and forming water through the hydrogenation of atomic oxygen. There have been laboratory experiments that do just that but with molecular oxygen. Atomic oxygen is harder to deposit onto the surface because it involves dissociation of molecular oxygen which is not an entirely efficient process. Laboratory abundances would be one means to test and parameterize the reaction network. A schematic below shows some reactions that would be important to parameterize. Oba et al. 2009 discuss such an experiment where they deposit hydrogen and molecular oxygen to form water. [65] The model would also need to be updated to include chemical diffusion as this would further compact the ice.

Criteria to match laboratory experiments:

- At an O2 /H ratio of 0.009, with temperature of 10 K, the ratio between H_2O and H_2O_2 was approximately 0.6, while it becomes approximately 1.3 at 20 K. At 30 and 40 K, the H_2O/H_2O_2 ratio is significantly smaller than that at 10 and 20 K, both at approximately 0.15.

- only 2 percent of H atoms are used for the hydrogenation of O2

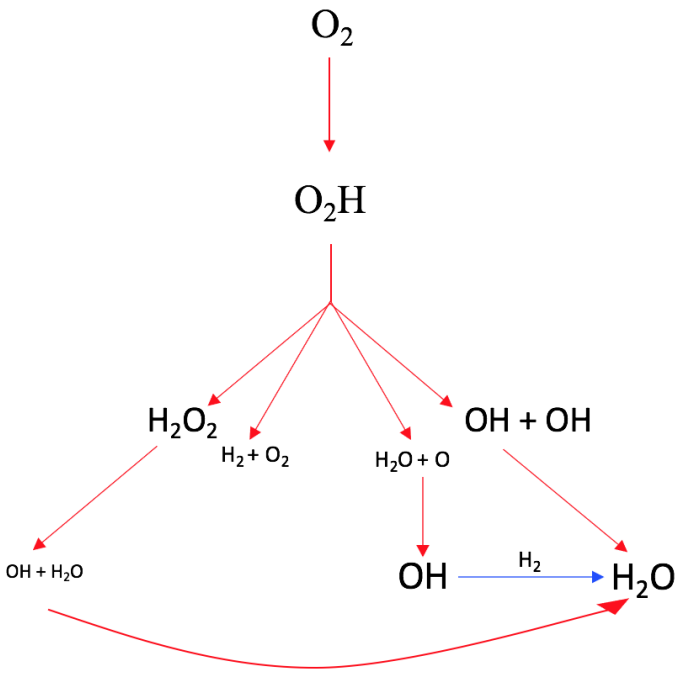

Figure 7.3: Simple schematic showing the hydrogenation of molecular oxygen. The addition of atomic hydrogen is shown in red. Molecular hydrogen reactions are shown in blue.

ID	Reaction	Barrier (K)	Branching
1	$H + H \rightarrow H_2$	0	1
2	$H + OH \rightarrow H_2O$	0	1
3	$H + O_2 \rightarrow O_2H$	0	1
4	$H + O_2H \rightarrow H_2O_2$	0	0.53
5	$H + O_2H \rightarrow OH + OH$	0	0.4
6	$H + O_2H \rightarrow H_2O + O$	0	0.05
7	$H + O_2H \rightarrow H_2 + O_2$	0	0.02
8	$H + H_2O_2 \rightarrow OH + H_2O$	3200	1
9	$H_2 + O \rightarrow OH + H$	3000	1
10	$H_2 + OH \rightarrow H_2O + H$	2100	1
11	$H_2 + O_2H \rightarrow H_2O_2 + H$	2600	1
11	$H_2 + O_2H \rightarrow H_2O_2 + H$	2600	1
12	$OH + OH \rightarrow H_2O_2$	0	0.87
13	$OH + OH \rightarrow H_2O + O$	0	0.13

Bibliography

[1] M. Agúndez, J. Cernicharo, and M. Guélin. Discovery of interstellar ketenyl (HCCO), a surprisingly abundant radical. *A&A*, 577:L5, May 2015.

[2] R. Alan May, R. Scott Smith, and B. D. Kay. The release of trapped gases from amorphous solid water films. II. "Bottom-up" induced desorption pathways. *J. Chem. Phys.*, 138:104502–104502, Mar. 2013.

[3] T. Albertsson and D. Semenov. CHEMODYNAMICAL DEUTERIUM FRACTIONATION IN THE EARLY SOLAR NEBULA : THE ORIGIN OF WATER ON EARTH AND IN ASTEROIDS AND COMETS. *The Astrophysical Journal*, 784(39):11, 2014.

[4] P. Ayotte, R. S. Smith, K. P. Stevenson, Z. Dohnálek, G. A. Kimmel, and B. D. Kay. Effect of porosity on the adsorption, desorption, trapping, and release of volatile gases by amorphous solid water. *Journal of Geophysical Research*, 106(E12):33,387–33,392, 2001.

[5] E. A. Bergin, Y. Aikawa, G. A. Blake, E. F. van Dischoeck, V. B. Reipurth, D. Jewitt, and K. Keil. The Chemical Evolution of Protoplanetary Disks. *Annual Review of Astronomy and Astrophysics*, 45:339–396, 2007.

[6] J. B. Bergner, K. I. Oberg, R. Mahesh, and E. C. Fayolle. Kinetics and mechanisms of the acid-base reaction bet. *The Astrophyical Journal*, 829(85):13pp, October 2016.

[7] B. S. Berland, D. E. Brown, M. A. Tolbert, and S. M. George. Refractive index and density of vapor-deposited ice. *Geophysical Research Letters*, 22(24):3493–3496, 1995.

[8] A. C. A. Boogert, P. A. Gerakines, and D. C. B. Whittet. Observations of the icy universe. *ARA&A*, 53:541–581, Aug. 2015.

[9] J.-B. Bossa, K. Isokoski, M. S. de Valois, and H. Linnartz. Thermal collapse of porous interstellar ice. *Astronomy & Astrophysics*, 545:A82 1–6, 2012.

[10] J. B. Bossa, K. Isokoski, M. S. de Valois, and H. Linnartz. Thermal collapse of porous interstellar ice. *A&A*, 545:A82, Sept. 2012.

[11] J. B. Bossa, K. Isokoski, D. M. Paardekooper, M. Bonnin, E. P. van der Linden, T. Triemstra, S. Cazaux, A. G. G. M. Tielens, and H. Linnartz. Porosity measurements of interstellar ice mixtures using optical laser interference and extended effective medium approximations. *A&A*, 561:A136, Jan. 2014.

[12] D. E. Brown, S. M. George, C. Huang, E. K. L. Wong, K. B. Rider, R. S. Smith, and B. D. Kay. H2O condensation coefficient and refractive index for vapor-deposited ice from molecular beam and optical interference measurements. *Journal of Physical Chemistry*, 100:4988–4995, 1996.

[13] C. Bu, C. A. Dukes, and R. A. Baragiola. Spontaneous cracking of amorphous solid water films and the dependence on microporous structure. *Applied Physics Letters*, 109:201902, Nov. 2016.

[14] C. Bu, J. Shi, U. Raut, E. H. Mitchell, and R. A. Baragiola. Effect of microstructure on spontaneous polarization in amorphous solid water films. *J. Chem. Phys.*, 142:134702, Apr. 2015.

[15] V. Buch and J. P. Devlin. Spectra of dangling OH bonds in amorphous ice: Assignment to 2- and 3-coordinated surface molecules. *J. Chem. Phys.*, 94:4091–4092, Mar. 1991.

[16] S. Cazaux, J.-B. Bossa, H. Linnartz, and A. G. G. M. Tielens. Pore evolution in interstellar ice analogues. *Astronomy & Astrophysics*, 573(A16):1–7, 2015.

[17] K.-J. Chuang, G. Fedoseev, S. Ioppolo, E. F. van Dishoeck, and H. Linnartz. H-atom addition and abstraction reactions in mixed CO, H2CO and CH3OH ices - an extended view on complex organic molecule formation. *Monthly Notices of the Royal Astronomical Society*, 455(2):1702–1712, 2015.

[18] F. J. Ciesla, S. Krijt, R. Yokochi, and S. Sandford. The efficiency of noble gas trapping in astrophysical environments. *The Astrophysical Journal*, 867(146), November 2018.

[19] L. I. Cleeves, E. A. Bergin, C. M. O. Alexander, F. Du, D. Graninger, K. I. Öberg, and T. J. Harries. The ancient heritage of water ice in the solar system. *Science*, 345(6204):1590–1593, 2014.

[20] A. R. Clements, B. Berk, I. R. Cooke, and R. T. Garrod. Kinetic monte carlo simulations of water ice porosity: extrapolations of deposition parameters from the laboratory to interstellar space. *Physical Chemistry Chemical Physics*, 20:5553–5568, 2018.

[21] M. P. Collings, M. A. Anderson, R. Chen, J. W. Dever, S. Viti, D. A. Williams, and M. R. S. McCoustra. A laboratory survey of the thermal desorption of astrophysically relevant molecules. *Monthly Notices of the Royal Astronomical Society*, 354(4):1133–1140, 2004.

[22] M. P. Collings, J. W. Dever, H. J. Fraser, M. R. S. McCoustra, and D. A. Williams. Carbon Monoxide Entrapment in Interstellar Ice Analogs. *The Astrophysical Journal*, 583(2):1058–1062, 2003.

[23] M. P. Collings, J. W. Dever, and M. R. S. McCoustra. Sub-monolayer coverages of CO on water ice. *Chemical Physics Letters*, 415:40–45, Oct. 2005.

[24] I. R. Cooke, K. I. Oberg, E. C. Fayolle, Z. Peeler, and J. B. Bergner. Co diffusion and desorption kinetics in co2 ices. *The Astrophyical Journal*, 852(75):12pp, January 2018.

[25] H. M. Cuppen and E. Herbst. Simulation of the Formation and Morphology of Ice Mantles on Interstellar Grains. *The Astrophysical Journal*, 668(2005):294–309, 2007.

[26] H. M. Cuppen, L. J. Karssemeijer, and T. Lamberts. The kinetic Monte Carlo method as a way to solve the master equation for interstellar grain chemistry. *Chemical Reviews*, 113, 2013.

[27] V. Devlin, J. P. andBuch. . *J. Chem. Phys.*, 99:16534, 1995.

[28] L. d'Hendecourt and E. Dartois. Interstellar matrices: the chemical composition and evolution of interstellar ices as observed by iso. *Spectrochimica Acta Part A: Molecular and Biomolecular Spectroscopy*, 57(4):669 – 684, 2001.

[29] Z. Dohnálek, G. A. Kimmel, P. Ayotte, R. S. Smith, and B. D. Kay. The deposition angle-dependent density of amorphous solid water films. *J. Chem. Phys.*, 118:364–372, Jan. 2003.

[30] Z. Dohnálek, G. A. Kimmel, P. Ayotte, R. S. Smith, B. D. Kay, G. A. Kimmel, P. Ayotte, R. S. Smith, B. D. Kay, and Z. Dohna. The deposition angle-dependent density of amorphous solid water films The deposition angle-dependent density of amorphous solid water films. *The Journal of Chemical Physics*, 118:364–372, 2003.

[31] M. Eldrup, A. Vehanen, P. J. Schultz, and K. G. Lynn. Positronium formation and diffusion in crystalline and amorphous ice using a variable-energy positron beam. *Physical Review B*, 32:7048–7064, Dec. 1985.

[32] E. C. Fayolle, J. Balfe, R. Loomis, J. Bergner, D. Graninger, M. Rajappan, and K. I. Oberg. N 2 AND CO DESORPTION ENERGIES FROM WATER ICE. *The Astrophysical Journal Letters*, 816(L28):L28, 2016.

[33] Fayolle, E. C., Öberg, K. I., Cuppen, H. M., Visser, R., and Linnartz, H. Laboratory h2o:co2 ice desorption data: entrapment dependencies and its parameterization with an extended three-phase model. *A&A*, 529:A74, 2011.

[34] G. Fedoseev, K. J. Chuang, S. Ioppolo, D. Qasim, E. F. van Dishoeck, and H. Linnartz. Formation of Glycerol through Hydrogenation of CO Ice under Prestellar Core Conditions. *ApJ*, 842(1):52, June 2017.

[35] H. J. Fraser, M. P. Collings, J. W. Dever, and M. R. S. McCoustra. Using laboratory studies of CO-H_2O ices to understand the non- detection of a 2152cm^{-1} (4.647μm) band in the spectra of interstellar ices. *MNRAS*, 353:59–68, Sept. 2004.

[36] H. J. Fraser, M. P. Collings, M. R. S. Mccoustra, and D. A. Williams. Thermal desorption of water ice in the interstellar medium. *Monthly Notices of the Royal Astronomical Society*, 327, 2001.

[37] A. Fredon, T. Lamberts, and H. M. Cuppen. Energy Dissipation and Nonthermal Diffusion on Interstellar Ice Grains. *The Astrophysical Journal*, 849(2):125, nov 2017.

[38] A. Fresneau, G. Danger, A. Rimola, P. Theule, F. Duvernay, and T. Chiavassa. Trapping in water – an important prerequisite for complex reactivity in astrophysical ices : the case of acetone (CH 3) 2 C = O and ammonia NH 3 1 I N T RO D U C T I O N. *Monthly Notices of the Royal Astronomical Society*, 443:2991–3000, 2014.

[39] K. Furuya, M. N. Drozdovskaya, R. Visser, E. F. Van Dishoeck, C. Walsh, D. Harsono, U. Hincelin, and V. Taquet. Water delivery from cores to disks: Deuteration as a probe of the prestellar inheritance of h2o. *Astronomy & Astrophysics*, 599(A40):18, 2017.

[40] R. T. Garrod. Three-dimensional, off-lattice monte carlo kinetics simulations of interstellar grain chemistry and ice structure. *The Atrophysical Journal*, 778(158):14, December 2013.

[41] E. L. Gibb, D. C. B. Whittet, A. C. A. Boogert, and A. G. G. M. Tielens. Interstellar ice: The infrared space observatory legacy. *The Astrophysical Journal Supplement Series*, 151:35–73, 2004.

[42] B. Gundlach and J. Blum. The Stickiness of Micrometer-sized Water-ice Particles. *ApJ*, 798(1):34, Jan. 2015.

[43] T. Hama and N. Watanabe. Surface Processes on Interstellar Amorphous Solid Water : Adsorption, Diffusion, Tunneling Reactions, and Nuclear-Spin Conversion. *Chemical Reviews*, 113(12):8783–8839, 2013.

[44] G. B. Hansen and T. B. McCord. Amorphous and crystalline ice on the galilean satellites: A balance between thermal and radiolytic processes. *Journal of Geophysical Research: Planets*, 109(E1), 2004.

[45] T. I. Hasegawa, E. Herbst, and C. Ming Leung. MODELS OF GAS-GRAIN CHEMISTRY IN DENSE INTERSTELLAR CLOUDS WITH COMPLEX ORGANIC MOLECULES. *The Astrophysical Journal Supplement Series*, 82:167–195, 1992.

[46] J. He, A. R. Clements, S. Emtiaz, F. Toriello, R. T. Garrod, and G. Vidali. The Effective Surface Area of Amorphous Solid Water Measured by the Infrared Absorption of Carbon Monoxide. *The Astrophysical Journal*, 878(2):94, jun 2019.

[47] J. He, S. Emtiaz, A. Boogert, and G. Vidali. The $^{12}CO_2$ and $^{13}CO_2$ Absorption Bands as Tracers of the Thermal History of Interstellar Icy Grain Mantles. *ApJ*, 869:41, Dec. 2018.

[48] J. He, S. Emtiaz, and G. Vidali. Measurements of Diffusion of Volatiles in Amorphous Solid Water: Application to Interstellar Medium Environments. *ApJ*, 863:156, Aug. 2018.

[49] J. He, S. Emtiaz, and G. Vidali. Measurements of diffusion of volatiles in amorphous solid water: Application to interstellar medium environments. *The Astrophysical Journal*, 863(156):7pp, August 2018.

[50] J. He and G. Vidali. Characterization of thin film CO_2 ice through the infrared $\nu_1 + \nu_3$ combination mode. *MNRAS*, 473:860–866, Jan. 2018.

[51] E. Herbst and E. F. van Dishoeck. Complex Organic Interstellar Molecules. *Annual Review of Astronomy and Astrophysics*, 47:427–480, Sept. 2009.

[52] H. Hidaka, N. Miyauchi, A. Kouchi, and N. Watanabe. Structural effects of ice grain surfaces on the hydrogenation of CO at low temperatures. *Chemical Physics Letters*, 456(1-3):36–40, 2008.

[53] N. Horimoto, H. S. Kato, and M. Kawai. Stepwise morphological change of porous amorphous ice films observed through adsorption of methane. *J. Chem. Phys.*, 116:4375–4378, Mar. 2002.

[54] K. Isokoski, J. B. Bossa, T. Triemstra, and H. Linnartz. Porosity and thermal collapse measurements of H2O, CH3OH, CO2, and H2O:CO2 ices. *Physical Chemistry Chemical Physics (Incorporating Faraday Transactions)*, 16:3456, Jan. 2014.

[55] J. Keane, A. Boogert, A. Tielens, P. Ehrenfreund, and W. Schutte. Bands of solid CO2 in the 2–3 μm spectrum of S 140:IRS1. *Astronomy & Astrophysics*, 375:L43–L46, 2001.

[56] G. A. Kimmel, Z. Dohnálek, K. P. Stevenson, R. S. Smith, B. D. Kay, K. P. Stevenson, R. S. Smith, B. D. Kay, G. A. Kimmel, and Z. Dohna. Control of amorphous solid water morphology using molecular beams . II . Ballistic deposition simulations Control of amorphous solid water morphology using molecular beams . II . Ballistic deposition simulations. *Journal of Chemical Physics*, 114(12):5295–5303, 2001.

[57] G. A. Kimmel, K. P. Stevenson, Z. Dohnálek, R. S. Smith, B. D. Kay, R. S. Smith, and B. D. Kay. Control of amorphous solid water morphology using molecular beams . I . Experimental results Control of amorphous solid water morphology using molecular beams . I . Experimental results. *Journal of Chemical Physics*, 114(12):5284–5294, 2001.

[58] J. Klinger, D. Benest, A. Dollfus, and R. Smoluchowski. *Amorphous and Porous Ices in Cometary Nuclei*. Springer Netherlands, 1985.

[59] H. Kobayashi, H. Hidaka, T. Lamberts, T. Hama, H. Kawakita, J. Kästner, and N. Watanabe. Hydrogenation and Deuteration of C 2 H 2 and C 2 H 4 on Cold Grains : A Clue to the Formation Mechanism of C 2 H 6 with Astronomical Interest. *The Astrophysical Journal*, 837(155):15, 2017.

[60] A. Kouchi, K. Furuya, T. Hama, T. Chigai, T. Kozasa, and N. Watanabe. Direct measurements of activation energies for surface diffusion of co and co2 on amorphous solid water using in situ transmission electron microscopy. *The Astrophysical Journal Letters*, 891(22):7pp, March 2020.

[61] T. Lamberts, H. M. Cuppen, S. Ioppolow, and H. Linnartz. Water formation at low temperatures by surface O 2 hydrogenation III: Monte Carlo simulation. *Phys. Chem. Chem. Phys. Phys. Chem. Chem. Phys*, 15:8287–8302, 2013.

[62] T. Lamberts, X. D. Vries, and H. M. Cuppen. The formation of ice mantles on interstellar grains revisited – the e ff ect of exothermicity. *Faraday Discussions*, 168:327–347, 2014.

[63] T. Lauck, L. Karssemeijer, K. Shulenberger, M. Rajappan, K. Öberg, and H. Cuppen. Co diffusion into amorphous h2o ices. *The Astrophysical Journal*, 801(118):12pp, March 2015.

[64] C. Mitterdorfer, M. Bauer, T. G. A. Youngs, D. T. Bowron, C. R. Hill, H. J. Fraser, J. L. Finney, and T. Loerting. Small-angle neutron scattering study of micropore collapse in amorphous solid water. *Physical Chemistry Chemical Physics (Incorporating Faraday Transactions)*, 16:16013, July 2014.

[65] Y. Oba, N. Miyauchi, H. Hidaka, T. Chigai, N. Watanabe, and A. Kouchi. FORMATION OF COMPACT AMORPHOUS H 2 O ICE BY CODEPOSITION OF HYDROGEN ATOMS WITH. *The Astrophysical Journal*, 701(5):464–470, 2009.

[66] K. I. Öberg, A. C. Adwin Boogert, K. M. Pontoppidan, S. Van Den Broek, E. F. Van Dishoeck, S. Bottinelli, G. A. Blake, and N. J. Evans Ii. The Spitzer Ice Legacy: Ice Evolution from Cores to Protostars. *The Astrophysical Journal*, 740(109):1–16, 2011.

[67] K. I. Öberg, E. C. Fayolle, H. M. Cuppen, E. F. V. Dishoeck, and H. Linnartz. Quantification of segregation dynamics in ice mixtures. *Astronomy & Astrophysics*, 194:183–194, 2009.

[68] K. I. Öberg, V. V. Guzmán, K. Furuya, C. Qi, Y. Aikawa, S. M. Andrews, R. Loomis, and D. J. Wilner. The comet-like composition of a protoplanetary disk as revealed by complex cyanides. *Nature*, 520:198–201, Apr. 2015.

[69] M. E. Palumbo. Formation of compact solid water after ion irradiation at 15 K. *A&A*, 453:903–909, July 2006.

[70] E. M. Penteado, C. Walsh, and H. M. Cuppen. Sensitivity analysis of grain surface chemistry to binding energies of ice species. *The Astrophyical Journal*, 844(1):13, 2017.

[71] J. Pipes, J. Roux, and A. Smith. Infrared transmittance of contaminated cryocooled optical windows. *American institute of Aeronautics and Astronautics*, 16(984), 1978.

[72] F. Poulet and J. Cuzzi. The composition of saturn's rings. *Icarus*, 160(2):350 – 358, 2002.

[73] M. W. Powner, B. Gerland, and J. D. Sutherland. Synthesis of activated pyrimidine ribonucleotides in prebiotically plausible conditions. *Nature*, 459(7244):239–242, 2009.

[74] C. Qi, K. I. Oberg, C. C. Espaillat, C. E. Robinson, S. M. Andrews, D. J. Wilner, G. A. Blake, E. A. Bergin, and L. I. Cleeves. Probing co and n2 snow surfaces in protoplanetary disks with n2h+ emission. *The Astrophysical Journal*, 882(160), September 2019.

[75] U. Raut, M. Famá, B. D. Teolis, and R. A. Baragiola. Characterization of porosity in vapor-deposited amorphous solid water from methane adsorption. *The Journal of Chemical Physics*, 127(204713):1–6, 2007.

[76] U. Raut, M. Famá, B. D. Teolis, and R. A. Baragiola. Characterization of porosity in vapor-deposited amorphous solid water from methane adsorption. *J. Chem. Phys.*, 127:204713–204713, Nov. 2007.

[77] U. Raut, B. D. Teolis, M. J. Loeffler, R. A. Vidal, M. Famá, and R. A. Baragiola. Compaction of microporous amorphous solid water by ion irradiation. *J. Chem. Phys.*, 126:244511–244511, June 2007.

[78] B. Saxton. Astronomers get rare peek at early stage of star formation. *National Radio Astronomy Observatory*, March 2012.

[79] B. Schmitt, J. M. Greenberg, and R. J. A. Grim. The Temperature Dependence of the CO Infrared Band Strength in CO: H 2O Ices. *ApJ*, 340:L33, May 1989.

[80] K. R. Schwarz, E. A. Bergin, L. I. Cleeves, K. Zhang, K. I. Oberg, G. A. Blake, and D. E. Anderson. Unlocking co depletion in protoplanetary disks. ii. primordial c/h predictions inside the co snowline. *The Astrophysical Journal*, 877(131), June 2019.

[81] R. S. Smith, C. Huang, E. K. L. Wong, and B. D. Kay. The molecular volcano: Abrupt ccl_4 desorption driven by the crystallization of amorphous solid water. *Phys. Rev. Lett.*, 79:909–912, Aug 1997.

[82] T. Stantcheva and E. Herbst. Models of gas-grain chemistry in interstellar cloud cores with a stochastic approach to surface chemistry. *Astronomy & Astrophysics*, 423:241–251, 2004.

[83] K. P. Stevenson, G. A. Kimmel, Z. Dohnalek, R. S. Smith, and B. D. Kay. Controlling the Morphology of Amorphous Solid Water. *Science*, 283:1505, Mar. 1999.

[84] A. G. G. M. Tielens and W. Hagen. Model calculations of the molecular composition of interstellar grain mantles. *Astronomy & Astrophysics*, 114:245–260, 1982.

[85] H. C. van de Hulst. The solid particles in interstellar space. *Recherches Astronomiques de l'Observatoire d'Utrecht*, 11:2.i–2, Jan. 1946.

[86] A. I. Vasyunin and E. Herbst. Reactive Desorption and Radiative Association as Possible Drivers of Complex Molecule Formation in the Cold Interstellar Medium. *ApJ*, 769:34, May 2013.

[87] S. Viti, M. P. Collings, J. W. Dever, M. R. S. McCoustra, and D. A. Williams. Evaporation of ices near massive stars: models based on laboratory temperature programmed desorption data evaporation of ices near massive stars: models based on laboratory temperature programmed desorption data. *Monthly Notices of the Royal Astronomical Society*, 354:1141–1145, August 2004.

[88] N. Watanabe and A. Kouchi. Efficient Formation of Formaldehyde and Methanol By the Addition of Hydrogen Atoms To Co in H 2 O-Co Ice At 10 K. *The Astrophysical Journal*, 571:L173–L176, 2002.

[89] N. Watanabe, A. Nagaoka, T. Shiraki, and A. Kouchi. HYDROGENATION OF CO ON PURE SOLID CO AND CO-H 2 O MIXED ICE. *The Astrophysical Journal*, 616, 2004.

[90] M. S. Westley, G. a. Baratta, and R. a. Baragiola. Density and index of refraction of water ice films vapor deposited at low temperatures. *Journal of Chemical Physics*, 108(8):3321–3326, 1998.

[91] A. Whalen. Cometary dust particiles. *https://stardust.jpl.nasa.gov/science/sd-particle.html*, November 2003.

[92] D. C. B. Whittet, W. A. Schutte, A. G. G. M. Tielens, A. C. A. Boogert, T. de Graauw, P. Ehrenfreund, P. A. Gerakines, F. P. Helmich, T. Prusti, and E. F. van Dishoeck. An ISO SWS view of interstellar ices: first results. *Astronomy & Astrophysics*, 315:L357–L360, 1996.

[93] Y. G. Yang, X. W. Zhou, R. A. Johnson, and H. N. G. Wadley. Monte carlo simulation of hyperthermal physical vapor deposition. *Acta Mater*, 49:3321–3332, 2001.

[94] W. Zheng, D. Jewitt, and R. I. Kaiser. Electron irradiation of crystalline and amorphous D $_2$O ice. *Chemical Physics Letters*, 435:289–294, Feb. 2007.

[95] X. W. Zhou, R. A. Johnson, and H. N. G. Wadley. A molecular dynamics study of nickel vapor deposition: Temperature, incident angle, and adatom energy effects. *Acta Mater*, 45(4):1513–1524, 1997.